

EFFECT OF NEUTRON IRRADIATION AND THERMAL AGING ON CAST  
AUSTENITIC STAINLESS STEEL AND STAINLESS STEEL WELD PHASE STABILITY

By

ZHANGBO LI

A DISSERTATION PRESENTED TO THE GRADUATE SCHOOL  
OF THE UNIVERSITY OF FLORIDA IN PARTIAL FULFILLMENT  
OF THE REQUIREMENTS FOR THE DEGREE OF  
DOCTOR OF PHILOSOPHY

UNIVERSITY OF FLORIDA

2017

© 2017 Zhangbo Li

To my family and friends

## ACKNOWLEDGMENTS

I would like to give my most sincere thanks to my advisor and my committee chair Dr. Yong Yang, Associate Professor of Nuclear Engineering Program, Department of Materials Science and Engineering, University of Florida for his support and guidance on my research. The consistent establishment of this work benefits greatly from his outstanding vision and extraordinary insight towards the materials aging and degradation program.

I am deeply thankful for my supervisory committee Prof. Michele Manuel, Prof. Gerhard Fuchs, Prof. Pat Patterson and Prof. Youping Chen for their valuable guidance and encouragement to the success of this research. It is such a great honor to have them in my committee.

My colleagues and friends have provided tremendous amount of help, support and encouragement during the last few years. They are my colleagues, friends and collaborators, Dr. Wei-Yang Lo, Dr. Yuedong Wu, Nicholas Silva, Haode Yang, Kookhyun Jeong, Chi Xu, Nils Strombom, Dr. Soumitra Sulekar, Dr. Yaqiao Wu and Dr. Yiren Chen. Thank you all for your help, support and dedication.

Finally, I would like to give my special thanks to my family for their love, company and trust on me for this journey.

## TABLE OF CONTENTS

	<u>page</u>
ACKNOWLEDGMENTS.....	4
LIST OF TABLES.....	8
LIST OF FIGURES.....	9
LIST OF ABBREVIATIONS.....	12
ABSTRACT.....	14
CHAPTER	
1 BACKGROUND AND INTRODUCTION.....	16
1.1 Basics of CASSs/Welds.....	16
1.1.1 Ferrite and Austenite Structures and Properties.....	16
1.1.2 Alloy Elements in Stainless Steel Alloys.....	18
1.1.3 Metallurgy in CASS and Weld.....	22
1.1.4 Structure/Property Relationships in CASS/Welds.....	24
1.2 Application of CASS/Weld in LWRs.....	26
1.3 Aging Degradation Study of CASS/Weld in LWRs.....	28
1.3.1 Aging Embrittlement Study Methodology.....	28
1.3.2 Microstructure Evolution of Thermally Aged Ferrite.....	30
1.3.3 Activation Energy Extraction of Aging Embrittlement.....	36
1.4 Motivation.....	37
1.4.1 Nuclear Energy and LWRs Sustainability Program.....	37
1.4.2 Challenges of Neutron Irradiation Enhanced Aging Degradation.....	38
1.4.3 Comparison of Thermal Aging and Neutron Irradiation Validation.....	41
1.4.4 Synergistic Effect of Irradiation and Thermal Aging on Ferrite Decomposition.....	42
1.4.5 Micro Scratch Test for Fracture Toughness Extraction.....	43
2 EXPERIMENTAL DETAILS.....	45
2.1 Materials and Treatment.....	45
2.2 OM & SEM Metallography.....	47
2.3 TEM Crystallography and Characterization.....	48
2.4 Atom Probe Microstructural Characterization & Analysis.....	49
2.4.1 Frequency Distribution.....	51
2.4.2 Radial Distribution Function.....	52
2.4.3 Proxigram of Cr Map.....	54
2.4.4 Cluster Analysis.....	55
2.5 Mechanical Property Testing.....	58
2.5.1 Nano-indentation Test.....	58

2.5.2 Miniature Tensile Test .....	62
2.5.3 Micro Scratch Test.....	63
3 RESULTS .....	68
3.1 Metallography and Chemical Composition.....	68
3.1.1 CF-3 .....	68
3.1.2 308L weld .....	70
3.2 Crystallography and Microstructure Characterization .....	73
3.2.1 Spinodal Decomposition.....	73
3.2.2 G Phase Precipitate.....	79
3.3 Mechanical Testing Results .....	84
3.3.1 Nano-indentation Results on Welds .....	84
3.3.2 Tensile Test on CF-3.....	86
3.3.3 Micro Scratch Test on Welds.....	88
4 DISCUSSION .....	90
4.1 Macrostructure and Metallurgical Analysis.....	90
4.1.1 CF-3 .....	90
4.1.2 308L Weld .....	93
4.2 Microstructure Evolution in Ferrite-Spinodal Decomposition.....	94
4.2.1 Synergistic Effect of Spinodal Decomposition .....	94
4.2.2 Irradiation Enhancement Estimation.....	95
4.2.3 Spinodal Decomposition at High Dose Irradiation .....	97
4.2.4 Spinodal Decomposition under TEM .....	103
4.3 Microstructure Evolution in Ferrite-G Phase .....	105
4.3.1 G Phase Formation under Irradiation and Aging in CF-3/308L weld .....	105
4.3.2 G Phase Coarsening under High Dose Irradiation in CF-3.....	108
4.3.3 TEM investigation and APT validation .....	110
4.4 Effect of Thermal Aging and Neutron Irradiation Validation .....	113
4.5 Mechanical Testing Analysis.....	115
4.5.1 Nano-indentation .....	115
4.5.2 Tensile Test.....	116
4.5.3 Micro Scratch Test.....	119
4.6 Structure-Property Relationship Validation on CASS/weld .....	120
4.6.1 Spinodal Decomposition Strengthening.....	120
4.6.2 Particle Strengthening by G Phase .....	123
4.6.3 Other Strengthening Mechanism.....	124
4.6.4 Compact Tension Test and Impact Test of CF-3.....	128
5 CONCLUSIONS .....	130
APPENDIX	
A ATOM PROBE BASICS AND TIP FABRICATION.....	133
B MICRO SCRATCH FRACTURE TOUGHNESS .....	136

C THE PHYSICS OF NEUTRON IRRADIATION DAMAGE.....	139
D SUPPLEMENT RESULTS.....	142
LIST OF REFERENCES.....	144
BIOGRAPHICAL SKETCH.....	153

## LIST OF TABLES

<u>Table</u>		<u>page</u>
1-1	Comparison between ferrite and austenite. ....	17
1-2	Properties of austenitic and ferritic stainless steels. ....	18
1-3	Operating pressure and temperature in primary pressure boundary of PWR. ....	28
1-4	Component serviced in PWRs with CASSs and weld. ....	41
2-1	Chemical composition of the cast stainless steel CF3. ....	45
2-2	Chemical composition of 308L weld fusion zone. ....	47
3-1	APT measured chemical composition of the ferrite at difference. conditions. ....	70
3-2	Average composition of G phase precipitate in CF-3. ....	80
3-3	Summary of G phase precipitation. ....	82
3-4	Fracture toughness of 308L weld measured from micro scratch test. ....	88
A-1	LEAP Tip Annular Milling Steps. ....	135

## LIST OF FIGURES

<u>Figure</u>	<u>page</u>
1-1 Pure iron cooling curve.....	16
1-2 Cr-Fe binary system .....	19
1-3 Impact of alloy element on the $\gamma$ loop.....	20
1-4 Phase diagram of Fe-Ni binary. ....	21
1-5 Phase diagram calculated using JMatPro for DSS. ....	22
1-6 Influence of composite volume fraction on mechanical properties.....	25
1-7 Application of CASS/weld in PWR.....	27
1-8 Comparison of spinodal decomposition and nucleation & growth.....	32
1-9 Ostwald step theory of precipitation behavior.....	34
1-10 Flux of element during G phase formation and spinodal decomposition of ferrite. ....	35
1-11 Full size Charpy V-notch impact energy of CF-3. ....	39
1-12 Application of CASS/weld in reactor core internals.....	40
2-1 SEM images of a typical TEM sample on the grid fabricated using FIB. ....	49
2-2 Cr frequency distribution of ferrite in DSS with varied aging time.....	52
2-3 Cr map in ferrite phase in DSS with varied aging times.....	52
2-4 Typical RDF plot of Cr-Cr of ferrite in aged CF-3.....	53
2-5 Typical proxigram of Cr of spinodally decomposed ferrite. ....	54
2-6 Mn-Mn nearest neighbor distributions for orders from 1 to 10 .....	56
2-7 Gaussian peak deconvolution for the 4th order nearest neighbor distribution and determination of $d_{max}$ and $d_e$ .....	57
2-8 Cluster analysis parameters selection of the $N_{min}$ in MSM.....	57
2-9 Cluster analysis results of ferrite in 308L weld aged for 2,226 h at 400 °C.....	58
2-10 Optical image of the sample surface of electropolished 308L weld at 500X.....	59

2-11	Loading and unloading curve for the nano-indentation.....	60
2-12	Tip scanned image of 308L weld with indentations. ....	61
2-13	Sample dimension for the sub-size tensile test of CF-3.....	62
2-14	Schematic of the micro scratch test.....	63
2-15	Indenter shape function calibration with fitted curve. ....	65
3-1	Metallographic image of CF-3.....	68
3-2	Metallographic image of unaged CF-3 using SEM. ....	69
3-3	Metallographic image of 308L weld .....	71
3-4	Metallographic image of 308L weld using SEM.....	72
3-5	Cr distribution in ferrites upon different treatment conditions of CF-3.....	74
3-6	Fe-Cr elemental frequency distributions in ferrites for different conditions. ....	74
3-7	Frequency distribution of Fe and Cr in ferrite of irradiated CF-3.....	76
3-8	Wavelength vs irradiation dose of neutron irradiated CF-3.....	77
3-9	TEM images of spinodal decomposition with mottled structure in ferrite of 308L weld. The small figure in the lower left corner is the APT reconstruction image.....	78
3-10	G-phase precipitates in aged, irradiated, and aged-irradiated ferrites. The images are sized to have an identical scale, and the isovalue thresholds of Mn, Ni and Si are 2, 10 and 6 %, respectively. ....	80
3-11	Cluster size distribution of neutron irradiated CF-3.....	81
3-12	The ionic concentration of Ni, Si and Mn in G phase precipitate in ferrite of irradiated CF-3.....	81
3-13	Diffraction pattern of ferrite matrix and G phase precipitate of CF-3 irradiated at 20 dpa. ....	83
3-14	TEM image of G phase precipitate in ferrite of CF-3 irradiated at 20 dpa.....	84
3-15	Nano-hardness of the austenite and ferrite + austenite phase of 308L weld aged at 0 h and 2226 h.....	85
3-16	Stress strain curves of CF-3 with 24% ferrite tested at room temperature. ....	86

3-17	SEM fractography of CF-3 with 24% ferrite .....	87
3-18	SEM images of the scratch of 308L weld, images on the right are the red box area in images on the left. ....	89
4-1	70 wt.% Fe-Cr-Ni pseudo binary phase diagram.....	91
4-2	Variation in solidification mode in weld. ....	94
4-3	Schematics of spinodal decomposition.....	98
4-4	Cr proxigrams in ferrite of irradiated CF-3. ....	100
4-5	Iso-surfaces of Mn-Ni-Si clusters and interfaces of Cr enriched $\alpha'$ phases .....	107
4-6	G phase precipitate in ferrite of CF-3 irradiated at 20 dpa reconstructed in IVAS. ....	111
4-7	Relative position of the G phase cluster from Ni iso-surface and the cylinder. .	113
4-8	G phase precipitate in ferrite of CF-3 irradiated at 20 dpa reconstructed in IVAS. ....	113
4-9	Decoupled stress strain curve of ferrite, austenite and CF-3 in exaggerated illustration. ....	118
4-10	Strength and hardness of unaged Fe-Cr alloys. ....	125
A-1	LEAP Tip fabrication steps in FIB-SEM procedure. ....	135
B-1	Relationship of fracture toughness and sample thickness.....	136
C-1	Schematic of neutron irradiation damage in solid. ....	140
D-1	Maximum size, mean size and volumetric number density of G-phase precipitates of CF-3. ....	142
D-2	As-weld 308L OM image of the base metal and fusion zone.....	142

## LIST OF ABBREVIATIONS

ANL	Argonne National Lab
APT	Atom probe tomography
ASTM	American standard testing method
AWS	American welding society
BWR	Boiling water reactor
CAES	Center for Advanced Energy Studies
CASS	Cast austenitic stainless steel
CT	Compact tension
DSS	Duplex stainless steel
EBSD	Electron back-scattering diffraction
EDS	Energy-dispersive X-ray spectroscopy
FIB	Focused ion beam
IVAS	Integrated visualization analysis software
LEAP	Local field atom probe
INL	Idaho National Lab
LWR	Light water reactor
MaCS	Microscopy and Characterization Suite
MSM	Maximum separation method
ORNL	Oak Ridge National Lab
PKA	Primary knock-on atom
PWR	Pressurized water reactor
RDF	Radial distribution function

SEM	Scanning electron microscopy
TEM	Transmission electron microscopy
UTS	Ultimately tensile strength
YS	Yield strength
UE	Uniform elongation

Abstract of Dissertation Presented to the Graduate School  
of the University of Florida in Partial Fulfillment of the  
Requirements for the Degree of Doctor of Philosophy

EFFECT OF NEUTRON IRRADIATION AND THERMAL AGING ON CAST  
AUSTENITIC STAINLESS STEEL AND STAINLESS STEEL WELD PHASE STABILITY

By

Zhangbo Li

December 2017

Chair: Yong Yang

Major: Materials Science and Engineering

Cast austenitic stainless steels (CASSs) and welds used in light water reactors (LWRs) usually adopt a duplex structure consisting of austenite and ferrite. Their compounds are widely used in LWRs as primary pressure boundary and reactor vessel internal components. The common cast stainless steels in service include CF-3 and CF-8 series with ferrite content up to 30%. For the welds, ferrite contents are limited to less than 20%. Potential embrittlement can occur due to microstructure evolution during LWR environmental degradation. Fully understanding of such phase decomposition-related embrittlement is crucial to the accurate evaluation and assessment of the LWR sustainability program. Therefore, systematic experiments and analysis have been performed in this study to investigate the effect of aging and irradiation on the phase stability of ferrite in CASS/weld.

The stability of ferrite in CF-3 under long-term aging and irradiation was examined. Low dose neutron irradiation can enhance the decomposition of ferrite synergistically with thermal aging owing to irradiation-enhanced diffusion. At high

irradiation doses, the ferrite phase exhibited a steady evolution of phase transformation with respect of spinodal decomposition and G phase precipitation coarsening.

For 308L weld, both long-term aging and low dose neutron irradiation induced spinodal decomposition, with large Cr concentration fluctuation wavelength and amplitude and minor G phase precipitate. Such decomposition could be the major reason for the ferrite phase nano-hardness increase, while little change in the hardness of austenite was observed. The periodic strain field combined with the Cr rich zone lattice friction augmentation would both oppose movement of dislocation and strengthen the ferrite phase.

CHAPTER 1  
BACKGROUND AND INTRODUCTION

1.1 Basics of CASSs/Welds

1.1.1 Ferrite and Austenite Structures and Properties

Shown in Figure 1-1, the pure iron cooling curve illustrates the transformation sequence of iron from liquid to  $\delta$  ferrite  $\rightarrow$   $\gamma$  austenite  $\rightarrow$   $\alpha$  ferrite at different temperature ranges.  $\delta$  and  $\alpha$  ferrite both have a body centered cubic (B.C.C.) structure with lattice constant of 2.85 – 2.88 Å. In comparison, the  $\gamma$  austenite phase has a face centered cubic (F.C.C.) crystal structure with lattice constant of 3.598 Å [1].

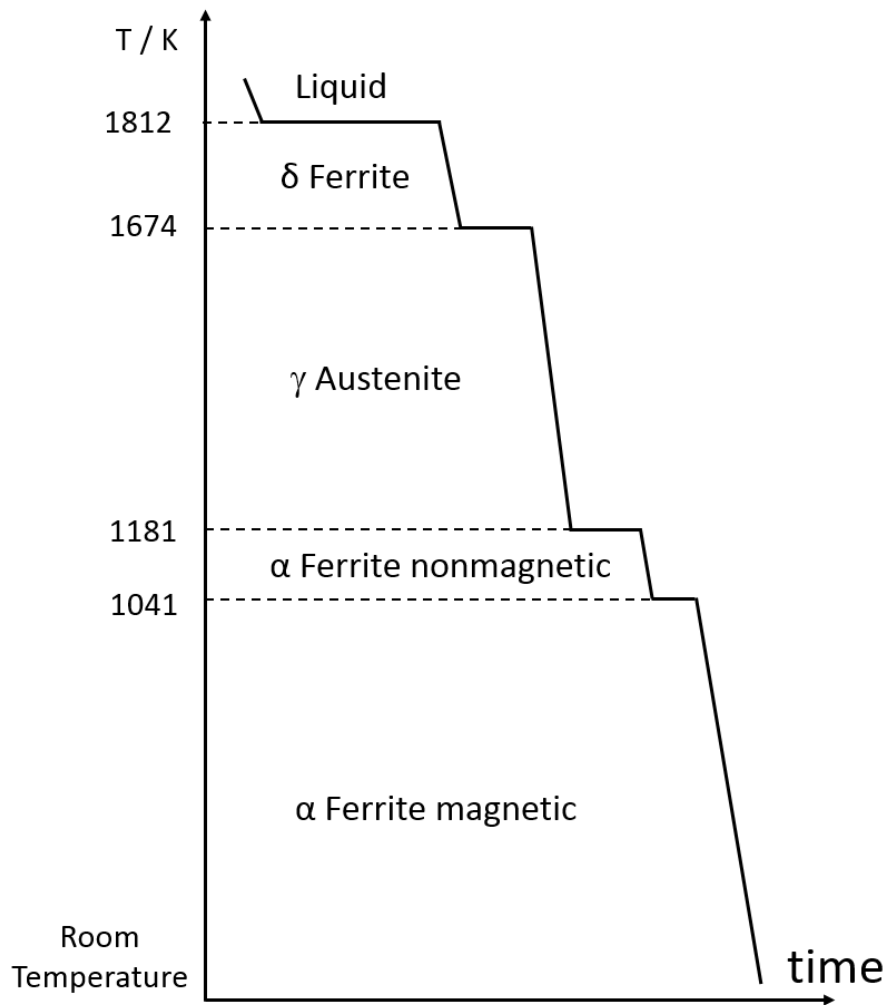


Figure 1-1. Pure iron cooling curve. (Source: Ref. [2])

For the F.C.C. structure, the close-packed plane has the smallest lattice spacing. Thus, less activation energy is required for slip to occur compared with other planes. In crystallography, there are four sets of independent close-packed planes in the F.C.C. structure which are {111} type planes. Each plane contains three <110> slip directions. There are 12 slip systems for F.C.C. crystals in total. All of them are identical with the same activation energy for dislocation slip. In comparison, B.C.C. crystals do not have close-packed planes, and slip can occur along the plane with the smallest Burgers vector. Plane types identified are six {110} types, twelve {112} types and twelve {123} types. There are two <111> directions for each {110} plane and one for the {112} and {123} planes. In total, there are 48 slip systems in B.C.C. crystals. Table 1-1 shows the details of ferrite and austenite slip plane configurations based on their crystallography [3].

Table 1-1. Comparison between ferrite and austenite. (Source: Ref. [1])

Phase	Crystal structure	Lattice parameter (Å)	Slip plane, direction & systems	Burger's vector (Å)
Ferrite	B.C.C.	2.865	{110},{112},{123} <111> (48)	2.48
Austenite	F.C.C.	3.598	{111} <110> (12)	2.54

Usually, for a duplex stainless steel (DSS), the ferrite phase is less ductile and harder compared with austenite phase at room temperature [4]. Ferrite can become brittle at extremely low temperature and exhibits a characteristic ductile-to-brittle transition phenomenon. In contrast, temperature drop has limited impact on the ductility of austenite. An implicit explanation is that the dislocation movement in ferrite requires greater activation energy. Above the ductile-brittle transition temperature, the kinetic energy of thermal vibration is sufficient to facilitate the dislocation movement. This helps enable the ductile behavior of ferrite. Below the ductile-brittle transition temperature,

dislocation becomes less mobile due to decreased thermal vibrations of the atoms. Greater external stress is required to enable dislocation movement. If the required stress is greater than that for the crack formation, deformation happens via cracking instead of dislocation movement. Ferrite becomes brittle under such conditions. The brittle cleavage usually occurs along the [001] plane, as it is not the close-packed plane.

In general, ferrite phase has greater strength, hardness and stress corrosion cracking resistance, while austenite phase has excellent performance in toughness, ductility, weldability and castability.

Table 1-2. Properties of austenitic and ferritic stainless steels.

Properties	Austenitic	Ferritic
Toughness	Very high	Moderate
Ductility	Very high	Moderate
Weldability	Good	Limited
Thermal expansion	High	Moderate
Stress corrosion cracking resistance	Low	Very high
Magnetic properties	Non-magnetic	Ferromagnetic

### 1.1.2 Alloy Elements in Stainless Steel Alloys

The alloy elements play a very important role in the austenite/ferrite formation in stainless steel alloys. Elements that tend to promote austenite formation are termed as austenite formers or stabilizers. On the contrary, elements that favor the stable ferrite phase are commonly referred to as ferrite formers. Austenite stabilizers include carbon, nickel, manganese and nitrogen. Manganese and nitrogen are usually added to replace some nickel as an austenite stabilizer. Without austenite stabilizer, the retention of  $\gamma$  is almost impossible at room temperature. Figure 1-2 shows the phase diagram of Fe-Cr where a  $\gamma$  loop can be seen. The  $\gamma$  loop indicates that the composition and temperature range for stable austenite is quite limited for Fe-Cr binary alloys. The addition of an

austenite former, such as nickel, can expand the  $\gamma$  loop. This could help with the control of austenite content. Ferrite stabilizers include chromium, silicon and molybdenum. The addition of these elements will retard the formation of austenite while favoring the ferrite phase. The impact of those alloy elements on the  $\gamma$  loop is shown in Figure 1-3.

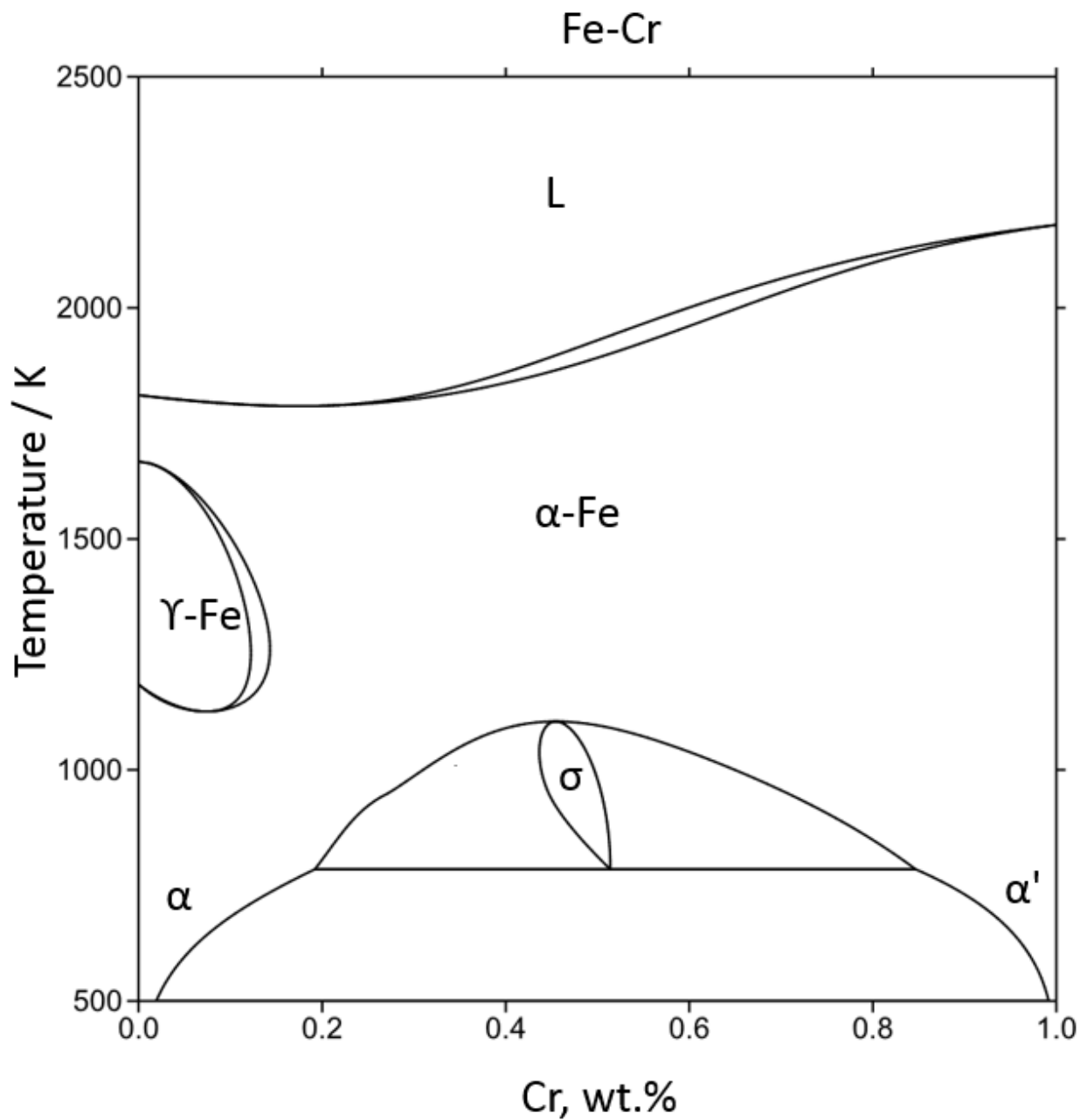


Figure 1-2. Cr-Fe binary system. (Source: Ref. [1,5])

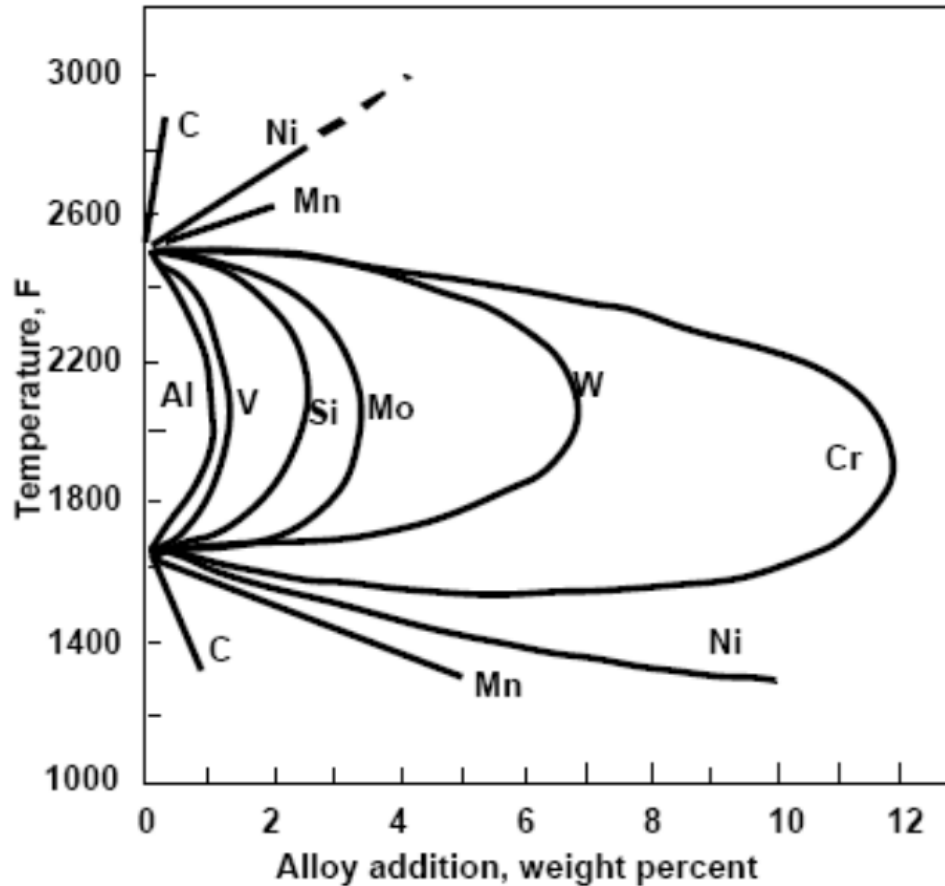


Figure 1-3. Impact of alloy element on the  $\gamma$  loop. (Source: Ref. [6])

Carbon has been known to be the most common interstitial element for steel alloys. Its atomic size is only about 1/30 of an iron atom. Carbon helps increase the tensile strength and hardness due to solid solution strengthening. Carbon is a very strong austenite former. Its concentration is typically kept less than 0.05% to prohibit the formation of carbide at grain boundaries in austenitic stainless steels.

Chromium is the essential element in stainless steel to enable the stainless property. When containing greater than 10.5% chromium, an oxide thin film will form on the surface of steel when exposed to air as passivation. This thin oxide layer prevents further oxidation of stainless steel. Chromium is a strong ferrite stabilizer. The atomic radii of chromium and iron are very close, with iron atoms at 0.126 nm and chromium

atoms at 0.127 nm [7]. As chromium exists in the B.C.C. structure at room temperature, it greatly favors ferrite formation by substitution for iron atoms.

Nickel is a strong and expensive austenite former widely used in various kinds of stainless steels. Ni tends to partition to the austenite phase during the alloy solidification process owing to its low solubility in ferrite. Pure Ni exhibits an F.C.C. crystal structure shown in the binary Ni-Fe phase diagram in Figure 1-4. When alloyed with Fe, Ni can perfectly dissolve in F.C.C. austenite owing to the negligible lattice misfit. When Ni content is less than 20 at.% in Fe, no intermetallic phases with ordered structure can be formed, as indicated in the phase diagram. Nickel can also help improve the fracture toughness, high temperature yield strength, formability and weldability.

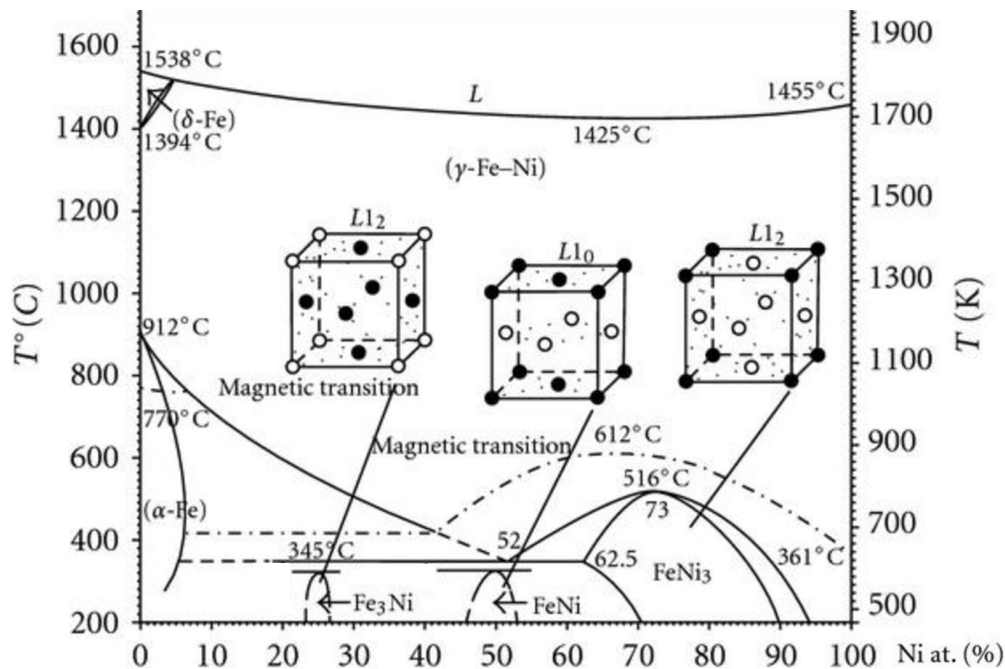


Figure 1-4. Phase diagram of Fe-Ni binary. (Source: Ref. [8])

Molybdenum primarily increases the pitting corrosion resistance of stainless steels and high temperature strength in austenitic and DSSs [9]. Molybdenum-containing grades of stainless steels are generally more corrosion resistant than

molybdenum-free grades. In austenitic stainless steels, between two to seven percent of molybdenum is usually added, whereas in DSSs, between three to five percent is added. The addition of one or two percent molybdenum to ferritic stainless steels also significantly increases the corrosion resistance and the elevated temperature strength through solid solution hardening. Application of this effect in industrial alloys can be found in heat exchangers and other elevated temperature equipment, such as automotive exhaust systems.

### 1.1.3 Metallurgy in CASS and Weld

CASS and weld typically have a structure of ferrite phase surrounded by the retained austenite because of the incomplete phase transformation from ferrite to austenite during the subsequent rapid cooling. This is very common in the DSS cooling process as well. A phase diagram by Li [10] calculated using JMatPro of slow cooling of DSS is shown in Figure 1-5. In this case, the cooling rate plays a major role in controlling the final volume fraction of ferrite phase.

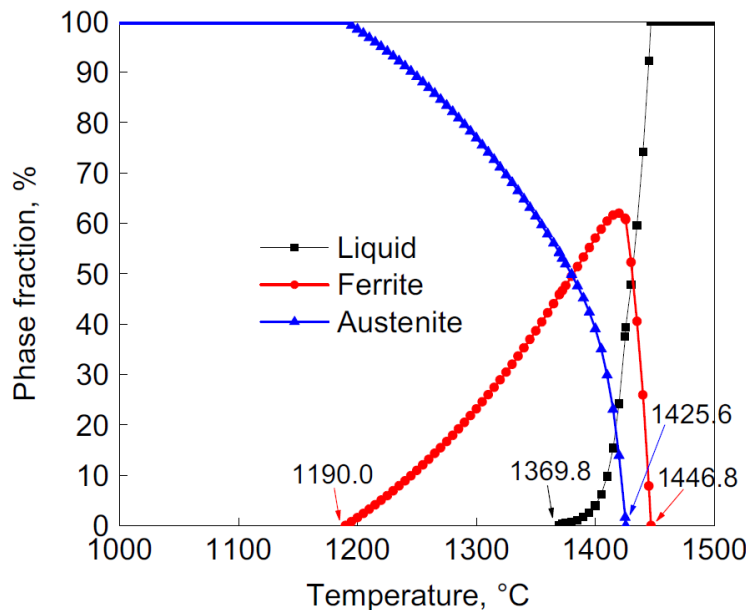


Figure 1-5. Phase diagram calculated using JMatPro for DSS. (Source: Ref.[11])

Because of incomplete ferrite-to-austenite transformations illustrated above, CASS can contain ferrite with volume fractions up to 30%. The fusion zones of the stainless steel welds normally have a smaller ferrite content. They both share a duplex structure of branch-like ferrite surrounded by austenite. Such a composite structure allows for excellent performance of CASS/welds in power plants, oil and gas industries where oxidation resistance and good strength are required.

The determination of ferrite formation in CASSs and welds has been well studied in the past decades [12]. As the microstructure determines the mechanical properties in applications, many experiments and theories have been developed to understand the ferrite formation process. Several American Standard Testing Method (ASTM)/ American Welding Society (AWS) standards for CASSs/welds have been established. In addition, considerable research has been carried out concerning the ferrite content determination. For CASS, ASTM A800 covers grades CF-3, CF-3A, CF-8 and CF-8A. In addition, AWS A4.2 covers most of the welds. Normally, the ferrite number is used to indicate the ferrite volume fraction in those stainless steels. The quantity of ferrite contained in the stainless steel is fundamentally a function of the chemical composition and its thermal treatment history. Primarily three different methods can be used for CASSs introduced, as described below.

The first method is the chemical composition determination method. The total ferrite-promoting elements and total austenite-promoting elements are calculated as chromium equivalents and nickel equivalents, respectively, using empirical equations. The values are then used to compare with the Shaeffler diagram via corresponding

chromium and nickel equivalents. The precision of the ferrite content estimated from the chemical composition depends on the accuracy of the chemical analysis procedure.

The second method is the magnetic induction method which has been widely applied. A probe is used to measure the magnetic content of a specimen that interacts with its built-in magnetic field. Such interaction can induce a change in voltage inside the coil which can be measured to estimate the overall content of ferrite. This method is the most accurate method for casting alloys [13].

The third method is metallographic examination. An etching technique is needed to reveal the ferrite phase. Ferrite content can be estimated from the ratio of ferrite area over the total area based on the recorded micrographs, as explained in test method E562.

The method for the determination of ferrite content in austenitic stainless steel weld in AWS A4.2 is very similar to the magnetic response method described in ASTM A800. Because of its facile procedure and good accuracy, the magnetic response method was used for the determination of ferrite content of CASSs/welds in this study.

#### **1.1.4 Structure/Property Relationships in CASS/Welds**

CF series steels can contain delta ferrite phase with volume fraction up to 30%. The percentage of ferrite can be measured by the magnetic method. Such a duplex structure of secondary phase surrounded by the matrix is quite similar to the structure of fiber reinforced composite materials. Based on the composite theory by Campbell [10], the ferrite content and structural configuration can impart excellent mechanical property enhancement to the bulk. Content greater than 30% of ferrite could easily allow for the connected and continuous structure shown in Figure 1-6. This could enable a much greater impact on strength and modulus compared with random short configuration in

structure. Thus, for typical applications of CASS, the ferrite content is best maintained at around 15% - 25% to allow for a sufficient amount of toughness. In comparison, welds usually have much less ferrite content.

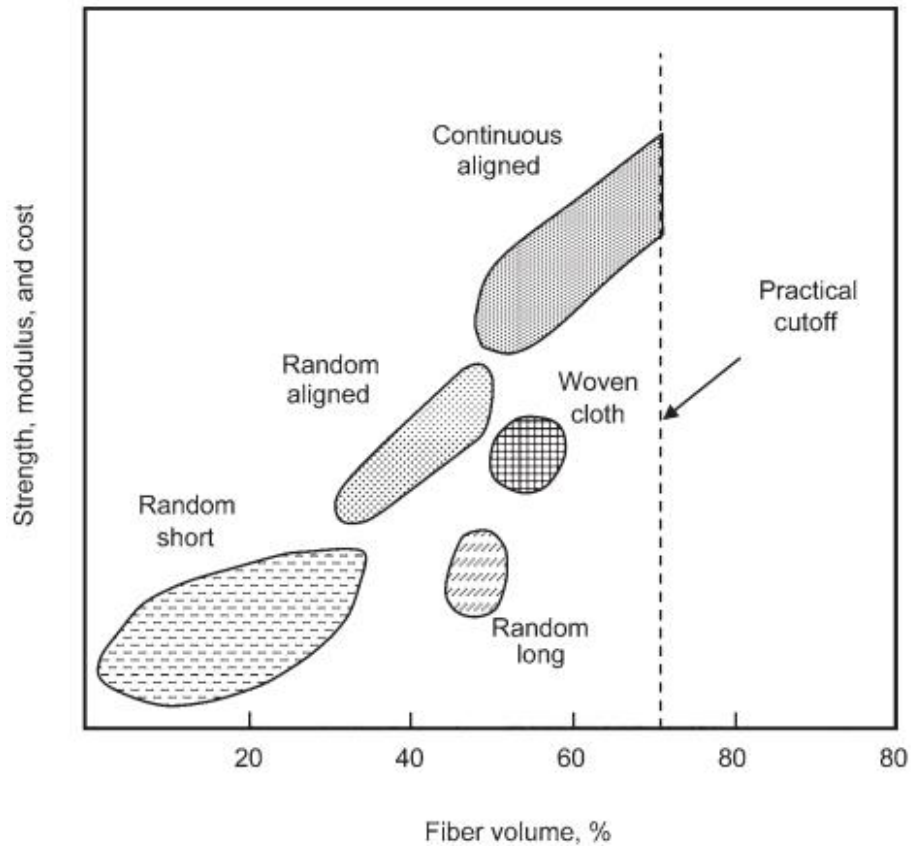


Figure 1-6. Influence of composite volume fraction on mechanical properties. (Source: Ref. [10])

Another widely analyzed structure/property relationship in CASS/welds is the impact of ferrite morphology. It has been reported by Kamiya and Karlsson [14,15] that ferrite in continuous film-like form can cause a certain amount of fracture toughness weakening of the weld. In comparison, the globular or discontinuous vermicular ferrite shows little fracture toughness shift. As further explained by Chopra [16], a globular ferrite morphology will have a higher fracture toughness. In comparison, a lacy network of ferrite with content greater than 30% could act as a continuous fracture path for crack

propagation. At very low temperature, ferrite turns brittle, while the austenite stays ductile. The continuous thin film morphology allows cracks to form and propagate along the failed ferrite network. Meanwhile, in the discontinuous ferrite morphology configuration, crack propagation could be slowed or stopped by the austenite matrix. However, Bonnet [13] proposed that the ferrite skeleton could remain continuous even with content less than 5%. He selectively dissolved the austenite phase by an electrochemical method. While the metallographic image indicated that the ferrite phase was fully isolated, the ferrite skeleton structure was continuous. The ferrite morphology in CASS, such as CF-3 and CF-8, usually exhibits a partially connected short range acicular morphology [17,18]. Such a morphology can maintain excellent strength enhancement without harming the ductile and tough austenite matrix.

In general, the ferrite/austenite duplex structure in CASS/weld provides excellent combination of toughness, weldability and castability with high strength.

## **1.2 Application of CASS/Weld in LWRs**

The CF-3 and CF-8 alloys have been used in LWRs in primary pressure boundaries and core internal components [19]. A general description of the types of steels used in pressurized water reactors (PWRs) is illustrated in Figure 1-7. For the primary pressure boundary, CF-8A and CF-8M have been primarily used for reactor coolant pipes, pump casings, reactor coolant valve bodies and covers. CF-3 later replaced CF-8 in the construction of those components. Type 308/308L weld metals are often used for welding the austenitic steel parts, e.g. circumferential and vertical welds in boiling water reactor (BWR) core shrouds, in vessel welds for the core control drives, and in jet pump assembly welds. These welding alloys are also used in the overlay cladding of the reactor pressure vessels. To prevent hot cracking, stainless steel welds

normally contain a small amount of  $\delta$ -ferrite up to 10% in the austenite matrix. Table 1-4 listed the operation temperature and pressure for the primary and secondary loop. Generally, those components operate in the temperature range of 275 °C -315 °C under high pressure at 2250 psi and in corrosive environments.

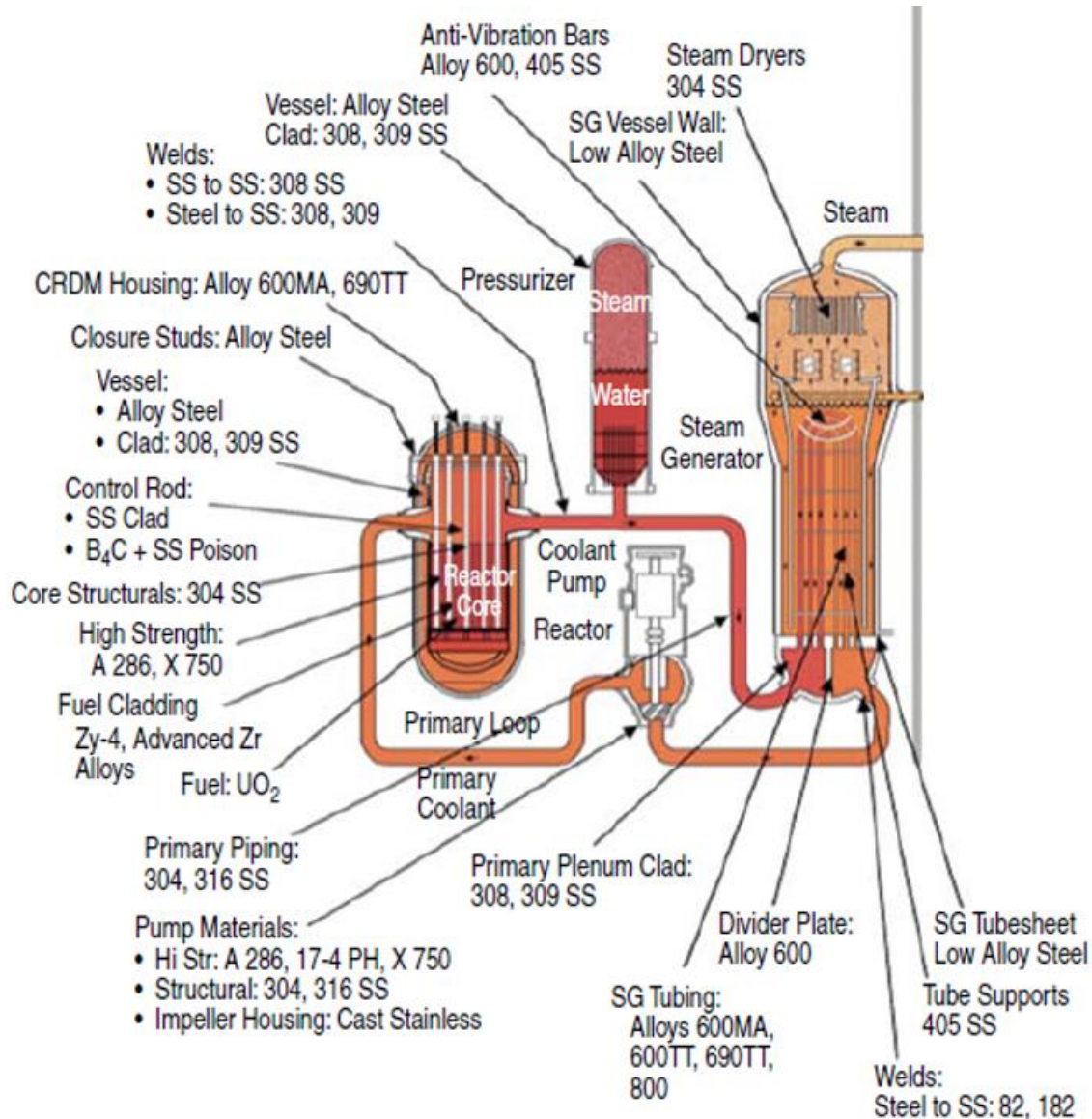


Figure 1-7. Application of CASS/weld in PWR. (Source: Ref. [20,21])

The ferrite phase can help improve the strength, corrosion resistance and weldability of the casting/welds. However, the duplex structure stainless steel

cast/welds are prone to thermal aging embrittlement. With a designed service lifetime of 40 years, aging can induce various phase decompositions in ferrite. This can dramatically affect its mechanical properties. Based on the experimental data,  $\sigma$  phase,  $\chi$  phase, carbide and Cr-rich phase all will contribute to the embrittlement of the casting under various conditions. With the stabilizer of Mo and less Ni, the  $\sigma$  phase formation temperature was pushed up to 950 °C, but to avoid  $\sigma$  phase formation, casting must be cooled past 850 °C in less than 2 minutes.  $\chi$  phase was typically formed above 550 °C and has rarely been detected when aged below 500 °C. Thus, Cr rich phase plays the major role in cast embrittlement.

Table 1-3. Operating pressure and temperature in primary pressure boundary of PWR.  
(Source: Ref. [22])

Loop	Pressure	T (hot leg)	T (cold leg)
Primary	15.5 MPa (2250 psi)	315 °C (l)	275 °C (l)
Secondary	6.2 MPa (900 psi)	220 °C (l)	275 °C (g)

### 1.3 Aging Degradation Study of CASS/Weld in LWRs

#### 1.3.1 Aging Embrittlement Study Methodology

The earliest research interest on CASS can date back to the aging degradation of CASS/weld program initiated in 1985 at Argonne National Lab (ANL). Its goal was to characterize and correlate the microstructure of in-service reactor components and laboratory-aged material embrittlement and to identify the mechanism of embrittlement. The basic methodology is summarized in the following paragraphs.

To evaluate the aging related embrittlement kinetics, the aging process was assumed to be thermally activated. The activation energy can be estimated by examining the onset of embrittlement (Charpy V-notch impact toughness measured at room temperature) through aging experiments at varied time and temperature. Based

on the initial data tested by George Fisher of Switzerland on CF casting in the temperature range of 300 °C-400 °C, an activation of 100.4 kJ/mol was extracted. The prediction of the long-term aging embrittlement of steel casting can be achieved through the Arrhenius extrapolation shown in Eq. 1-1, in which  $E_a$  is the activation energy and  $R$  is the gas constant. For a service component at aging temperature  $T$  and time frame  $t$ , the equivalent aging parameter  $P$  can be calculated with respect to the degree of embrittlement at 400 °C.

$$t = 10^P \exp \left[ \frac{E_a}{R} \left( \frac{1}{T} - \frac{1}{673} \right) \right] \quad (1-1)$$

The application essence of those materials in LWRs was the focus of a field engineering study. Depending on the source of the material obtained, the heat treatment history can be quite different. For samples obtained from a decommissioned power plant, it is difficult to trace their original metallography and heat treatment history. Because of this, some researchers have performed aging on CASS samples without consideration of the heat treatment [24]. In other cases, castings in small dimensions were solution annealed at 1040 °C- 1060 °C [25]. Recently, Li [11] carried out solution treatment at 1080 °C for varied time lengths on DSSs. Combined with subsequent TEM and tensile testing on the later-aged samples, the study showed that the solution annealing has little effect on ferrite compositions with insignificant impact on the thermal aging kinetics.

It is trustworthy that the grain size and the grain orientation effect of the casting were not considered as key parameters in the aging degradation studies described above. The austenite dendrite grain in CASSs can reach a few milli-meters. Within each

austenite grain, hundreds of  $\mu\text{m}$ -scale ferrite grains reside at the dendrite core of austenite. Ferrite acts as a reinforcement inside the ductile austenite matrix. This duplex structure plays a critical role in maintaining the high strength and excellent ductility of CASS. Such a composite-like structure has been confirmed by Schwarm [26,27] via finite element modeling (FEM). Schwarm investigated CF-3 and CF-8 in non-aged and aged condition via tensile testing and nano-indentation. Further electron backscattering diffraction and FEM were also performed to simulate the process of mechanical testing. Ferrite tends to be more stress sensitive while austenite is more strain sensitive. Compared with austenite grain boundaries, the ferrite/austenite hetero-phase boundaries play a significant role in plastic deformation. Furthermore, Wang [28] investigated the plastic deformation of ferrite/austenite duplex structure steels using tensile testing. Scanning electron microscopy (SEM) was used to record the specimen surface deformation pattern after a certain strain was reached. The result indicated that the ferrite/austenite phase boundary plays a major role in strengthening the material after long periods of thermal exposure. Thus, to facilitate the study and simplify the discussion, only the ferrite/austenite duplex structure was considered as the key factor in the present study.

### **1.3.2 Microstructure Evolution of Thermally Aged Ferrite**

It has been known for over 60 years that ferrite-containing stainless steels are susceptible to aging embrittlement when serviced in the reactor operational temperature range [17]. Identified phase transformations in ferrite include spinodal decomposition and Ni-Si rich G phase in the temperature range of 280 °C - 400 °C.

The Fe and Cr binary system has been well studied from a metallurgical perspective. Similar to other binary systems, such as Cu-Ti, Ai-Ag and Ni-Au, they all

exhibit a miscibility gap in a certain temperature range. The phase separation evolution inside the miscibility gap can sometimes go without nucleation and growth, leading to formation of an interconnected morphology known as spinodal decomposition. Spinodal decomposition of ferrite occurs when the ferrite composition falls inside the spinodal region of the phase diagram of Fe and Cr (Figure 1-2). Fe and Cr atoms demix from each other through uphill diffusion shown in Figure 1-8. This process eventually results in a very fine modulating morphology of Cr rich  $\alpha'$  phase and Fe rich  $\alpha$  phase. As the Cr concentration fluctuates, the extent of decomposition can be measured by the wavelength of the Cr concentration profile. The formation of the  $\alpha + \alpha'$  structure can lead to hardening of the ferrite phase. Historically, the characterization and measurement of spinodal decomposition in Fe-Cr binary system has mainly relied on the Mossbauer spectroscopy [29–33]. Nowadays, spectroscopy with atomic resolution tools are normally used for the characterization and quantification.

To explain the spinodal decomposition in the perspective of free energy, the Cahn-Hilliard equation was introduced, as shown in Eq. 1-1 to Eq. 1-3 [34].

$$G = \int [f(c) + \kappa(\nabla c)^2] dV \quad (1-1)$$

$$f(c) = f(c_0) + (c - c_0) \frac{\partial f}{\partial c} + \frac{1}{2} (c - c_0)^2 \frac{\partial^2 f}{\partial c^2} + \dots \quad (1-2)$$

$$\Delta G = \int \left[ \frac{1}{2} (c - c_0)^2 \frac{\partial^2 f}{\partial c^2} + \kappa(\nabla c)^2 \right] dV \quad (1-3)$$

In these equations, G denotes the Gibbs free energy, f(c) indicates the Gibbs free energy as a function of solute concentration c. The term  $\kappa(\nabla c)^2$  is the increase in free energy due to concentration fluctuation. If we assume the binary solution to be incompressible and isotropic with constant molar volume,  $\Delta G$  can become negative if

$\frac{\partial^2 f}{\partial c^2} < 0$  inside the spinodal region. Such a driving force can enable the binary system to demix into two phases with different compositions via uphill diffusion. Depending on the lattice parameters of the two phases, the misfit value  $\delta$  can be calculated. For the Fe-Cr binary system,  $\delta$  is quite small, i.e., far less than 5%. This can help explain why the two phases are highly coherent with little distinction in X-ray diffraction (XRD) and transmission electron microscopy (TEM) diffraction patterns.

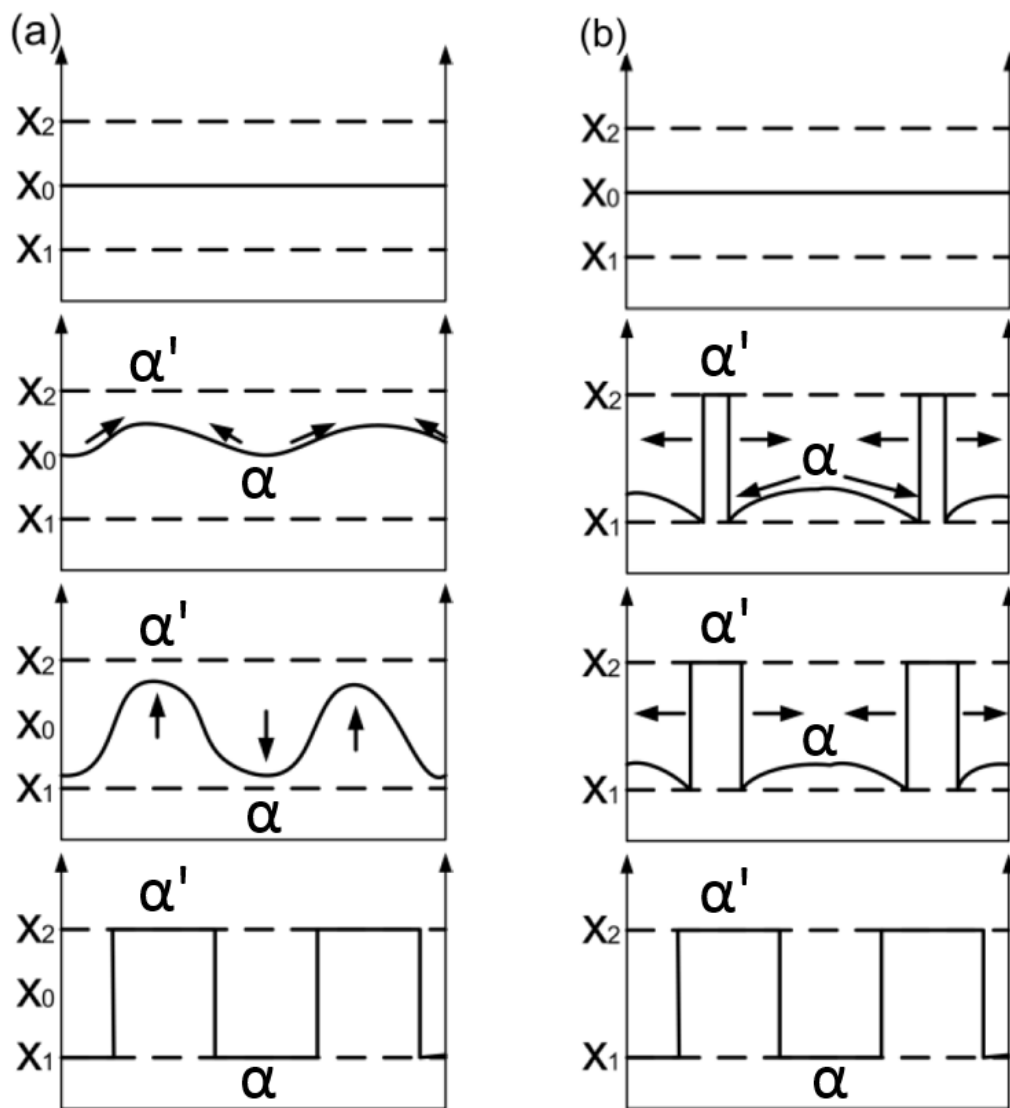


Figure 1-8. Comparison of (a) spinodal decomposition and (b) nucleation & growth. (Source: Ref. [35])

An early study performed by Miller [36] on Fe-Cr binary alloy used a field ion atom probe (FIAP) to identify the Cr rich  $\alpha'$  phase. However, the  $\alpha'$  phase was sometimes mistakenly interpreted as a precipitate during the 1990s. Chopra [16] studied CF-3 and CF-8 but reported no discovery of spinodal decomposition in the ferrite phase due to the precipitation interpretation. Many recent experiments performed on CASSs/welds have found spinodal decomposition in ferrite phase using atom probe tomography (APT) due to its atomic resolution. For a nucleation and growth process, the driving force is usually the Gibbs free energy  $\Delta G$  shown in Eq. 1-4.

$$\Delta G = \frac{4}{3}\pi r^3 \Delta G_v + 4\pi r^2 \gamma + \frac{4}{3}\pi r^3 \Delta G_\varepsilon \quad (1-4)$$

The first term,  $\frac{4}{3}\pi r^3 \Delta G_v$ , denotes the difference in chemical potential when a nucleus with radius of  $r$  is formed from the matrix. The term  $4\pi r^2 \gamma$  indicates the induced strain energy of the nucleus and  $\frac{4}{3}\pi r^3 \Delta G_\varepsilon$  denotes the corresponding surface free energy increase. Traditionally, precipitate forms via the sequence of G.P. zone  $\rightarrow \theta'' \rightarrow \theta' \rightarrow \theta$  following the step rule proposed by Ostwald [37]. The G.P. zone normally has exactly the same microstructure as the matrix, but slightly different chemical composition. The  $\theta''$ ,  $\theta'$  and  $\theta$  have exactly the same chemical composition but slightly different crystal structures with respect to the coherence level with the parent phase. Overall the composition difference between the precipitate and surrounding matrix is achieved via long range solid diffusion within the parent phase [38].

A more detailed phase transformation is illustrated step-by-step in Figure 1-9. The final  $\theta$  phase is different from the  $\alpha$  matrix in both chemical composition and microstructure. Instead of the  $\theta$  phase nucleating directly from the  $\alpha$  matrix with a large

activation barrier, precursors can be formed as a result of intermediate processes with much smaller formation barriers.

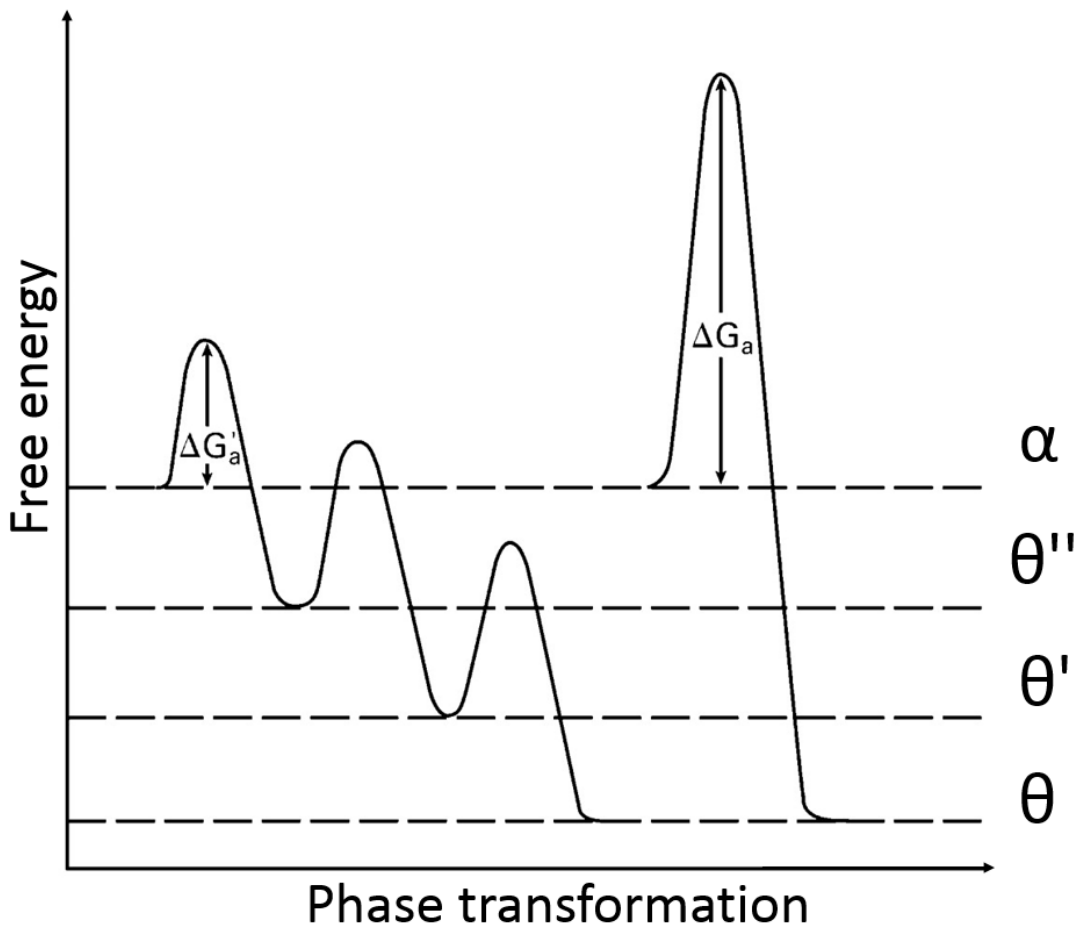


Figure 1-9. Ostwald step theory of precipitation behavior. (Source: Ref. [35])

In principle, the precipitate tends to nucleate along the grain boundary of the parent phase, where interfacial and strain energy can be well accommodated [40]. The name G-phase was given, as it was a new phase discovered at the grain boundary. This normally takes a long time, as both the crystal structure and chemical composition of the precipitate are quite different from the matrix. Thus, it was normally discovered in austenite when aged at high temperature. G phase precipitation is an intermetallic silicide. It has an F.C.C. structure with lattice parameter no greater than 1.14 nm

depending on chemical composition [1,39]. Its common clustering elements include Ni, Mn, Ti and Nb. As a secondary phase found in CASS/weld materials when aged at reactor operating temperature [25,41], G phase can strengthen the ferrite phase via precipitate hardening.

For CASS/weld ferrite, G phase is known to have a longer incubation time compared with spinodal decomposition when aging temperature is lower than 400 °C [39,42]. Thus, G phase formation is typically considered to rely on the spinodal decomposition process. Li [11] investigated DSS aged at 400 °C for 3000 h using TEM. He reported that G phase was not observed, as there was only one set of diffraction patterns in the ferrite matrix. It was further explained that the incubation time for G phase could be even longer than 3000 h at 400 °C.

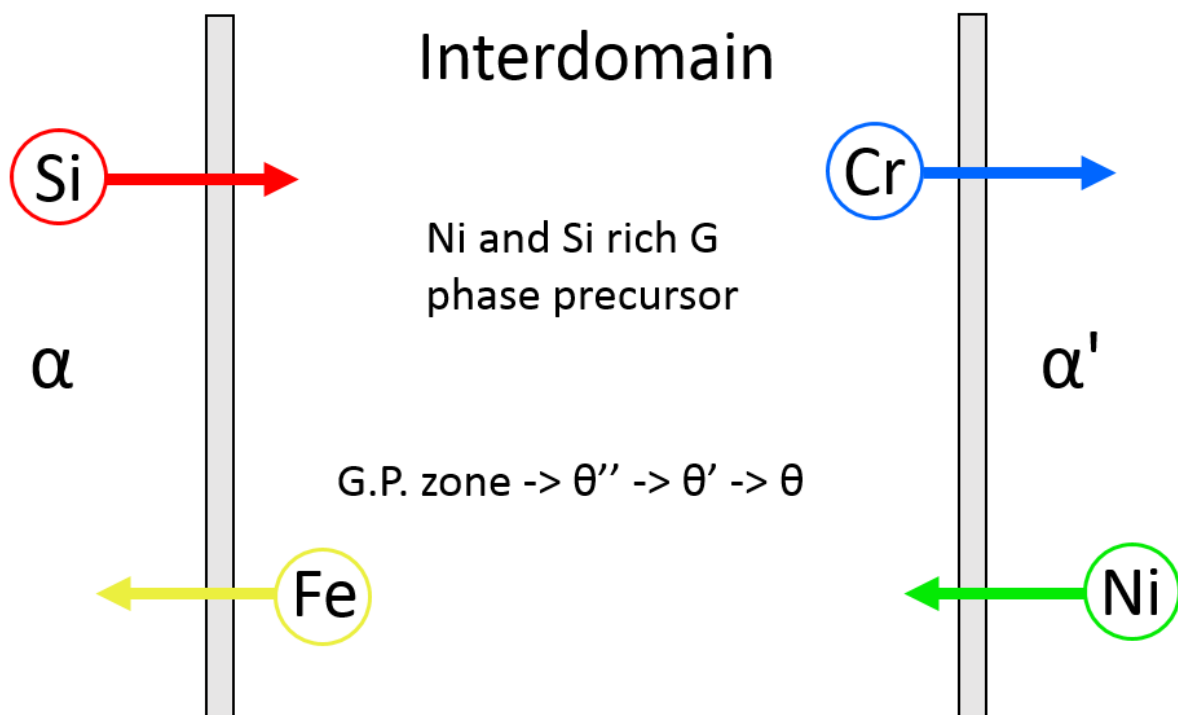


Figure 1-10. Flux of element during G phase formation and spinodal decomposition of ferrite. (Source: Ref. [39])

Spinodal decomposition is known to be a pivotal process for G phase precipitation. In fact, Mateo [39] proposed the correlation of G phase formation on spinodal decomposition in a model depicted in Figure 1-10. For Cr-rich  $\alpha'$  phase, Ni is expelled towards the phase boundary owing to its limited solubility. Likewise, Si is expelled from Fe-rich  $\alpha$  phase. The combined effect is that more and more Si and Ni atoms gather and accumulate at the interface region of an  $\alpha/\alpha'$  interconnected structure. To minimize the Gibbs free energy, a more stable G phase starts to nucleate out of those clusters. This assumption was further enhanced by Takeuchi [43] in his study on stainless steel welds.

### **1.3.3 Activation Energy Extraction of Aging Embrittlement**

Many mechanical tests have been performed to investigate the aging embrittlement at 400 °C and in the lower temperature range of 280 °C-320 °C on CASSs/welds. Pumphery [25] performed aging experiments on CF-3 in the temperature range of 300 °C- 400 °C, followed by the Charpy impact test. With an activation energy of 169 kJ mol<sup>-1</sup>, he concluded that aging at 350 °C for 11,200 h was sufficient to simulate the end-of-life service of 32 years at 294 °C for CF-3. Chemical composition may have a direct influence on the spinodal reaction. However, there was insufficient evidence showing that chemical composition can also influence the aging activation energy. Chung [19] further conducted both aging experiments and mechanical property tests over a wide temperature range on CF-3, CF-8 and CF-8M. It was summarized that accelerated aging at 400 °C can be used to evaluate aging at 280 °C - 340 °C. The accuracy was primarily determined by the aging activation energy, which can be affected by the chemical composition. In the meantime, Pareige [44] performed long-term aging experiments on CF-3M at 325 °C and 350 °C followed by mechanical property

tests. By using the equivalent time model, aging at 350 °C anticipated the same microstructural evolution as aging at 325 °C.

Experiments to extract the weld aging embrittlement activation energy were performed during the early 1990s by Grobner [9,45], Trautwein and Gysel [46] with inconclusive results ranging from 100 kJ mol<sup>-1</sup> to 230 kJ mol<sup>-1</sup>. Tavassoli [47] attempted to determine the aging activation energy of spinodal decomposition in the temperature range of 490 °C – 540 °C and reported an activation energy of 67 kJ mol<sup>-1</sup> at 490 °C. Vitek [41] further conducted aging experiments on 308L welds at an elevated temperature range from 400 °C to 550 °C. His results indicated that the aging kinetics of spinodal decomposition at 475 °C was the most rapid. Chandra's [29] group performed aging experiment on 304 and 316 weldment at 335 °C – 400 °C. They reported that aging at higher temperature tended to yield greater activation energy values compared with lower temperature range aging.

## **1.4 Motivation**

### **1.4.1 Nuclear Energy and LWRs Sustainability Program**

The Nuclear Regulatory Commission has licensed 99 LWRs which produce about 20% of the electricity in the United States over the past two decades. The LWRs contribute to more than 70% of the non-greenhouse gas emitting electric power generation. Over 75% of those LWRs are generation II reactors, reaching the end of their 60-year operating licenses. In the meantime, the domestic electricity demand is expected to grow at around 1% annually. If those nuclear power plants do not continue to operate beyond 60 years, more new power plants need to be built to meet the energy demand. To build a new advanced nuclear fleet can cost hundreds of billions of dollars. Traditional fossil plants are cheaper, but they will increase greenhouse gas emission

dramatically. In comparison, extending the current license lifetime of 60 years is a low-risk option and cost effective.

To ensure that the current LWRs can be operated safely, reliably and economically, the Office of Nuclear Energy has identified four R&D pathways within the LWR sustainability frame. They are material aging and degradation, advanced LWR nuclear fuel, advanced instrumentation, information and control system technologies and risk-informed safety margin characterization.

The goal of the material aging and degradation pathway is to develop a scientific basis for better understanding and more accurately predicting the long-term environmental degradation behavior of the primary system, structure and components in LWRs. The program will provide data and methods to assess LWR performance which is essential to their safe and reliable operation.

#### **1.4.2 Challenges of Neutron Irradiation Enhanced Aging Degradation**

CASSs and welds in LWRs are susceptible to aging embrittlement in the service temperature range of 280 °C -320 °C. The aging behavior of CASS/weld has been well established in the past two decades, as discussed in Section 1.3. Specifically, for the low-carbon steel CF-3 when aged at elevated temperature, an obvious characteristic ductile-brittle transition phenomenon of its impact energy can be observed as shown in Figure 1-11. Both a decrease in upper shelf energy and an increase of ductile-brittle transition temperature indicate the embrittlement tendency. Fortunately, if only considering the designed 40-year lifetime at reactor operation temperature, the corresponding impact energy of CF-3 is still quite high to guarantee its safe and reliable functionality.

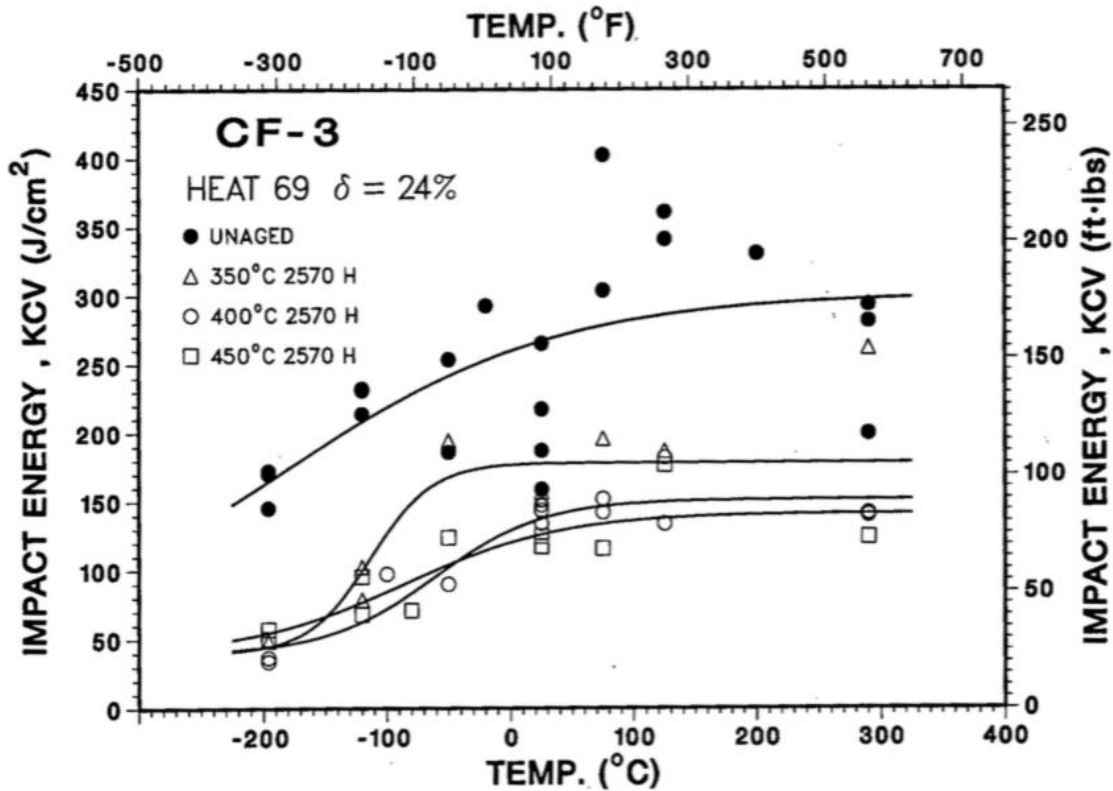


Figure 1-11. Full size Charpy V-notch impact energy of CF-3. (Source: Ref. [17])

As shown in Figure 1-12, some CASS components, such as core support columns and mixing devices, may be exposed to neutron irradiation with fluence level on the order of  $10^{20}$  n/cm<sup>2</sup> ( $E > 1$  MeV) when considering an extended service lifetime of 80 years. For the current 60 years of service, the neutron irradiation dose on those CF series steels can range from 0.01 displacement per atom (dpa) up to more than 10 dpa. Thus, it is quite important to establish the corresponding irradiation responses of those service components. As pointed out by Chopra [48], current data on neutron irradiation damage is more focused on dose level between 1 dpa – 5 dpa. More data points are needed in the dose level range of less than 0.1 dpa to greater than 5 dpa.

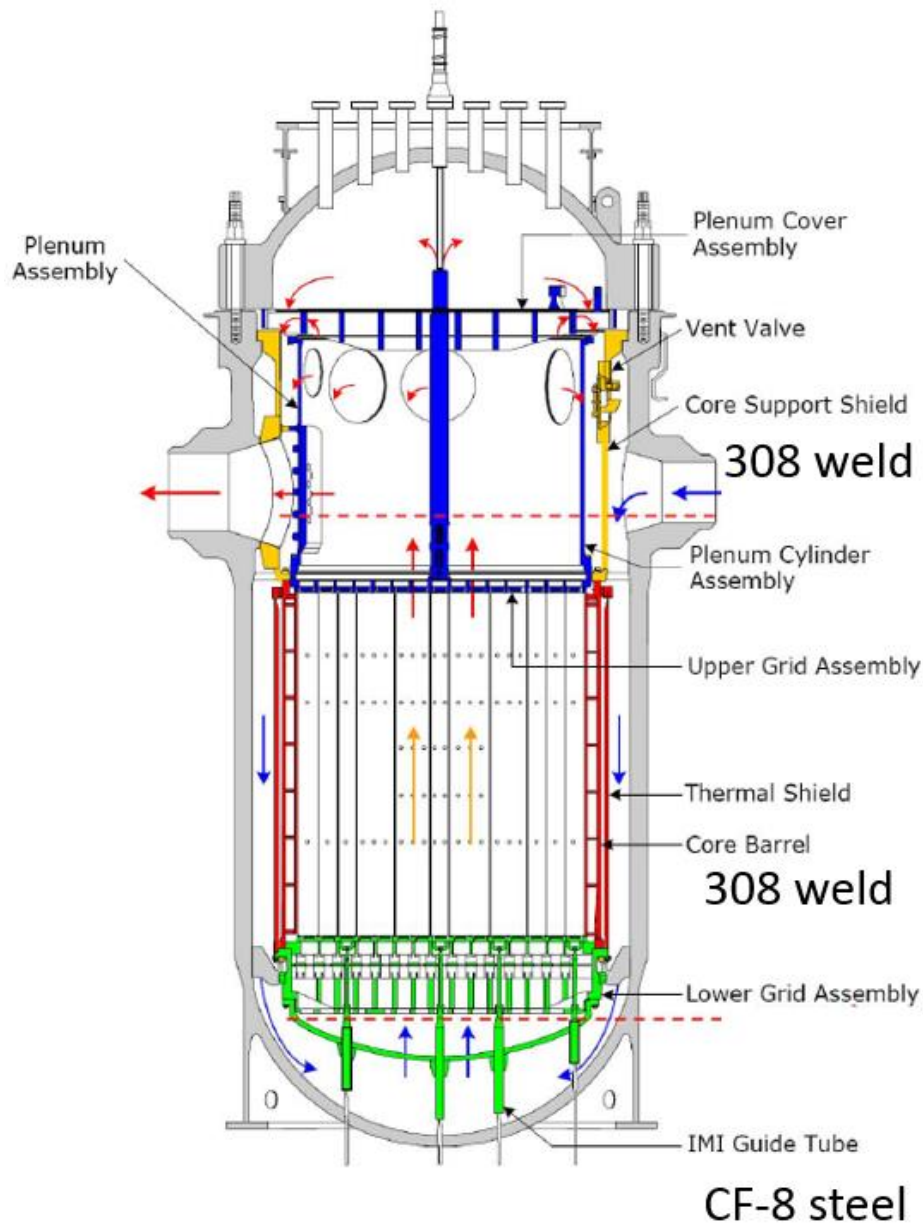


Figure 1-12. Application of CASS/weld in reactor core internals. (Source: MRP-276)

The stainless steel welds in the LWRs are also exposed to neutron irradiation to a relatively lower dose as compared with reactor core components. As noted by the ERPI technical reports MRP-276 summarized in Table 1-4, the welds can be in the high fluence regions of the PWR internals (e.g. core barrel welds and flux thimble tube plugs). The anticipated neutron fluence can be on the order of  $10^{22}$  n/cm<sup>2</sup>. There are

several studies regarding the neutron irradiation effect on the fracture property of stainless steel welds [49,50]. TEM examinations conducted by Lee et al [51] could not reveal the nature of fine defects, even though micro-hardness tests showed a significant hardening in the  $\delta$ -ferrite phase after irradiation. Takeuchi [43] observed the neutron irradiated microstructures in a stainless steel electro-slag weld overlay irradiated to ~around 1 dpa at 290°C. A slight progression of Cr spinodal decomposition and an increase in the fluctuation of the Si, Ni, and Mn concentrations were observed in the ferrite phase. Nevertheless, related microstructural studies, particularly at LWR-relevant conditions are very limited.

Table 1-4. Component serviced in PWRs with CASSs and weld. (Source: MRP-276)

Components	Grade	Irradiation fluence ( n/cm <sup>2</sup> , E>1.0 MeV)	Potential concerns
CRGT assembly spacer castings	CF-3M	10 <sup>20</sup>	Thermal embrittlement
CSS assembly cast outlet nozzles	CF-8	10 <sup>17</sup>	Thermal embrittlement
CSS assembly vent valve discs	CF-8	10 <sup>17</sup>	Thermal embrittlement
IMI guide tube assembly spiders	CF-8	10 <sup>20</sup>	Thermal and irradiation embrittlement
Core barrel	ASA with 308L	10 <sup>20</sup>	Irradiation embrittlement
Core support shield	ASA or AMA with 308L	10 <sup>18</sup>	Irradiation embrittlement
Lower grid	STIG with 308L	10 <sup>20</sup>	Irradiation embrittlement

### 1.4.3 Comparison of Thermal Aging and Neutron Irradiation Validation

High-energy neutron irradiation can introduce point defects in materials at varied rates and densities depending on the irradiation parameters. Subsequent thermal diffusion of these point defects can lead to a healing process. This occurs when the

interstitials and vacancies recombine with each other or sinks in the materials and become annihilated. Eventually, the point defects reach a dynamic equilibrium level owing to the continuous neutron irradiation. Such irradiation-induced defects will have a wide variety of effects on the materials with respect to microphysics and microchemistry, such as thermodynamic equilibrium, transport kinetics and local disordering.

Based on the theory and experiments by Was and Rothman [52,53], the aforementioned equilibrium density of vacancy tends to dramatically outgrow that of interstitial by a few orders of magnitude at low irradiation temperatures. Such high-density vacancy can enhance the diffusion kinetics in many ways. Usually when competing with thermal diffusion at the same temperature, irradiation enhanced diffusion tends to be much faster. As a result, microstructure evolution, such as phase decomposition, under irradiation will become more rapid compared with the slow transformation under thermal aging conditions.

#### **1.4.4 Synergistic Effect of Irradiation and Thermal Aging on Ferrite Decomposition**

The synergistic effect of thermal aging and neutron irradiation on ferrite phase decomposition was first introduced by Miller [36] in 1996. He concluded that neutron irradiation could facilitate the spinodal decomposition at a very low dose of 0.03 dpa in Fe-32% Cr alloy. For core internal components exposed to neutron irradiation, this irradiation-enhanced thermal aging can bring more inaccuracy to the evaluation of aging embrittlement. Thus, it is critical to carry out more experiments to study the effect of irradiation enhancement on the degradation of those components.

Ideally, to study the synergistic effect of thermal aging and neutron irradiation on the ferrite phase, the material needs to be exposed to the actual working environment in a nuclear reactor. Thus, the thermal aging and irradiation can affect the microstructure simultaneously and interactively. Unfortunately, it is impractical to pursue a real-time aging experiment for 60 years or longer. In many cases, thermal aging has to be accelerated at a higher temperature to complete the experiment in a reasonable period. It has been reported that the activation energy of spinodal decomposition in a Fe-Cr system has a wide range of 164 to 324 kJ/mole [44,54]. By considering the low end of activation energy of 164 kJ/mole in a conservative manner, 10,000 hours aging at 400°C will correspond to 79 years of service at 315°C in a PWR. To further study the synergistic effect of neutron irradiation and thermal aging, a neutron irradiation experiment can be performed on the aged materials. This method can provide a scientific insight for the understanding of the combined effect of thermal aging and neutron irradiation.

#### **1.4.5 Micro Scratch Test for Fracture Toughness Extraction**

With the development of the atom probe tomography (APT), transmission electron microscopy (TEM) and focused ion beam (FIB) techniques, the microstructural characterization of the CASS/weld can be systematically performed. However, it is very important to correlate the microstructure results with the corresponding changes in mechanical properties, such as hardness, tensile strength and fracture toughness. Due to the dimension limit of the materials available in this research, it was quite impractical to carry out mechanical testing, such as impact energy testing. Such testing typically requires a large dimension specimen, which is very material consuming. With the development of the micro scratch test for fracture toughness characterization, the

sample preparation requires only a tiny dimension as big as the fingernail. Such testing is a perfect match of the weldment samples in this study.

### **1.5 Summary**

CASSs and stainless steel welds have been extensively used in LWRs as primary pressure boundaries and core internal components. They both have a duplex structure of the ferrite phase surrounded by the austenite matrix. Ferrite plays a major role in enhancing the strength, stress corrosion cracking and weldability. However, during the designed 40 years of service of LWRs, ferrite is susceptible to thermal aging-induced phase decomposition.

Recently both industry and regulators have strong incentives to extend the service lifetime of LWRs to 80 years. As part of the material aging and degradation research and development program, this study is dedicated to perform a systematic study of the CASS/weld. Scientific data and analysis are established to help regulators perform better and more accurate assessment and evaluation on the licensing of LWRs. The scope of this research is mainly focused on structural characterization of CASS/welds, low strain rate mechanical property testing and interpretation, along with subsequent structure-property relationship investigation, such as the strengthening mechanism. The high strain rate fracture behavior of the materials is also included.

## CHAPTER 2 EXPERIMENTAL DETAILS

### 2.1 Materials and Treatment

CF-3 steels were selected from the ANL research program [17,55] with heat batch number 69. This batch of CF-3 was static cast slab with dimensions of 610 mm x 610 mm x 76 mm by Foundry of ESCO Corporation following ASTM A351. The slab dimensions were close to that of the pump impeller used in LWRs with Rockwell hardness of 83.7. The slab contained approximately 23% volumetric fraction of delta ferrite measured by ferrite scope AUTO Test FE with probe type FSP-1. The documented average ferrite spacing was around 35  $\mu\text{m}$ . The chemical composition of CF-3 cast slab used in this study is listed in Table 2-1.

All the CF-3 samples used in this study were obtained from the interior region of the same cast slab. Bulk materials were sectioned from cast slab and further sliced into small cuboid plates with dimensions of 0.25" x 0.5" x 0.5". Some of the bulk materials were further thermally aged. The thermal aging experiment was carried out at 400°C for 10,000 hours in a box furnace. A Dualscope FMP100 was further used to measure the ferrite content of the CF-3 bulk samples via the magnetic induction method. Probe FGAB1.3-Fe was used with a detection limit of 0.1%. Fifteen fields were analyzed for the measurement on unaged and aged CF-3 used in this study. The measured ferrite content is 23.6% which is very close to the measurement by Chopra's report [17].

Table 2-1. Chemical composition (wt. %) of the cast stainless steel CF3. (Ref. [17])

Ni	Si	P	S	Mn	C	N	Cr	Mo	Fe
8.59	1.13	0.015	0.005	0.63	0.023	0.028	20.18	0.34	Bal.

Some of the un-aged and aged CF-3 plates were further ground and polished down to around 150 mm and punched into 3 mm discs using a disc punch from SPI

Supplies with model type 17001-AB. Both surfaces of the disc were jet polished to remove the polishing strain layers. The discs were further sealed into a helium-filled capsule to be irradiated in the reactor. The neutron irradiation experiment was conducted in the Halden reactor in Norway. The irradiation temperature was controlled at 315 °C with two sets of melting alloy temperature monitors installed in the irradiation assembly. Due to limited access to the post-irradiated samples, metallography of the irradiated samples is not available.

During the irradiation experiment, three fluence monitor wires (Fe, Ni, and Al/Co alloy) were placed outside the irradiation capsule. After irradiation, dosimetry reading was performed by the Halden reactor researchers based on these monitors. Using the activation cross sections determined previously, the accumulated neutron fluence for the irradiation capsule could be estimated. The obtained fast neutron fluence ( $E > 1$  MeV) was about to  $5.56 \times 10^{19}$  n/cm<sup>2</sup>, with a dose rate of  $2.8 \times 10^{-9}$  dpa/s, corresponding to a displacement damage of 0.08 dpa for the sample [55].

To simulate the irradiation under extreme condition, CF-3 discs in as-cast condition were kept in 3 mm capsules, which were further placed in a BOR-60 reactor for neutron irradiation. The irradiation temperature was controlled at  $315 \pm 2$  °C. The irradiation damage calculation was performed by Research Institute for Atomic Reactors [56]. The irradiation dose rate was estimated at  $10^{-6}$  dpa/s.

An ASTM 304L stainless steel weldment fabricated with ER308L filler metal was used in this study. The chemical composition of the weldment used is shown in Table 2-2. The 304L stainless steel plates were welded following a conventional submerged arc butt-welding procedure with a double-V joint design. The parameters for each weld pass

were documented in the data package, including current, voltage, travel speed, heat input and so on. Only the property of the 308L fusion zone was considered for the environmental degradation evaluation in this study. The measured ferrite content of the fusion zone was  $13.5\pm 0.5\%$  using Feriscope FMP100. Some of the weldment joints were thermally aged at 400 °C for 2,226 hours and 6000 h.

Table 2-2. Chemical composition (wt.%) of 308L weld fusion zone

C	Mn	P	S	Si	Ni	Cr	Mo	Ti	Fe	N
.023	2.06	.032	.006	.92	9.30	20.50	.10	<.01	Bal.	.10

## 2.2 OM & SEM Metallography

A Tagremin-25 polisher with SiC sand paper was used for the surface polishing finished with 1200 grit (P4000, 2.5  $\mu\text{m}$ ) for the non-irradiated CF-3 steels and 308L weldment specimens. All grinding and polishing procedures followed the microprobe polishing standard by Fynn and Zipperian [57,58]. After fine polishing with 1  $\mu\text{m}$  diamond slurry, the surfaces were etched with ferric chloride balanced with hydrochloric acid for a few seconds following the guide for special alloy etching [59–61]. Due to the limited access to the neutron-irradiated 3 mm CF-3 disc, the metallographic image of irradiated specimens has not been prepared. Further SEM images should be prepared in the future to clarify the structural stability of CF-3 under irradiation conditions.

The CF-3 steel specimens used were in as-cast condition with no prior heat treatment history. Typically, heat treatment, such as solution annealing, is performed to remove the macro-segregation and carbide precipitate, and to control ferrite content. The measured ferrite content stayed relatively the same throughout this research for CF-3. As concluded by Li [11], solution annealing on cast stainless steels has little

impact in the subsequent aging kinetics at lower temperature. Thus, use of CF-3 casting with no heat treatment in this study is fully justified.

A Bruker XFlash 6|30 EDS on a Tescan LERA3 Xe plasma source FIB/SEM was used for chemical composition analysis in this study on the unaged CF-3. The accelerating voltage used was 15 kV with a working distance at 30 mm. The spot size used was 13 nm. At least five different measurements were performed for the unaged CF-3. The EDS result is shown in Chapter 3.

### **2.3 TEM Crystallography and Characterization**

Around 2 mm thick slices of 308L weld were prepared from the fusion zone. The sectioning plane was parallel to the welding surface. The slices were further ground and polished to around 150  $\mu\text{m}$  chips, which were punched into 3 mm discs using a SPI Supplies disc punch. Those discs were further electropolished using a single jet polisher with model type M-550. Specimens were finished with central perforation size of  $100\pm 30$   $\mu\text{m}$ . The transparent region adjacent to the perforation was thin enough for TEM investigation. The electrolyte used was 10% perchloric acid balanced with methanol. A cold bath was used with dry ice mixed with methanol. The bottom part of the plastic bucket of the polisher was submerged in the cold bath. The temperature of the electrolyte was maintained at  $-18\pm 2$   $^{\circ}\text{C}$  measured by a thermometer during the experiment. TEM specimens of the irradiated CF-3 steels and welds were prepared using FEI Quanta 3D FEG FIB on the 3 mm irradiated discs. A typical TEM specimen fabricated using FIB is shown in Figure 2-1. A Tecnai G2 F30-FEG TEM in Idaho Falls, Idaho National Lab (INL) was used to characterize the microstructure of ferrite phase with an acceleration voltage of 300 kV.

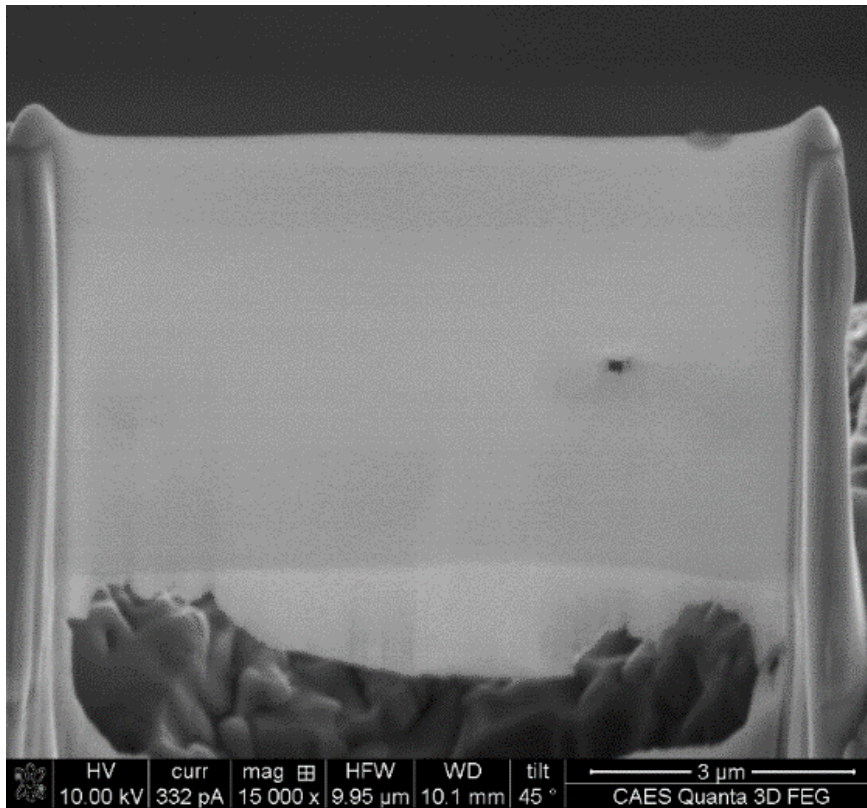


Figure 2-1. SEM images of a typical TEM sample on the grid fabricated using FIB.

#### 2.4 Atom Probe Microstructural Characterization & Analysis

With the objective of developing a fundamental understanding of ferrite microstructure evolution, characterization was focused on the development of spinodal decomposition and G-phase precipitation. Because of its atomic resolution [62,63], APT examination was extensively used to quantify the redistribution of Cr element in the ferrite phase and the fine precipitates.

Chips with thickness around 2 mm were sectioned from the bulk CF-3 and weldment fusion zone using a high speed diamond saw. A Techcut-5 high speed diamond saw from Allied high tech was selected for the experiment, and a diamond wafering blade with diameter at 6" and thickness at 0.02" was used. The rotation speed of the wheel was set at 3000 rpm, and the feeding speed used was 0.05"/min. Chips

were further ground to 150  $\mu\text{m}$  - 200  $\mu\text{m}$  using the Tegramin-25 polisher to remove the abrasive cutting damage layer. The final step of sample surface grinding was finished with 800 grit sandpaper. A 3 mm disc punch from SPI Supplies with model type 17001-AB was used to fabricate 3 mm discs from the steel chips. The sample surfaces were further etched using a jet polisher from Southbay Technology M550 to reveal the ferrite and austenite phase boundary. Each surface was polished with a 1.5 mm nozzle for 100 s at  $-18\pm 2^\circ\text{C}$  with a voltage and current at 75 V and 100 mA, respectively, in a mixture of 10% perchloric acid balanced with methanol.

The discs prepared for irradiation were electropolished to reveal the ferrite and austenite phase boundary in ANL. A jet polisher with model type of Struers Tenupol-5 was used. Each surface was polished with a 1.5 mm nozzle for 100 s at  $-18^\circ\text{C}$  with the voltage and current at 75 V and 100 mA, respectively. Electrolyte was a mixture of 5% perchloric acid balanced with methanol. After irradiation experiment, the 3 mm discs were shipped back to ANL from the reactor sites. After a few more safety protocol communications between ANL and INL, irradiated samples were transported from ANL to INL user facility for microstructure characterization.

In INL, APT tips were prepared for both CF-3 steels and 308L weldment using FEI Quanta 3D FEG FIB focused on the ferrite phase of the 3 mm etched disc. Samples were finished using low energy ion beam cleaning with voltage of 2kV and current of 27pA to ensure a minimal Ga implantation. For each condition of CF-3 steels and 308L weldments, a minimum of seven tips were fabricated.

The atom probe experiment was carried out in a local field atom probe (LEAP) 4000 XHR at 55 K with ion detection efficiency at 37%. The laser pulse rate was set at

200 kHz with pulse energy at 60 pJ. The detection rate was kept between 0.1% - 0.5% to allow for large dataset collection. The 3-D reconstruction and analysis were performed using integrated visualization analysis software (IVAS) 3.6.8 following the standard procedure of the Recon Wizard in IVAS. SEM tip images were used for defining tip profiles. The evaporation field value was 33.0V/nm and a k factor of 3.30 was used. The FIB and APT instruments used for this study are both located in the Microscopy and Characterization Suite (MaCS), Center for Advanced Energy Studies (CAES) in Idaho Falls, Idaho. More details of the APT sample fabrication and LEAP experiment can be found in Appendix A.

To quantify the nanoscale spinodal decomposition in ferrite phase, the frequency distribution, radial distribution function (RDF) and Cr proxigram techniques were used to determine the degree of spinodal decomposition, the wavelength and the amplitude.

#### **2.4.1 Frequency Distribution**

The frequency distribution technique is often used to roughly analyze the extent of spinodal decomposition in ferrite phase. The procedure included indexing all the identified solute ions, which were evenly divided into boxes with a certain number of ions (100/box in this study) that best reflects the distribution trend. For each 100-ion box, the concentration of Cr was calculated. The concentrations of all the boxes were histogrammed from 0-100% to generate the frequency distribution of Cr. Figure 2-2 shown a Cr frequency distribution of ferrite in DSS with aging time from 1 h to 1000 h at 450 °C. The Cr map is also illustrated in Figure 2-3. As can be observed, with the increase of aging time, the extent of Cr clustering behavior became greater. As a result, the peak shift and peak broadening in Figure 2-2 are typically used to reflect this Cr distribution evolution trend. A peak shift towards lower Cr concentration indicates the

formation of a Cr depletion region. On the other hand, the peak broadening towards the higher Cr concentrations is representative of the Cr rich clusters.

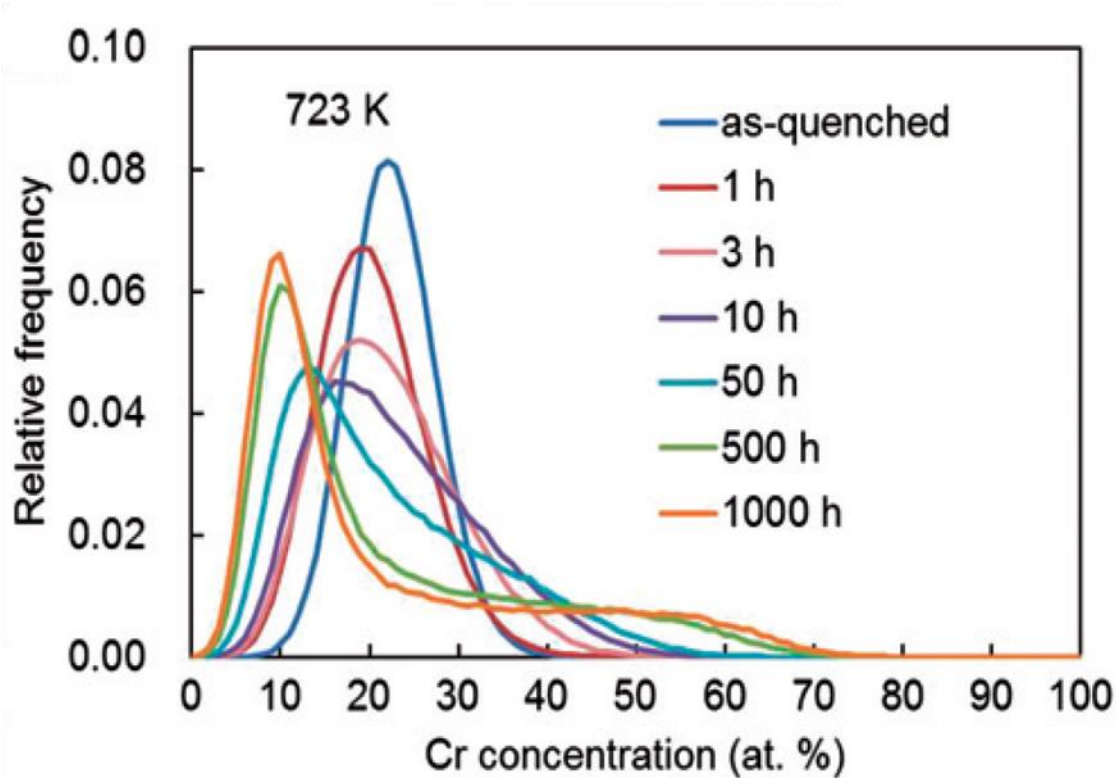


Figure 2-2. Cr frequency distribution of ferrite in DSS with varied aging time. (Source: Ref. [64])

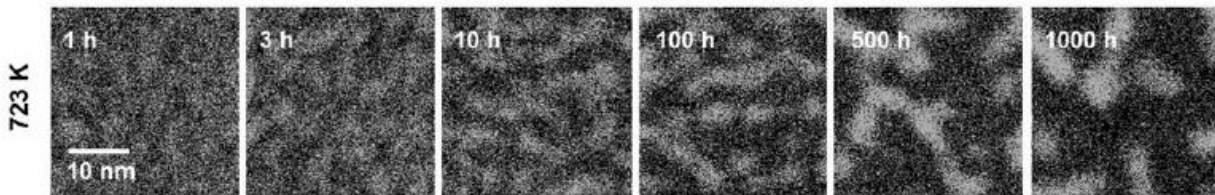


Figure 2-3. Cr map in ferrite phase in DSS with varied aging times. (Source: Ref. [64])

### 2.4.2 Radial Distribution Function

The RDF method calculates the Cr concentration distribution as a function of radial distance from each referenced Cr ion. The clustering tendency can be revealed based on the fluctuation of the RDF. The RDF method provides a unique quantitative evaluation on spinodal decomposition as compared with other methods, (e.g. 1D

concentration profiles and frequency distribution), because it provides a 3-D analytical perspective by including all the identified Fe or Cr ions.

Input parameters used to perform the RDF calculation in IVAS include the original reference ion type, bin width (nm) and maximum distance (nm). For Cr distribution fluctuation analysis, each and every detected Cr ions in the dataset is settled as the center reference ion [62]. By default, the maximum analysis distance is 10 nm. The bin width, as the increment, ranges from 0.01 nm – 1 nm, with 0.2 nm often used to best reveal the Cr clustering behavior without introducing too much noise. The algorithm calculates the shell concentration and generate a histogram based on the bin width.

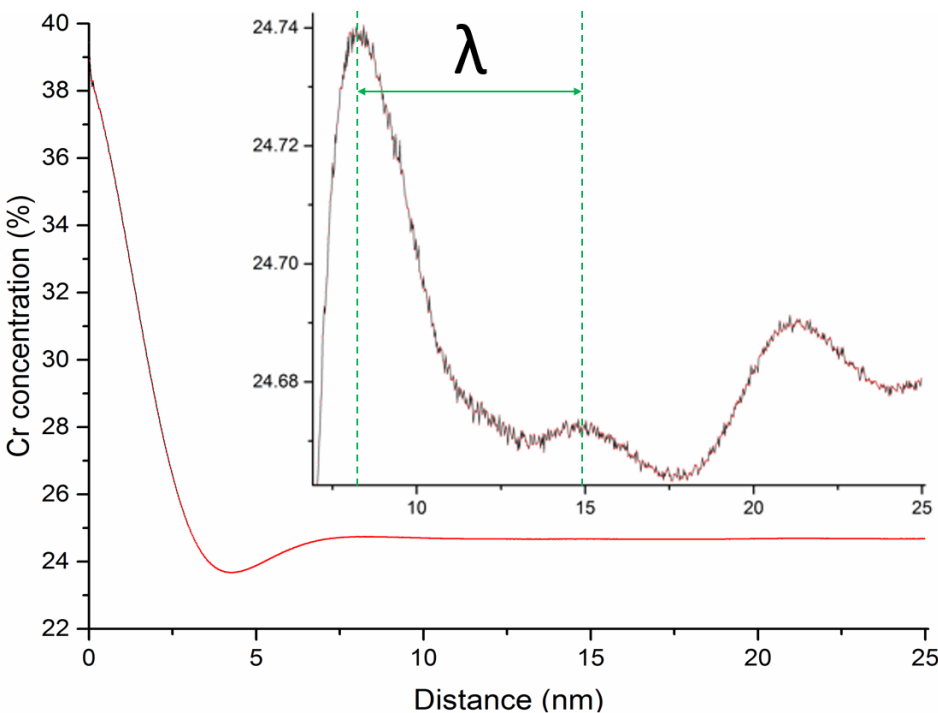


Figure 2-4. Typical RDF plot of Cr-Cr of ferrite in aged CF-3.

Figure 2-4 shows a typical Cr-Cr RDF curve for the ferrite phase in the aged CF-3. The inset in Figure 2-4 highlights the wavelength between two maxima. The

maximum indicates a statistically closest distance between two Cr-rich regions, and corresponds the Cr concentration fluctuation wavelength. We can assume Cr concentration as a sinusoidal wave function [34]:

$$f(\vec{r}) = C_o + \frac{A}{2} \cdot \sin\left(\frac{2\pi}{\lambda}\right)(\vec{r}) \quad (2-1)$$

where,  $C_o$  is the average Cr concentration in ferrite phase,  $A$  is the concentration fluctuation amplitude,  $\lambda$  is the wavelength, and  $\vec{r}$  is a position vector.

### 2.4.3 Proxigram of Cr Map

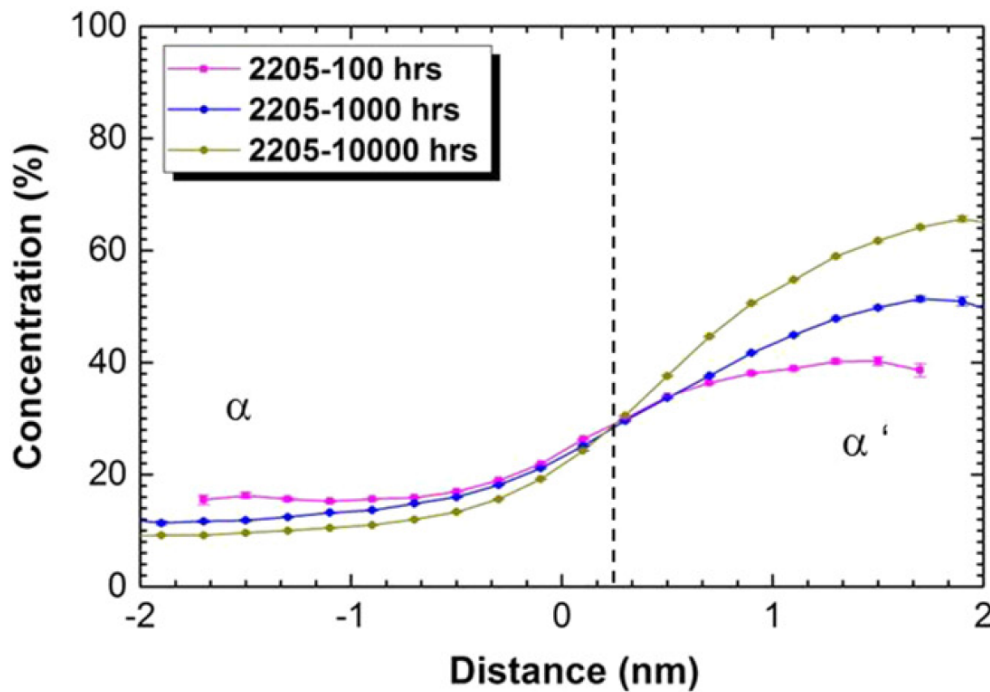


Figure 2-5. Typical proxigram of Cr of spinodally decomposed ferrite. (Source: Ref. [67])

The so-called proxigram is a combination of the proximity and histogram techniques in performing concentration profile calculations. A Traditional 1-D concentration profile is typically calculated along a certain axis of the cuboid or cylinder. Proxigram, however, computes the concentration profile along varied distances from a reference geometric surface. As long as there is a reference surface, proxigram can be

applied for the analysis. It is capable of visualizing the gradual demixing phenomenon of the Cr and Fe system. Thus, it is very useful for the amplitude and concentration profile study. The first publication using this technique is shown in Figure 2-5 by Poplawski's [65] group from Oak Ridge National Lab (ORNL). A smooth Cr concentration profile shifting from the left side of the  $\alpha$  phase towards the right side of the  $\alpha'$  phase was demonstrated. This can be interpreted as evidence of the diffusing interface formed due to the spinodal decomposition in ferrite.

#### 2.4.4 Cluster Analysis

To quantify precipitates in ferrite decomposition, a cluster analysis tool is used in IVAS software on the APT data. Parameters of "ions" (element), "orders" (ions), "erosion distance  $d_e$ ", " $d_{max}$  (nm)", " $N_{min}$ " and "envelop parameter  $L$  (nm)" have to be specified during the analysis. Maximum separation method (MSM) is one of the commonly used approaches to determine the optimal values of the parameters. The actual application of this method in this study is focused on the G phase cluster detection and identification. G phase is typically enriched in Ni, Si and Mn. With the help of this method, the size, density, chemical composition and volume fraction of the G phase clusters can be quantified. A typical procedure on how to carry out the analysis is described in the following paragraph.

Based on the preliminary analysis, Mn ions showed the best distribution contrast between matrix and clustered regions. Therefore, it was chosen as the ion for determining the solute cluster regions to select the desired orders (ions). The Mn-Mn nearest neighbor distributions for orders of one to ten are plotted in Figure 2-6, which shows that 4<sup>th</sup> order of nearest neighbor starts to show a clear separation of ions between matrix and cluster regions. The left peak represents the ions in cluster regions

and the right peak represents the ions in a more diluted matrix regions. The 4<sup>th</sup> order nearest neighbor distribution was then fitted using two Gaussian distributions, as shown in Figure 2-7. The value of  $d_{max}$  is determined as the distance between zero and the crossover of two fitted Gaussian distributions. The value of  $d_e$  is the distance between the peak of the left Gaussian distribution and the crossover of two Gaussian distributions. As suggested by Y. Chen et al. [66], envelope parameter  $L$  equals  $d_{max}$ . To determine parameter  $N_{min}$ , the minimum of ions in a cluster was counted in the analysis. The curve of identified cluster number vs  $N_{min}$  is plotted in Figure 2-8. As can be seen, a reasonable choice for  $N_{min}$  is 20, which eliminates clusters containing only a few atoms while giving a stable number of clusters, as increasing  $N_{min}$  does not significantly change the number of clusters. The precipitate model in this method uses the maximum distance of constituent ion positions along each of the precipitate axes instead of radius of gyration. Figure 2-9 reveals the results of the 2,226 h aged 308L ferrite G phase cluster size and density evaluation using the cluster analysis method. A mean size of 2.8 nm and number density at  $6.9 \times 10^{23}/m^3$  were identified based on the calculation.

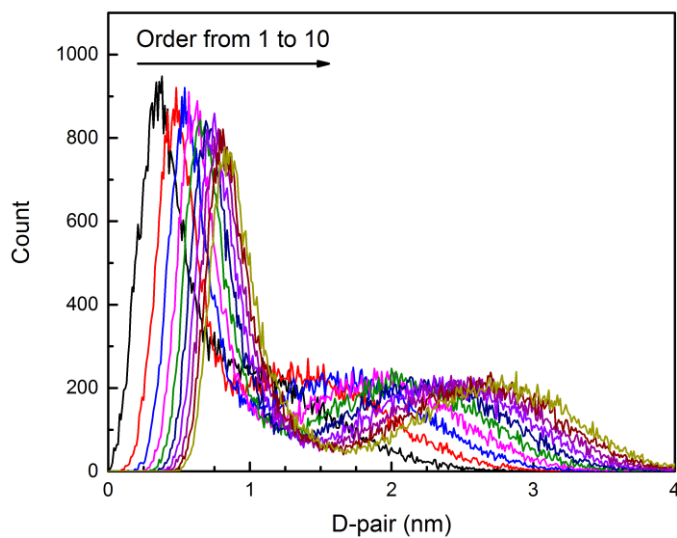


Figure 2-6. Mn-Mn nearest neighbor distributions for orders from 1 to 10

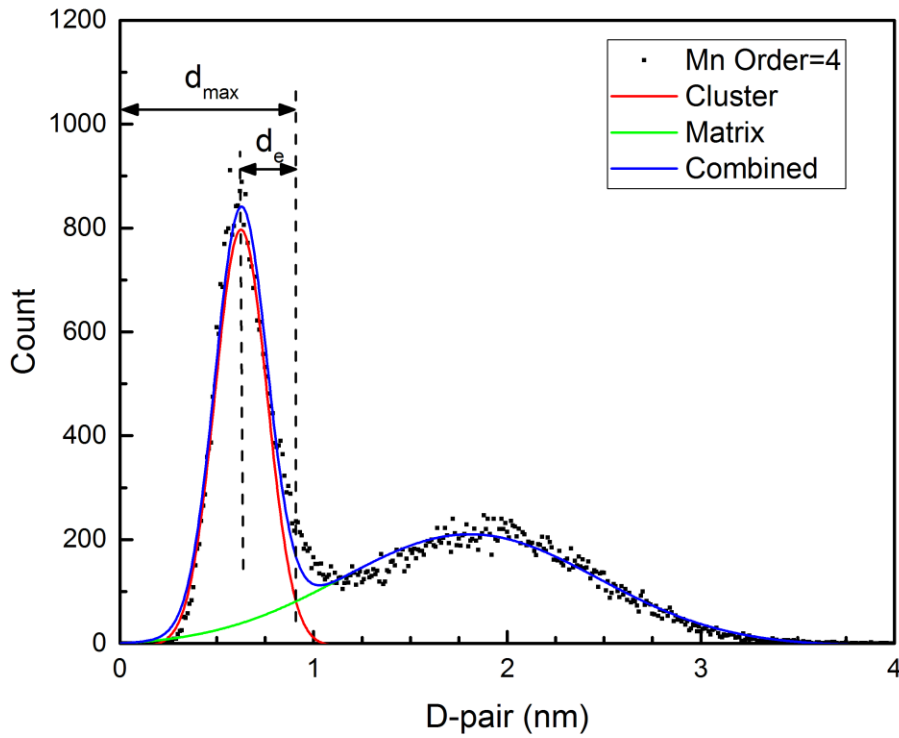


Figure 2-7. Gaussian peak deconvolution for the 4th order nearest neighbor distribution and determination of  $d_{max}$  and  $d_e$

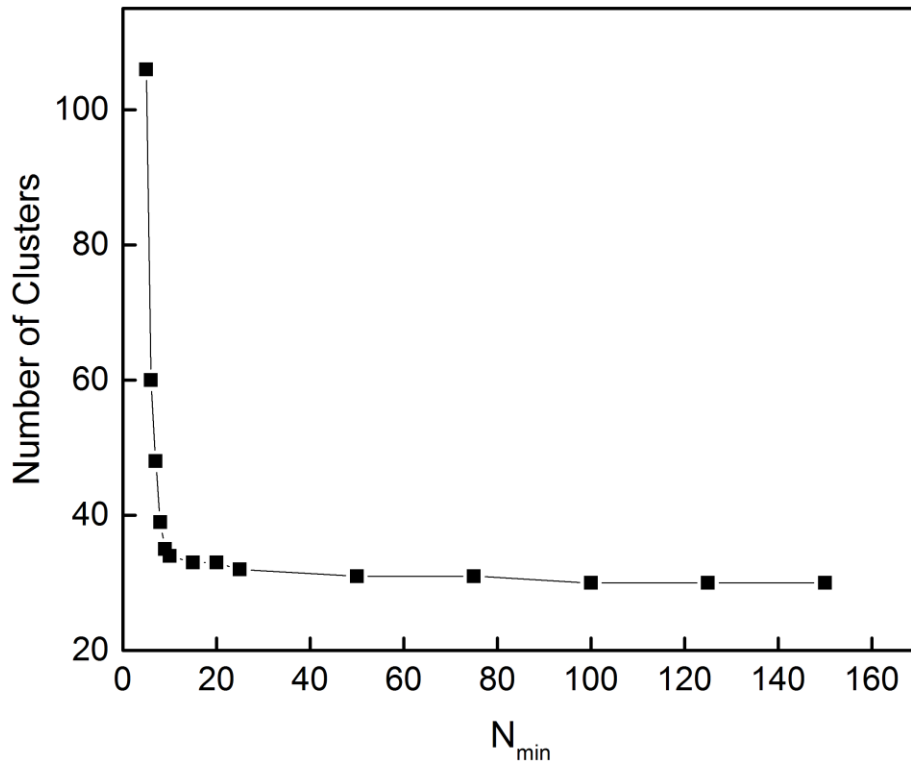


Figure 2-8. Cluster analysis parameters selection of the  $N_{min}$  in MSM.

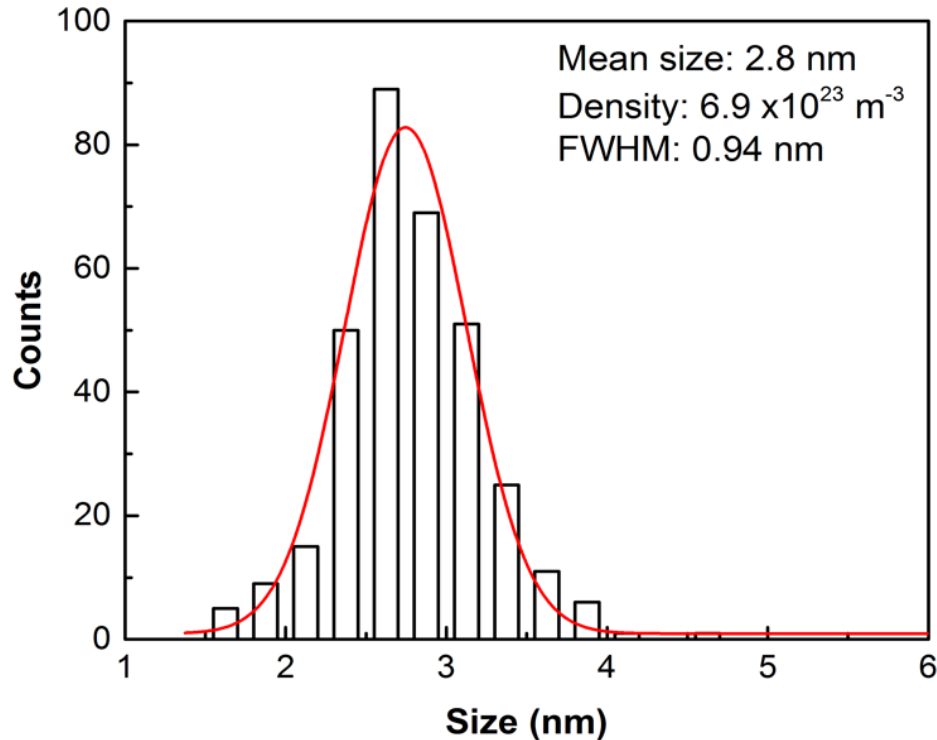


Figure 2-9. Cluster analysis results of ferrite in 308L weld aged for 2,226 h at 400 °C.

## 2.5 Mechanical Property Testing

### 2.5.1 Nano-indentation Test

Nano indentation has the advantage of using nano-sized indentation over a small area of interest to obtain hardness and Young's module. Chips with thickness around 1 mm were sectioned from the bulk weldment fusion zone using the high speed diamond saw mentioned previously. The feeding speed used was 0.05"/min to minimize cutting damage. Chips were further ground to 150  $\mu\text{m}$  - 200  $\mu\text{m}$  using the Tegamin-25 polisher. The polishing paper used was all SiC in 10". The final step of sample surface grinding was finished with 800 grit sandpaper (P2400, 6.5  $\mu\text{m}$ ). A 3 mm discs punch from SPI Supplies was used to fabricate 3 mm disc from the thin chip. To remove the surface strain induced by the abrasive polishing, the sample surface was further etched using a jet polisher from Southbay Technology M550. The electrolytic etching was

performed with a 3 mm nozzle for 5 s at -20°C with voltage and current at around 75 V and 100 mA, respectively. Electrolyte was a mixture of 10% perchloric acid balanced with methanol. A Nikon Eclipse LV100 optical microscope was used to examine the sample surface and a digital camera from Digital Sight SD-U3 was used for imaging.

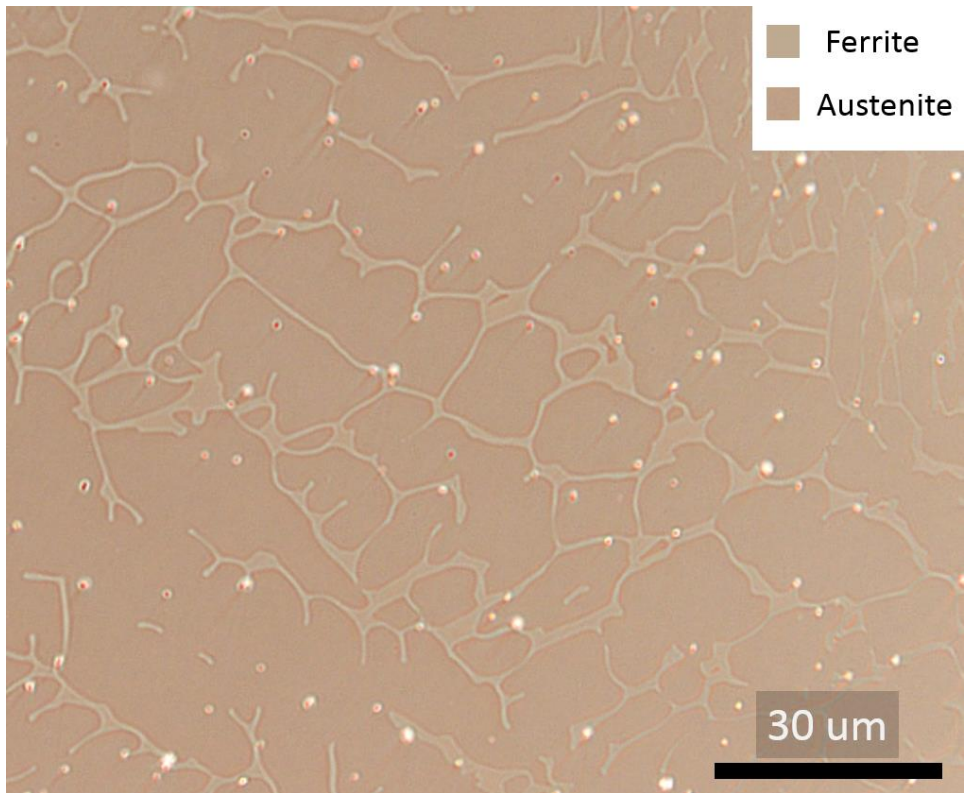


Figure 2-10. Optical image of the sample surface of electropolished 308L weld at 500X.

As shown in Figure 2-10, the overall morphology of the ferrite phase is interconnected thin and elongated fish bone shapes surrounded by the austenite matrix. A Hysitron triboindenter 950 was used for the load-controlled nano-indentation test in INL. The indenter used is a diamond Berkovich tip system by Bruker. All indentations were performed after routine calibration of the tip area position and loading. To avoid interference between the austenite and ferrite phases, a maximum load of 2 mN was set for the indentation with the average indentation depth at around 400 nm. The sample

surface was scanned to obtain general information about the phase size and morphology. The position of the indent was then set based on the scanned image. The indentation was divided into three stages: loading for 5 s, holding for 2 s, followed by another 5 s for unloading shown in Figure 2-11. A post-indentation image generated by the indenter tip scanning over the sample surface is shown in Figure 2-12. The red circles indicate the indent identified within austenite phase and the green circles denotes the location of the intents in the ferrite phase. An average of 45 indents were performed for each sample.

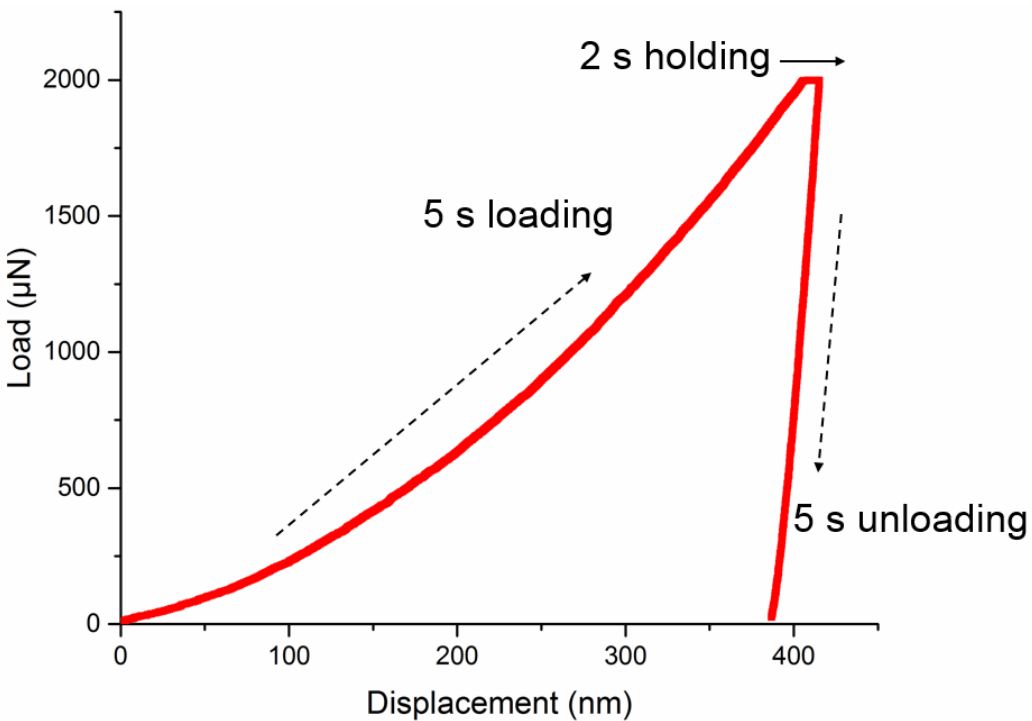


Figure 2-11. Loading and unloading curve for the nano-indentation.

To interpret the results of the indents, a direct comparison of the indent mapping and the scan image was performed to determine the number of each indent by visual recognition from their relative locations. The raw data for each indent number was

stored in a hys file and analyzed with Triboscan software to obtain parameters, such as effective indent depth, hardness and reduced elastic modulus.

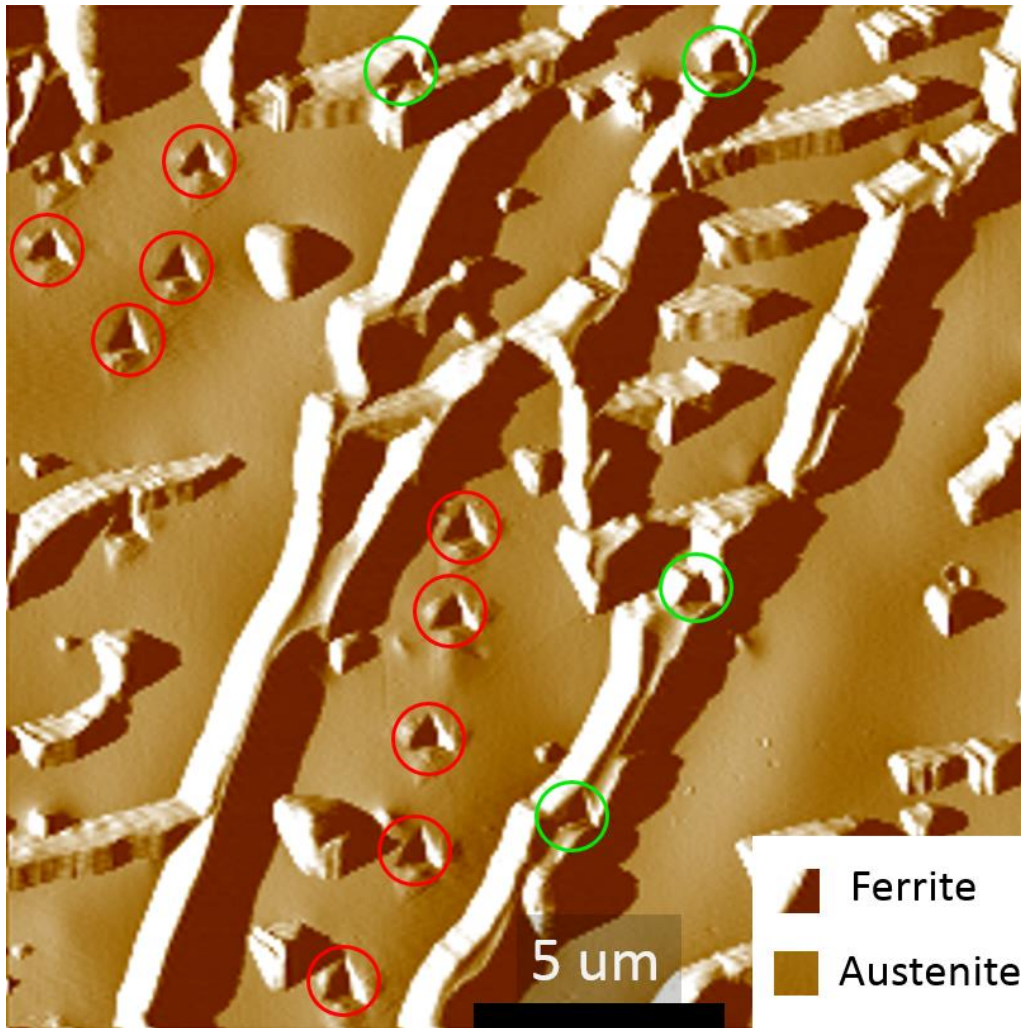


Figure 2-12. Tip scanned image of 308L weld with indentations.

For the Berkovich indenter, the hardness of the indented region can be calculated through equation Eq. 2-2.

$$H = \frac{P_{max}}{A_c} \quad (2-2)$$

where  $P_{max}$  is the maximum loading and  $A_c$  is the actual contact area. For this experiment, the indenter tip contact area as a function of indentation depth was calibrated on a piece of quartz with known hardness and elastic modulus.

### 2.5.2 Miniature Tensile Test

The effect of thermal aging on the mechanical response of CASS was evaluated by miniature tensile tests. Thermal aging was conducted at 400°C for 10,000 hrs. This thermal aging condition is known to reduce the impact energies of CASS alloys significantly, approaching their lower bounds regardless of their chemical compositions [17]. Such micro-scale uniaxial tensile tests have not been fully standardized [67,68]. The samples were miniature flat tensile specimens with a nominal gauge section of 1.6 mm x 0.76 mm x 7.6 mm, as shown in Figure 2-13. Two tests were performed at room temperature for unaged and aged CF-3. The strain rate was  $1 \times 10^{-3} \text{ s}^{-1}$ . The test results were corrected with the elastic modulus of stainless steels (210 GPa) to compensate for the compliance of loading strain. It must be pointed out that, according to the ASTM report,[68] the sample thickness should be around 4-5 times greater than the grain size. Thus, the test results in this study might not be representative of the actual polycrystalline tensile behavior. However, considering the average size of the ferrite phase at 10  $\mu\text{m}$ , the thickness is 5 times greater than ferrite phase size. Thus, the miniature-testing sample is sufficient to reveal the effect of ferrite hardening on the tensile behavior of the duplex structure. Subsequent fractography studies were performed using a Tescan LERA3 Xe plasma source FIB/SEM.



Figure 2-13. Sample dimension for the sub-size tensile test of CF-3.

### 2.5.3 Micro Scratch Test

The micro scratch test was carried out to characterize the fracture toughness property of the material. Three groups of 308L stainless steel weldment samples were prepared with the following treatment conditions: as-welded, aged for 2,226 h at 400 °C, and aged for 6,000 h at 400 °C (Table 3-1). Bulky specimens with dimensions of 10 mm x 10 mm x 2 mm were sectioned from bulk weldment fusion zone. Steel plates were further polished to make sure that the top and bottom surfaces were parallel. A 0.06 μm silica colloidal suspension was used in the final step to improve the smoothness of the testing surface. With an estimated activation energy of 164 kJ/mole for the weldment, these two aging experiments were equivalent to 17.6 years and 47.4 years' service period at 315 °C in a LWR according to Eq. 1-1. Thus, these two aging experiments were representative of two distinctive degrees of aging embrittlement. With the increase in aging time, the testing results should yield an obvious descending trend of fracture toughness.

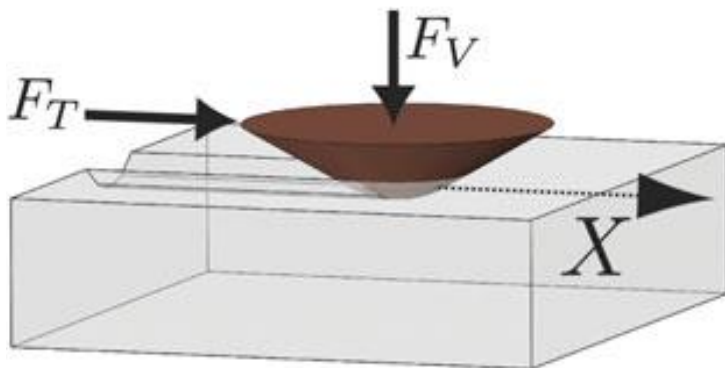


Figure 2-14. Schematic of the micro scratch test.

The basic schematics of the testing are shown in Figure 2-14. A new indenter L-119 was used for the modified micro scratch test. It is diamond indenter with a conical-spherical shape with a tip radius of 100 μm, and half apex angle of 45°. Experiments

were conducted at room temperature with progressively increased loading force using the Anton Parr Micro Combi-Tester, which has a valid loading range at 0.1 mN to 30 N with resolution at 0.1 mN. The maximum indent depth could reach 1 mm with depth measurement resolution at 0.3 nm. The loading force was applied from 0.03 N to 30 N with a loading increment rate of 1 N/s. The length of the scratch was controlled at exactly 3 mm with a scratch speed of 6 mm/min. The rate of data acquisition was set at 30 Hz. Three scratches were conducted for each condition to obtain an average penetration depth and sliding force.

All samples were sectioned into dimensions slightly greater than 15 mm x 15 mm from the fusion zone of the weldment block using a Techcut-5 high speed diamond saw manufactured by Allied High Tech. A diamond wafer blade with diameter of 6" and thickness of 0.02" was used. The feeding speed was 0.01"/min and blade rotation speed was 3000 rpm. The estimated abrasive cutting damage to the steel subsurface was very small [69,70]. Further polishing were carried on a Struers Tegramin-25 to flatten both surfaces while removing the sectioning damage layer. Samples were glued onto a steel plate holder using crystal bond. The rotation speed of the wheel was set at 150 rpm. The sample surface was finished with 1200 grit SiC sandpaper. To eliminate the grinding damage layer, further polishing with a 3  $\mu$ m diamond slurry was used. All sample preparations were performed at the University of Florida. Samples were then shipped to Anton Parr Inc. for the micro scratch test.

To accurately simulate the scratching process on the steel weld, the calibration material should have similar fracture mechanics. Therefore, ANSI-1045 steel was

chosen with a referenced fracture toughness of  $50 \text{ MPa(m)}^{1/2}$  for the indenter shape function calibration in Eq. 2-3:

$$f = 2p(d)A(d) \quad (2-3)$$

where  $f$  is the indenter shape function,  $d$  is the penetration depth,  $p(d)$  is the indenter perimeter as a function of penetration depth  $d$  and  $A(d)$  is horizontal projection area as a function of penetration depth  $d$ . Both the spherical and conical parts of the tip were gradually in contact with the steel materials due to the intermediate indentation depth.

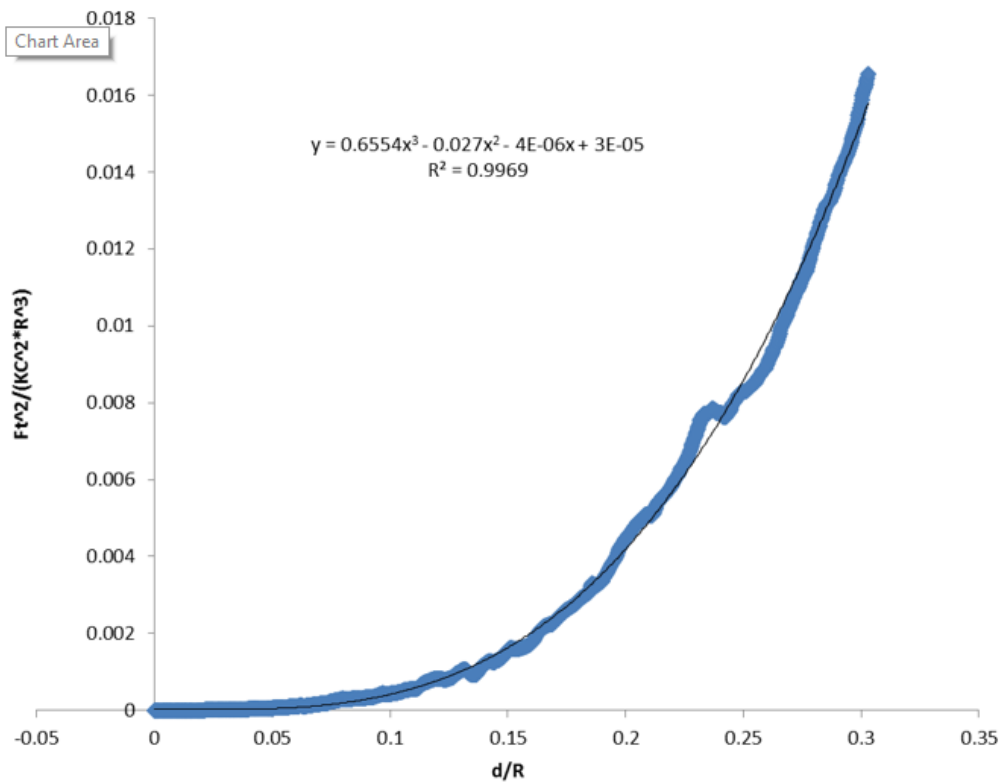


Figure 2-15. Indenter shape function calibration with fitted curve.

The ratio of penetration depth to indenter radius,  $d/R$ , was used for the calculation. The equation used for the calibration is shown in Eq. 2-4.

$$f\left(\frac{d}{R}\right) = R^3\left[\alpha\left(\frac{d}{R}\right)^3 + \delta\left(\frac{d}{R}\right)^2 + \gamma\left(\frac{d}{R}\right)\right] \quad (2-4)$$

where  $f$  is the indenter tip shape function,  $\alpha$ ,  $\delta$  and  $\gamma$  are fitting coefficients. The calibration results  $\alpha = 0.6554$ ,  $\delta = -0.0270$  and  $\gamma = 4 \times 10^{-5}$  indicate that both the

spherical and conical parts were involved in the scratching process shown in Figure 2-14. The coefficient of determination  $R^2$  was 0.9969 representing a valid fit. To verify that this fitting is accurate in predicting the fracture toughness, a validation test was performed on paraffin wax. The measured fracture toughness was around 0.169 MPa(m)<sup>1/2</sup> with a literature value of 0.15 MPa(m)<sup>1/2</sup> extracted from three point bending test. With the error less than 13%, the calibration is quite acceptable.

The assessment of the aging response of 308L weld was conducted by fractographic analysis using SEM. For the scratch surface analysis, the corresponding SEM images focusing on the rim of the scratches for each condition is shown in Figure 2-13. Overall, the micro scratch test on fracture toughness was recently developed by Akono [71,72]. The post scratch surface analysis for potential embrittlement interpretation was not yet fully established. In comparison, fractographic analysis in other fracture testing methods, such as the tensile test, has validated crack surface analysis with the failure mode justification.

To symmetrically conduct the analysis without skewed conclusion, conservative features were used with only qualitative comparisons introduced. The cracks initiated at the bottom of the scratch groove were ignored for the aged sample due to the low density. The front and ending region of the scratch were not selected either. Cracks developed in these two areas could be either too localized or too trivial to be detected by SEM. In fact, for each condition, 3 scratches were made within nearby region distanced by at least 5 mm. For each scratch, exactly the same testing parameters, such as loading increase rate and horizontal sliding speed, were applied. All three scratches were examined by SEM for each condition, and showed good consistency

among scratches. Here only one scratch was selected randomly with results at 0° tilting presented. Equipment used for the examination was a Tescan LERA3 Xe plasma source FIB/SEM.

## CHAPTER 3 RESULTS

### 3.1 Metallography and Chemical Composition

#### 3.1.1 CF-3

The unaged and aged CF-3 metallography is shown in Figure 3-1. The darker region is the ferrite phase while the lighter area is the austenite phase. As explained in paragraph 1.3.1, the  $\mu\text{m}$ -scale ferrite phase resides at the core of the elongated austenite dendrite arms [73,74]. The ferrite morphology within the duplex structure can be observed as a discontinuous fish bone shape. Combined with the FEM modeling and experimental results by Schwarm and Wang [26,28], the duplex structure rather than the austenite dendrite structure should be the focus of the structure-property relationship for such casting.

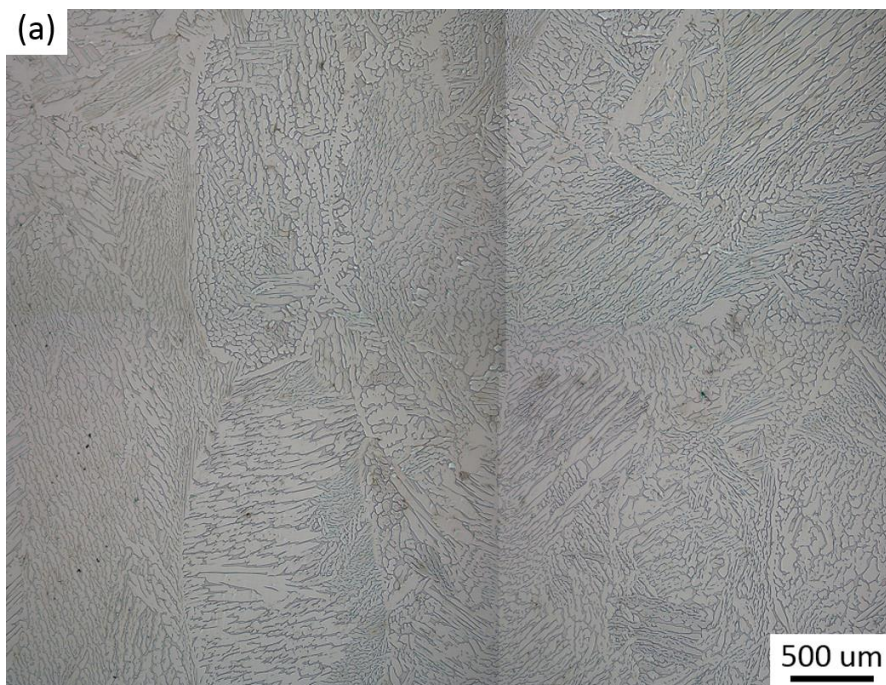


Figure 3-1. Metallographic image of CF-3 of a). unaged and b). aged for 10 kh (50X).

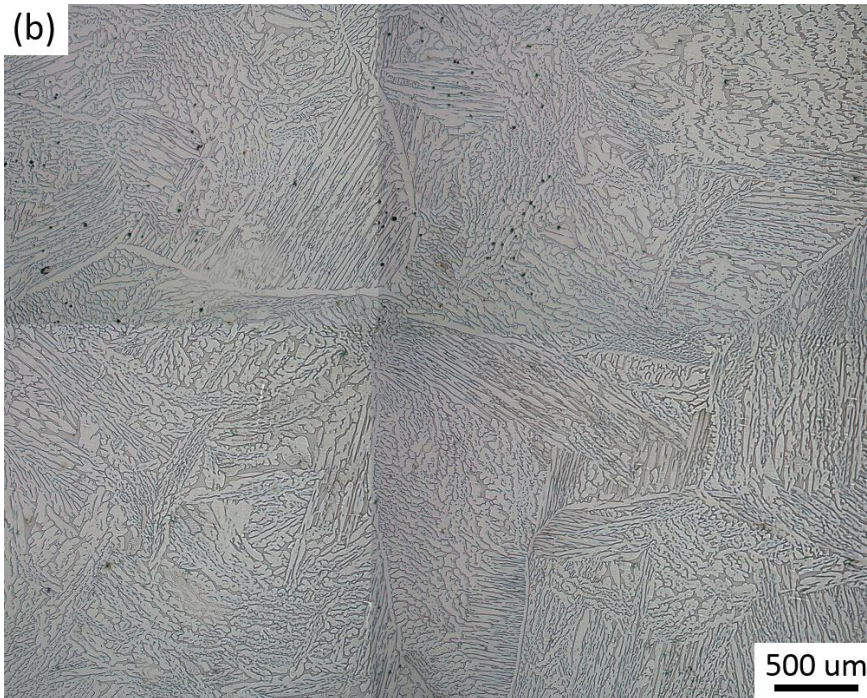


Figure 3-1. Continued.

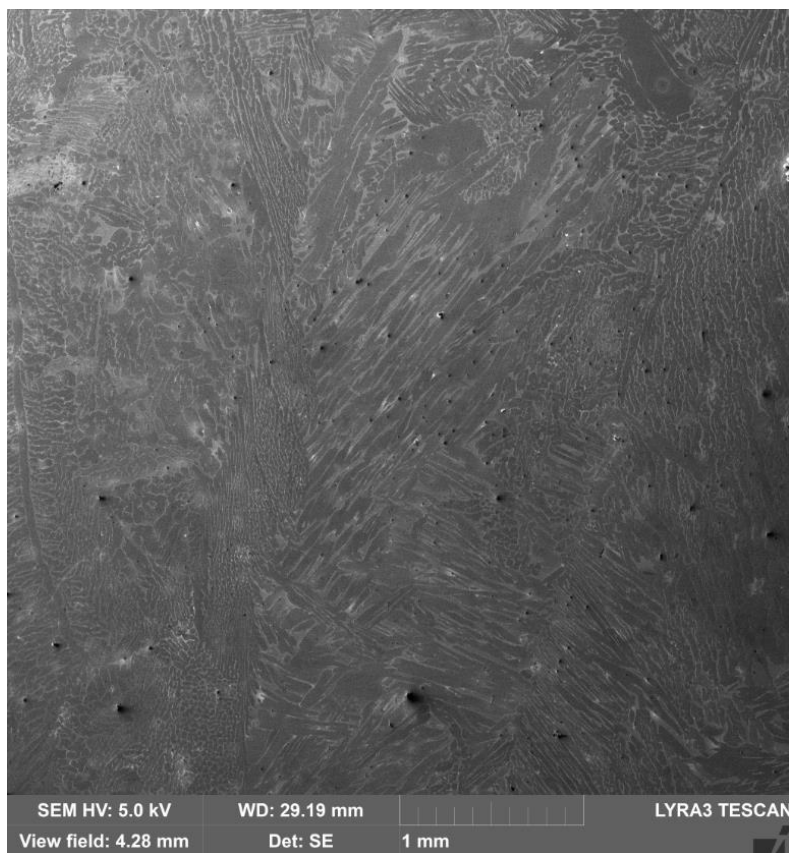


Figure 3-2. Metallographic image of unaged CF-3 using SEM.

Table 3-1 lists the APT measured chemical composition of the ferrite tips at four different conditions of CF-3. The standard deviations were calculated for all four conditions. The concentrations of Fe, Cr, Ni, Mn and Si are reasonably consistent. Even for P, S and C with very low concentrations, the measured values do not vary significantly, considering a relatively large measurement error for these minor alloying elements.

Table 3-1. APT measured chemical composition (wt.%) of the ferrite at different conditions.

Condition	Ni	Si	P	S	Mn	C	Cr	Mo	Fe
As cast	5.61	1.36	0.028	0.0009	0.57	0.006	24.45	0.618	67.34
Aged	5.71	1.37	0.026	0.0015	0.56	0.011	23.61	0.658	68.05
Irradiated	5.30	1.39	0.042	0.0012	0.54	0.009	24.11	0.657	67.95
Aged & Irradiated	5.87	1.25	0.028	0.0015	0.55	0.013	23.06	0.664	68.19
Standard deviation	0.05	0.01	0.001	0.0003	0.002	0.0006	0.13	0.005	0.08
As cast (EDS)	6.2	1.9	-	-	1.33	-	24.06	0.31	66.19

In comparison, the EDS point scan was performed on the ferrite phase of different grains of the unaged CF-3 specimen shown in Figure 3-2. Due to the limitation of detection resolution, only major elements are included in the last row of Table 3-1. Overall, no significant difference in chemical composition is observed for the tested ferrite with respect to Fe, Cr and Ni compared with APT results. This indicates that the content of Fe and Cr in these specimens are relatively similar. A much greater content of Si and Mo is observed in the EDS measurement. This can be due to the large error in the measurement.

### 3.1.2 308L weld

The metallography of the as-welded and 2226 h aged 308L weldment is shown in Figure 3-3 by optical microscopy. The darker region is the ferrite phase while the lighter

area is the austenite phase. Figure 3-4 shows the corresponding metallography using SEM. Samples were obtained from the fusion zone near the welding centerline. The morphology of equiaxed dendritic structure can be observed for both as-welded and aged samples, as reported by Silva [75–77] and David [78]. The key objective of this study is to examine how the ferrite phase decomposition affects the mechanical properties of the weldment, for instance, the fracture toughness. Thus, the base metal, heat affected zone and columnar dendrite area are not the focus of this study. Manganese silicide inclusion is observed in both ferrite and austenite phases, similar to those found in Alexander’s report [79].

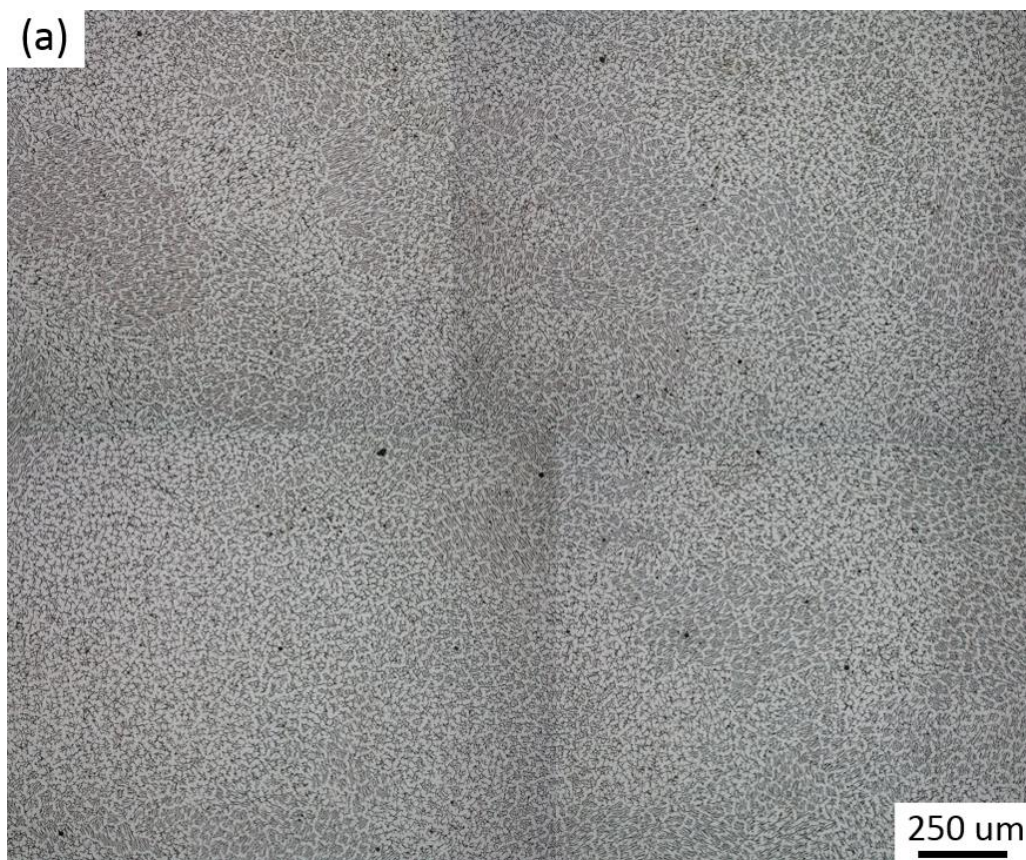


Figure 3-3. Metallographic image of 308L weld a). as-welded and b). aged for 2226 h (50X).

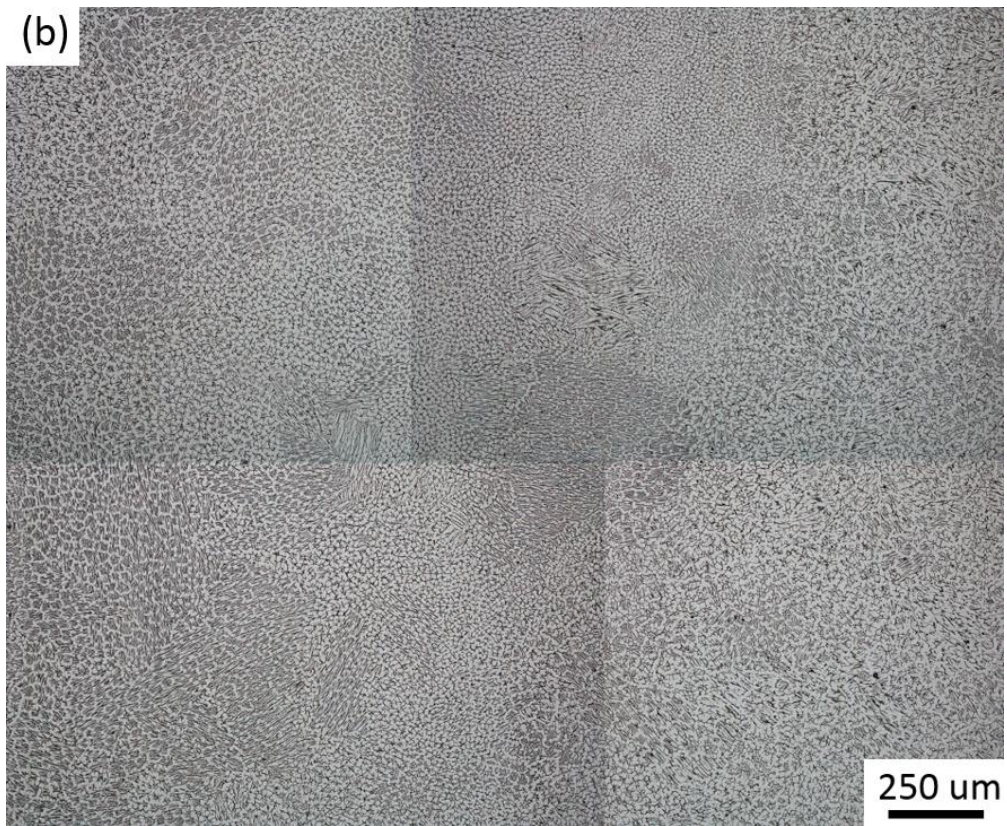


Figure 3-3. Continued.

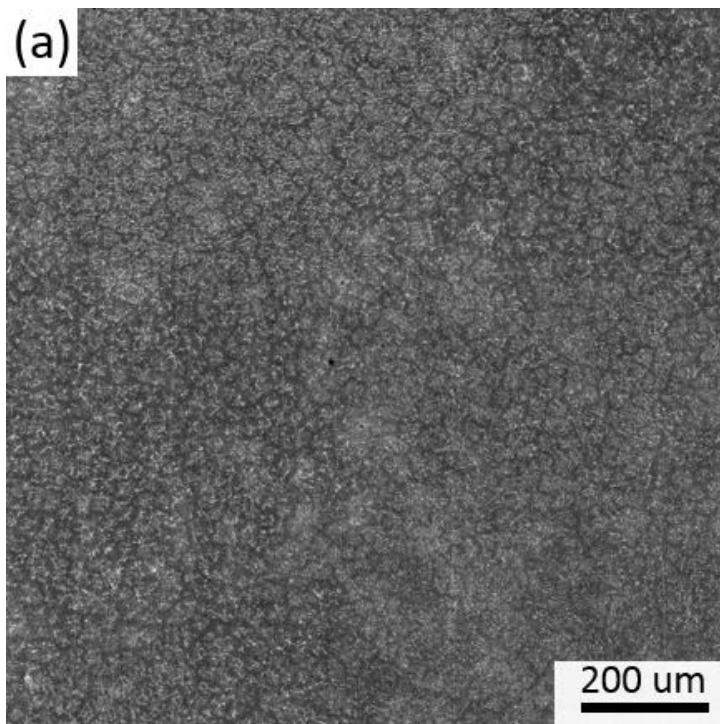


Figure 3-4. Metallographic image of 308L weld a). as-welded and b). aged using SEM.

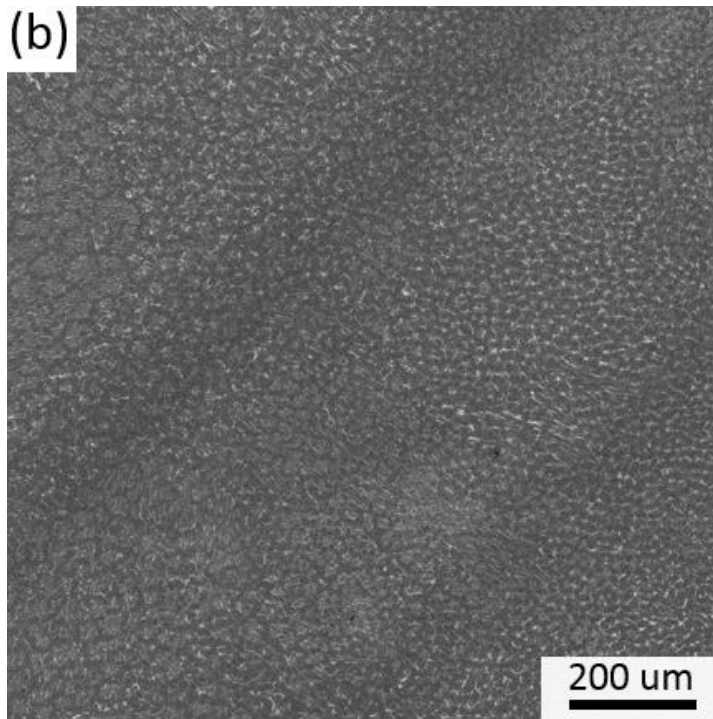


Figure 3-4. Continued.

### **3.2 Crystallography and Microstructure Characterization**

The environmental degradations on ferrite in CF-3 steels and 308L welds were revealed through spinodal decomposition and G phase precipitation. The crystallography of the ferrite and austenite phases is not the focus of this study. However, it is the basis of the nano-feature characterization of spinodal decomposition and G phase precipitation. Thus, only the TEM diffraction patterns to with precipitation are shown in this section. The TEM results are further compared with the APT reconstruction of ferrite phase for better structural characterization.

#### **3.2.1 Spinodal Decomposition**

Figure 3-5 shows the evolution of Cr distribution in the as-cast, end-of-life aged and end-of-life aged with irradiation ferrite phase in CF-3 cast steel. The atomic maps were formulated from a slice of 10 nm in thickness at the Y-middle plane of each APT

tip reconstruction. The atom maps illustrate that Cr clustering was induced during thermal aging at 400 °C. The extent of clustering was further enhanced by subsequent neutron irradiation.

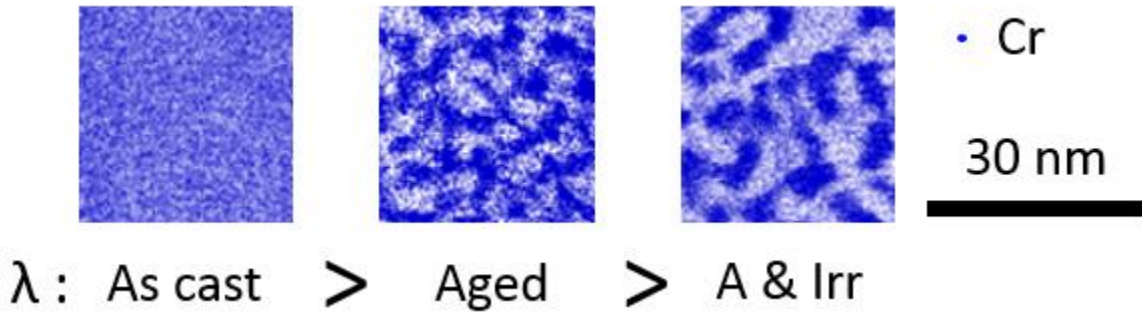


Figure 3-5. Cr distribution in ferrites upon different treatment conditions of CF-3.

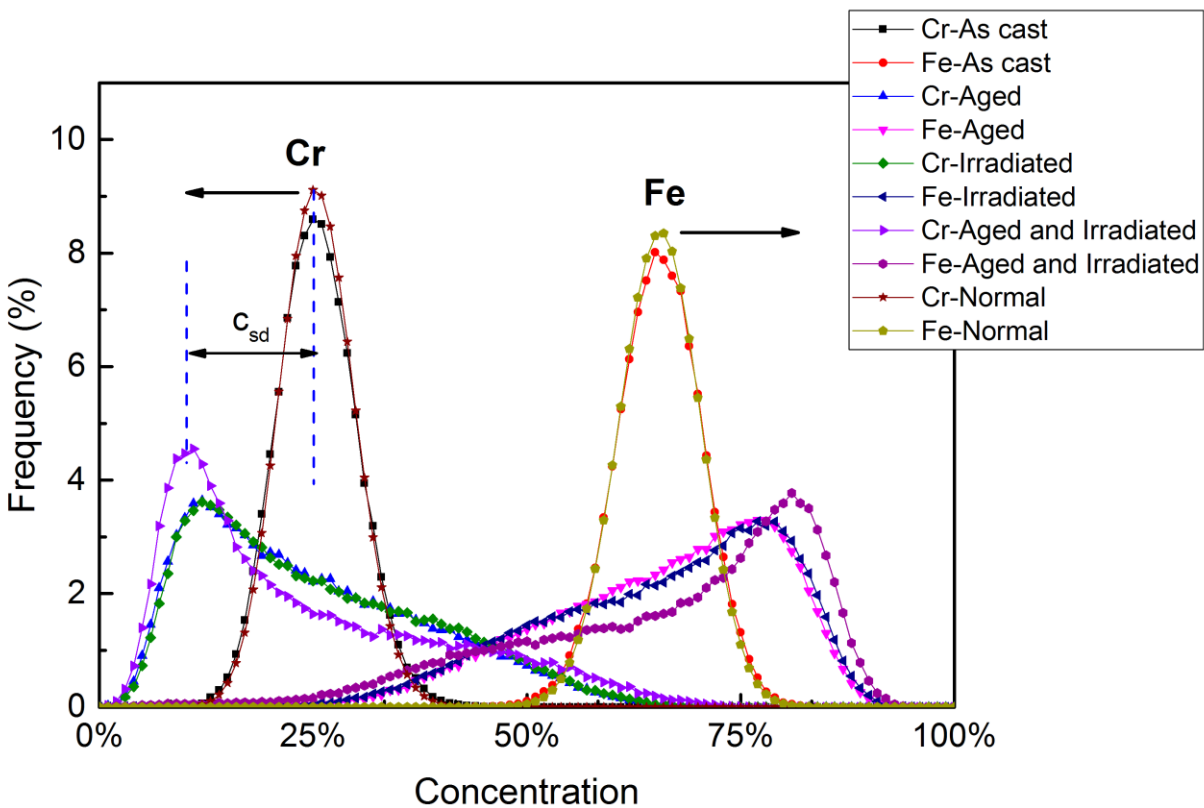


Figure 3-6. Fe-Cr elemental frequency distributions in ferrites for different conditions.

To quantify spinodal decomposition, the Cr and Fe frequency distributions are plotted using the frequency distribution analysis illustrated in 2.3.1, as shown in Figure

3-6. The atoms in solute clusters were excluded from the analysis, and the bin size of ions was 100. For comparison, theoretical normal distributions of Cr and Fe were also calculated based on the measured average concentrations in the examined APT specimens. Apparently, the as-cast ferrite has nearly perfect normal distributions of Cr and Fe with profile peaks located at 25.24 and 65.88 at.%, respectively. This is consistent with the Cr atom map, showing that there is no spinodal decomposition occurring in the as-cast ferrite. For the aged and irradiated samples, both of the Cr frequency profile peaks shift to left, while the profile is also broadening into the high concentration range. To quantify the extent of spinodal decomposition, the measured values of  $C_{sd}$  as illustrated on Figure 3-6 are 0, 13.37, 13.37 and 14.97 at.% for conditions of as-cast, aged, irradiated, and aged plus irradiated, respectively. For the Fe atoms, the concentration frequency profiles show a similar trend by deviating from a nominal distribution upon thermal aging, irradiation or a combination of those two. The low-dose irradiation on thermally aged ferrite could promote further spinodal decomposition and lead to a higher extent of demixing of Cr and Fe atoms in the ferrite.

To systematically analyze the spinodal decomposition in ferrite under high dose neutron irradiation, the frequency distributions of Fe and Cr were calculated and are shown in Figure 3-7. The bin size was set at 100 ions to best reveal the distribution trend. Peak broadening and shift of Cr and Fe distribution due to neutron irradiation was observed compared with the binomial distribution. Such a phenomenon can be interpreted as a result of the demixing behavior of Fe and Cr element from the homogeneous state.

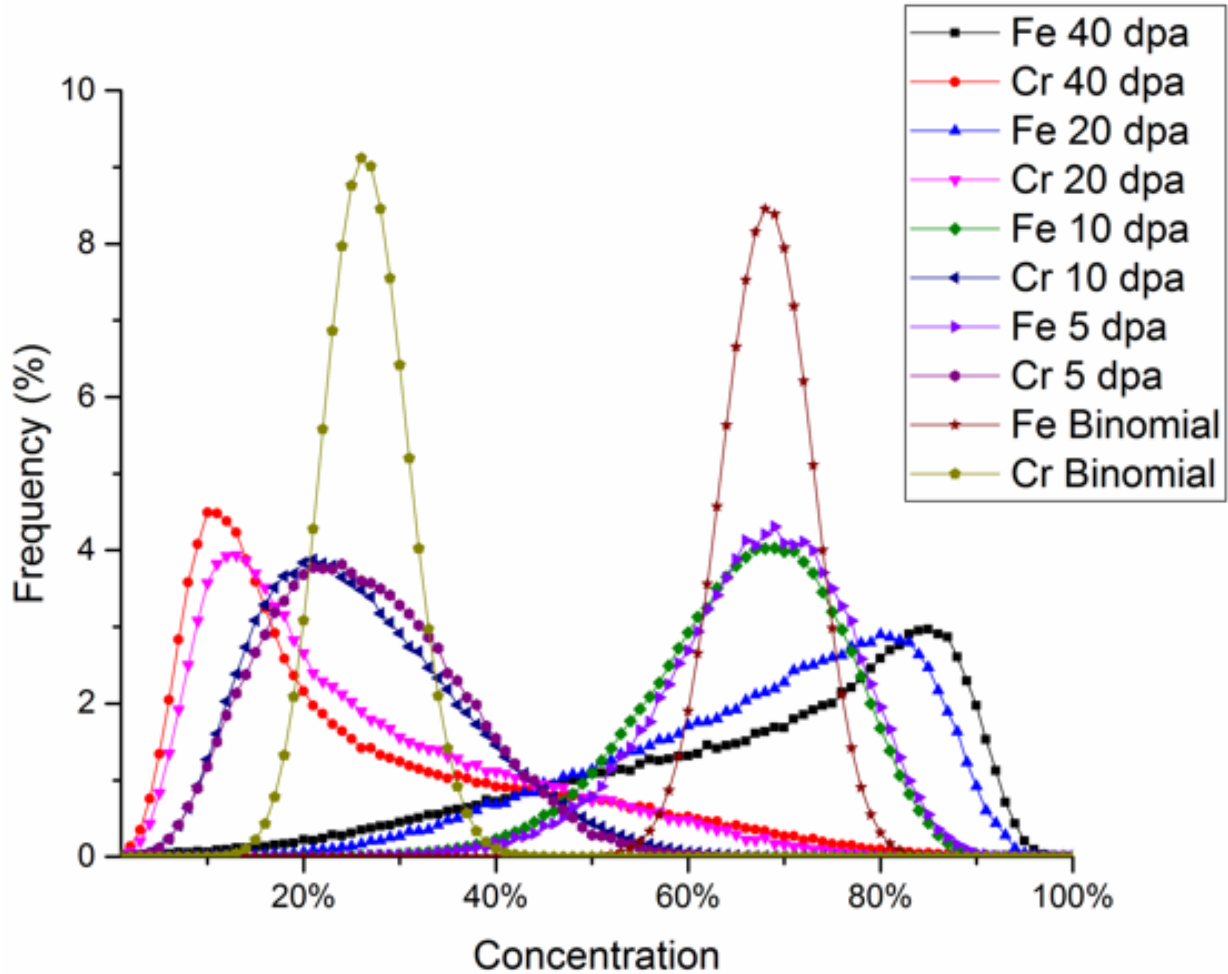


Figure 3-7. Frequency distribution of Fe and Cr in ferrite of irradiated CF-3.

RDF was applied to the Cr element distribution to extract the wavelength  $\lambda$  of the modulation. The dependence of  $\lambda$  on neutron irradiation dose is illustrated in Figure 3-8. The wavelength of as-cast CF-3 at 0 dpa is also added to the curve as a comparison. An overview of the Cr atom spatial distribution for all four irradiation conditions is also illustrated. A chip of 10 nm was extracted from the cone shape tip for each condition to generate the Cr map. The blue color represents the Cr atoms. A scaling morphology of the Cr atom distribution can be observed in all four irradiation conditions, indicating spinodal decomposition. The darker blue region is the Cr-rich  $\alpha'$  phase. The contrast of

the dark and white regions grows stronger with increasing irradiation dose. A size increase of the dark domain (Cr rich) and white domain (Cr diluted) was observed with increasing irradiation dose, while the white domain outgrew the dark domain at 40 dpa. Both the Cr map and the wavelength calculated from RDF indicate an increasing trend of Cr clustering compared with as-cast ferrite. A possible wavelength saturation trend was observed near 20 dpa with an estimated wavelength of 20.3 nm.

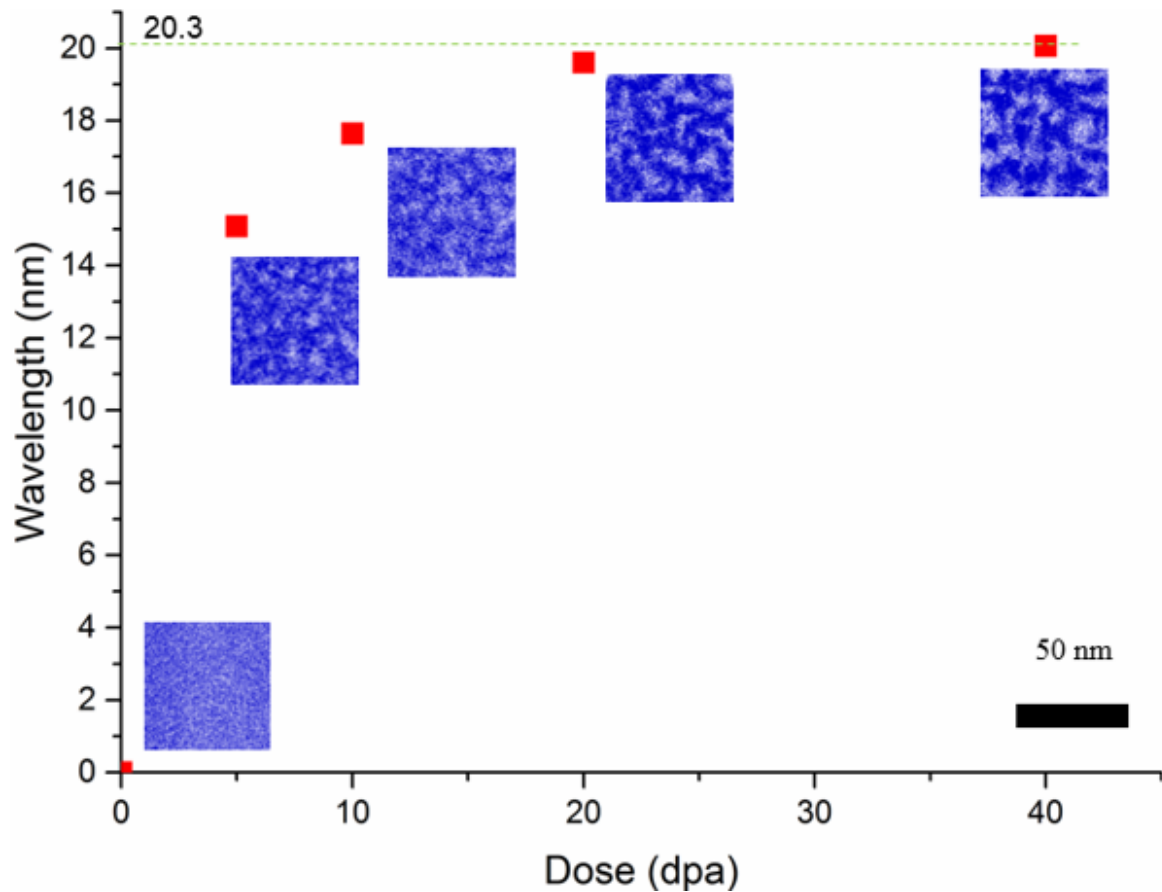


Figure 3-8. Wavelength vs irradiation dose of neutron irradiated CF-3.

To validate the capability and accuracy of APT in Cr clustering detection, TEM results of 308L aged at 400 °C and irradiated at 0.08 dpa were selected as shown in Figure 3-9. In comparison, the corresponding APT reconstruction under same magnification of the Cr map in black dots are illustrated in the lower left corner in Figure

3-9. The thickness of the Cr map envelope was set to be 50 nm, which is close to the actual thickness of the TEM lamellae. The two bright field TEM images were taken at zone axis [001]. In both cases, the APT reconstruction maps show a good resemblance with the TEM mottled phases. Both are direct indications of the spinodal decomposition pattern of the ferrite phase. It can be pointed out that the TEM contrast is not necessarily an exact match to APT reconstruction. The major reason for it is that the orientation of the Cr map in APT reconstruction is not necessarily aligned along the [001] direction. No correlation has been successfully established for the interpretation of the APT and TEM results.

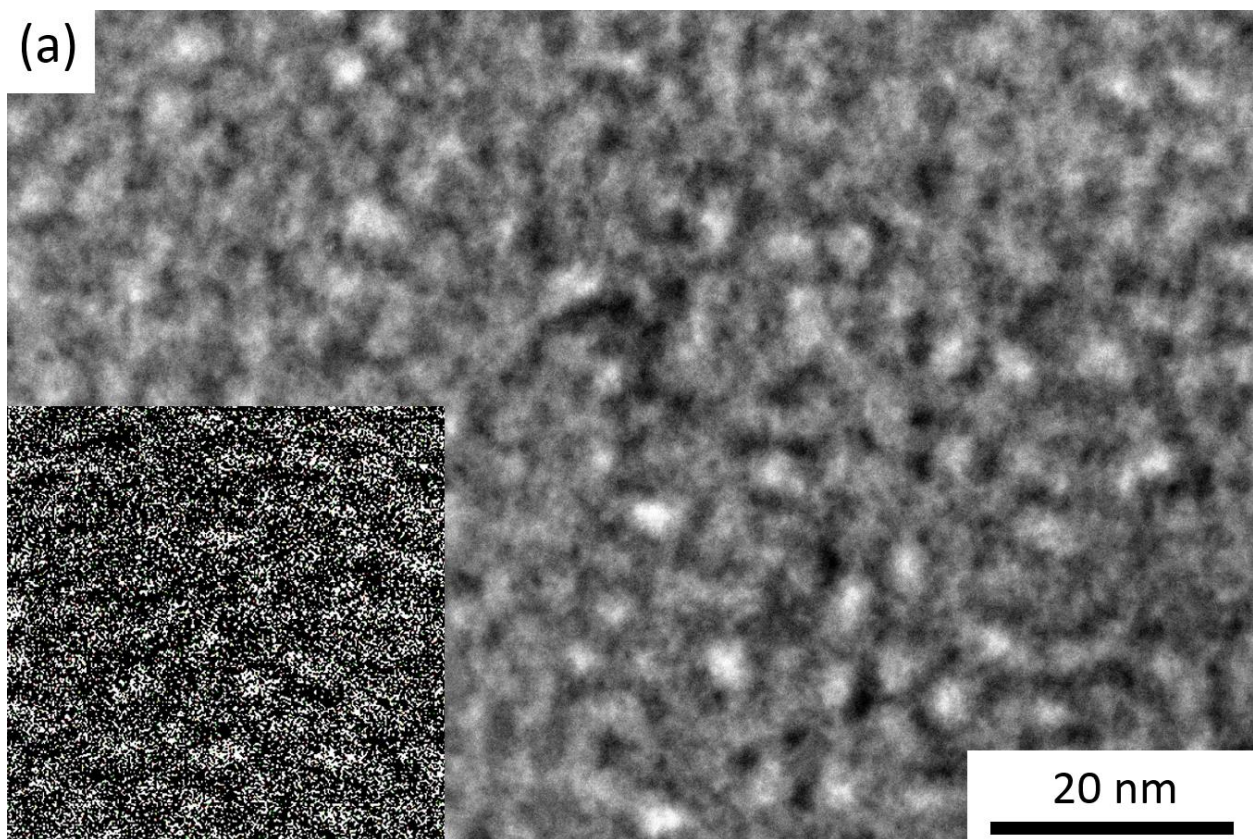


Figure 3-9. TEM images of spinodal decomposition with mottled structure in ferrite of 308L weld, a) 400 C aged for 2226 h; b) irradiated at 0.08 dpa. The small figure in the lower left corner is the APT reconstruction image.

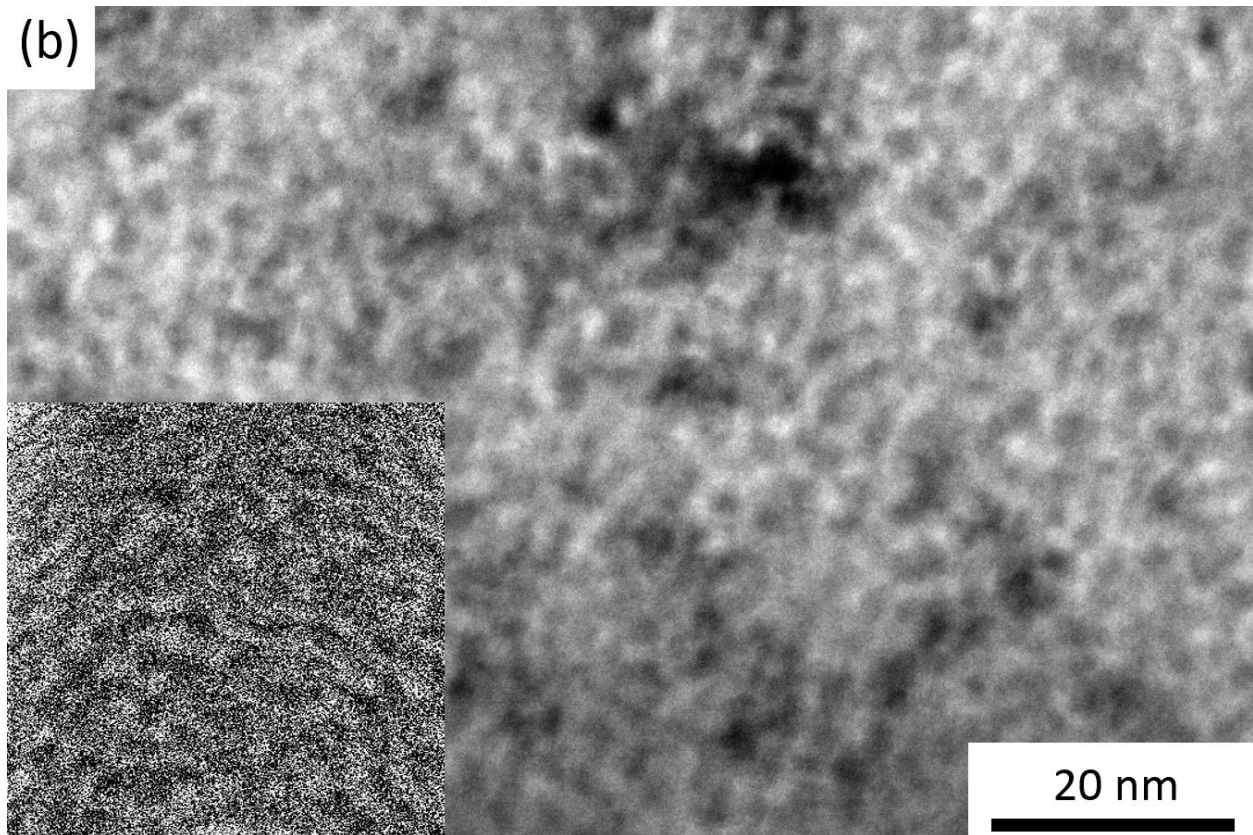


Figure 3-9. Continued.

### 3.2.2 G Phase Precipitate

Overall, the precipitates are enriched in Ni, Mn and Si for those ferrites in CF-3 and 308L weld under varied aging and low dose irradiation conditions. Such enrichment is a representative elemental composition of a G-phase precipitate. The sizes were all less than 20 nm, with a spherical shape. Figure 3-10 shows a typical reconstruction of G phase clusters via an iso-surface of the solute elements for the aged, irradiated and aged & irradiated ferrite in CF-3. Enhancement by neutron irradiation of G phase clustering in both size and density was revealed by cluster analysis quantification method.

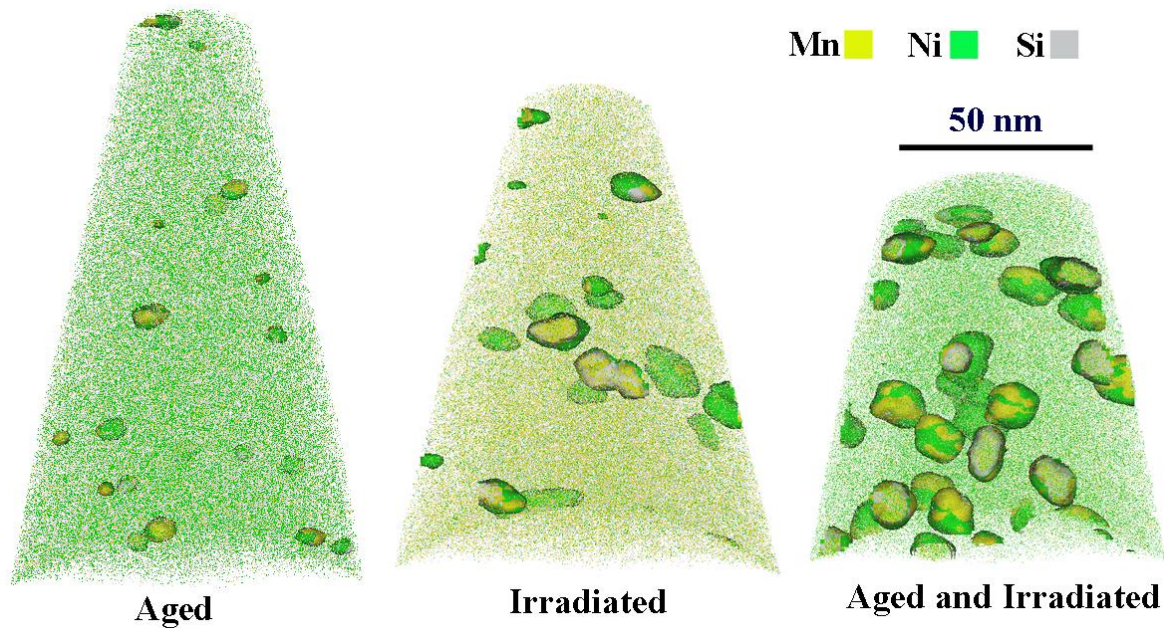


Figure 3-10. G-phase precipitates in aged, irradiated, and aged-irradiated ferrites. The images are sized to have an identical scale, and the isovalue thresholds of Mn, Ni and Si are 2, 10 and 6 %, respectively.

Table 3-2. Average composition of G phase precipitate in CF-3 (at.%)

Condition	Mo	Mn	Ni	Fe	Cr	Si
Aged	0.67	3.09	13.72	51.30	24.50	6.22
Irradiated	1.55	5.60	26.62	31.76	19.11	11.35
Aged and Irradiated	1.33	7.98	30.10	29.65	15.75	13.42

The G phase precipitation of high dose irradiated CF-3 steels is evident in Figure 3-11 and Figure 3-12. Neutron irradiation has a strong impact on the G phase size increase. On the other hand, the G phase number density keeps decreasing. The compositions of major solute elements are listed in Figure 3-8. The ratio of Ni : Si : Mn is estimated to be 15:5:2 in all four conditions. Pronounced Ni enrichment was found in the G phase clusters with an increase in concentration from 36.67% to 53.51% for irradiation doses of 5 dpa and 40 dpa, respectively. The average Ni composition in ferrite matrix is less than 6% as shown in Table 3-1.

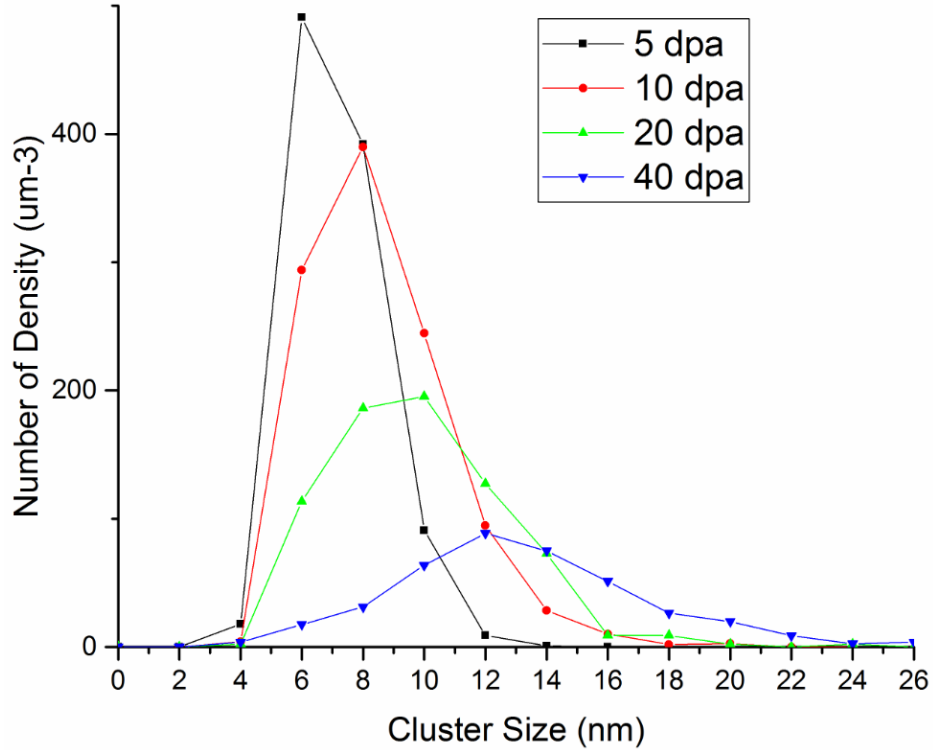


Figure 3-11. Cluster size distribution of neutron irradiated CF-3.

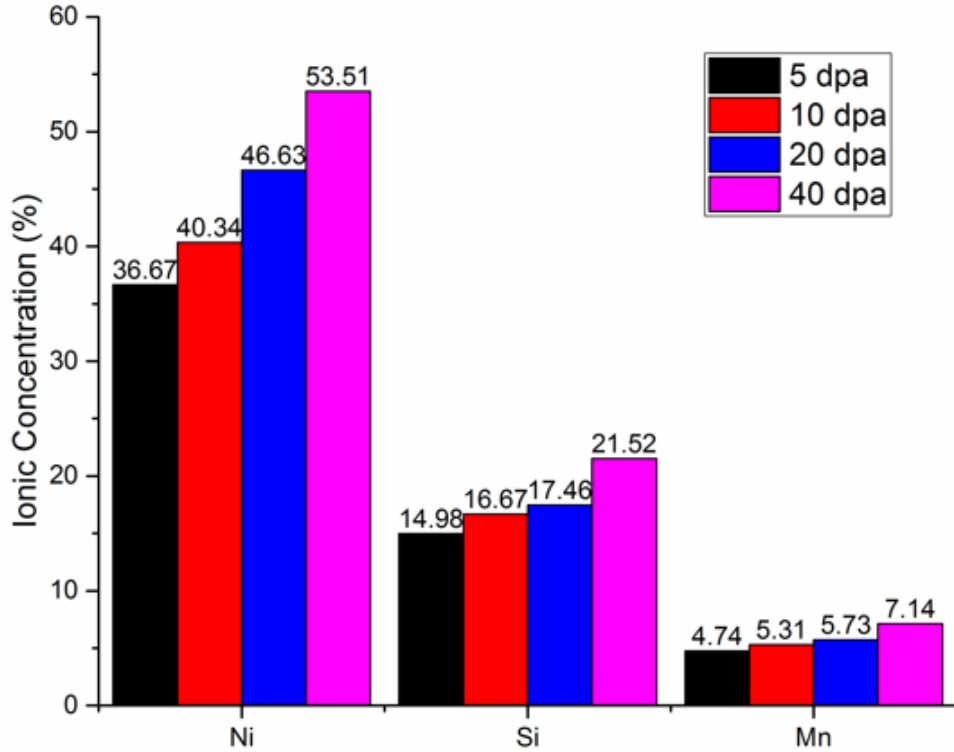


Figure 3-12. The ionic concentration of Ni, Si and Mn in G phase precipitate in ferrite of irradiated CF-3.

A summary of the G phase clusters of ferrite in CF-3 steels and 308L welds is presented in Table 3-3. The G phase precipitation behavior in the ferrite phase of 308L welds is relatively more active than that in the CF-3 steel's ferrite with respect to size and density for both aging condition and neutron irradiation conditions.

Table 3-3. Summary of G phase precipitation.

Material	Size /nm	Density ( $10^{12}/\text{cc}$ )
As-cast CF-3	0	0
10,000 h aged CF-3	2.7	7
0.08 dpa CF-3	4.0	10
A&I CF-3	4.6	11.5
As-weld weld	0	0
2,226 h aged weld	2.8	69
0.08 dpa weld	3.1	45

With the help of TEM, the crystallography of the G phase and its orientation relationship with ferrite was investigated. The goal of this study was intended to cover all the samples examined in APT. Only the result for 20 dpa irradiated CF-3 is presented. Data for the remaining conditions will be obtained in the future. As shown in Figure 3-13, the diffraction pattern of ferrite of 20 dpa-irradiated CF-3 exhibits a B.C.C. structure with strong reflections. The lattice parameter measured from Figure 3-13 is 2.85 Å which is within the range of literature reports [1]. Meanwhile a weaker F.C.C. diffraction reflection is also observed in Figure 3-14, with a lattice parameter measured of 11.60 Å, which matches previous results on G phase precipitation [39]. The lattice parameter of G phase is about 4 times the size of the ferrite matrix in this study. Such a relationship corresponds quite well with literature reports [39]. In addition, the cube-on-cube orientation of the G phase and ferrite matrix was well confirmed in this study. As shown, the zone axis direction for both G phase and ferrite matrix was at [001], indicating the direction parallelism. Furthermore, the lattice plane of (020) for G phase is

aligns with that of ferrite phase (020). Such evidence strongly indicates that the lattice planes (020) for G phase and ferrite are aligned.

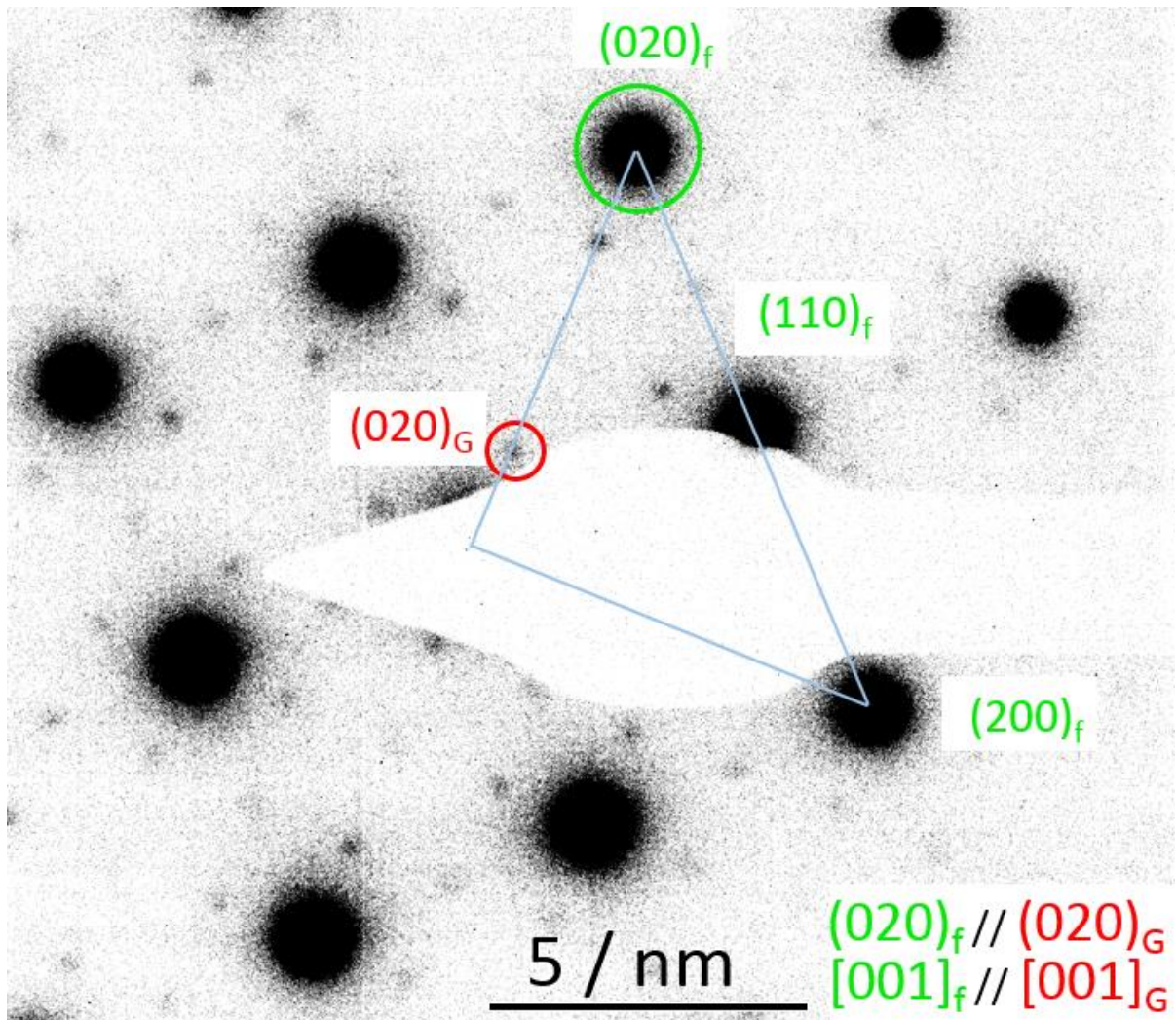


Figure 3-13. Diffraction pattern of ferrite matrix and G phase precipitate of CF-3 irradiated at 20 dpa.

Due to the weak reflection of G phase spot, it is not easy to capture its diffraction near the direct beam. Thus, the diffraction spot of G phase at  $(0\bar{2}0)_G$  shown in Figure 3-14 was used around the  $(0\bar{2}0)_f$  spot at  $g_{0\bar{2}0}$  with zone axis at  $[001]$ . The dark field image captured the tiny particle and its homogeneous distribution within the ferrite matrix. The estimated size of the G phase precipitate is about 3.5 nm.

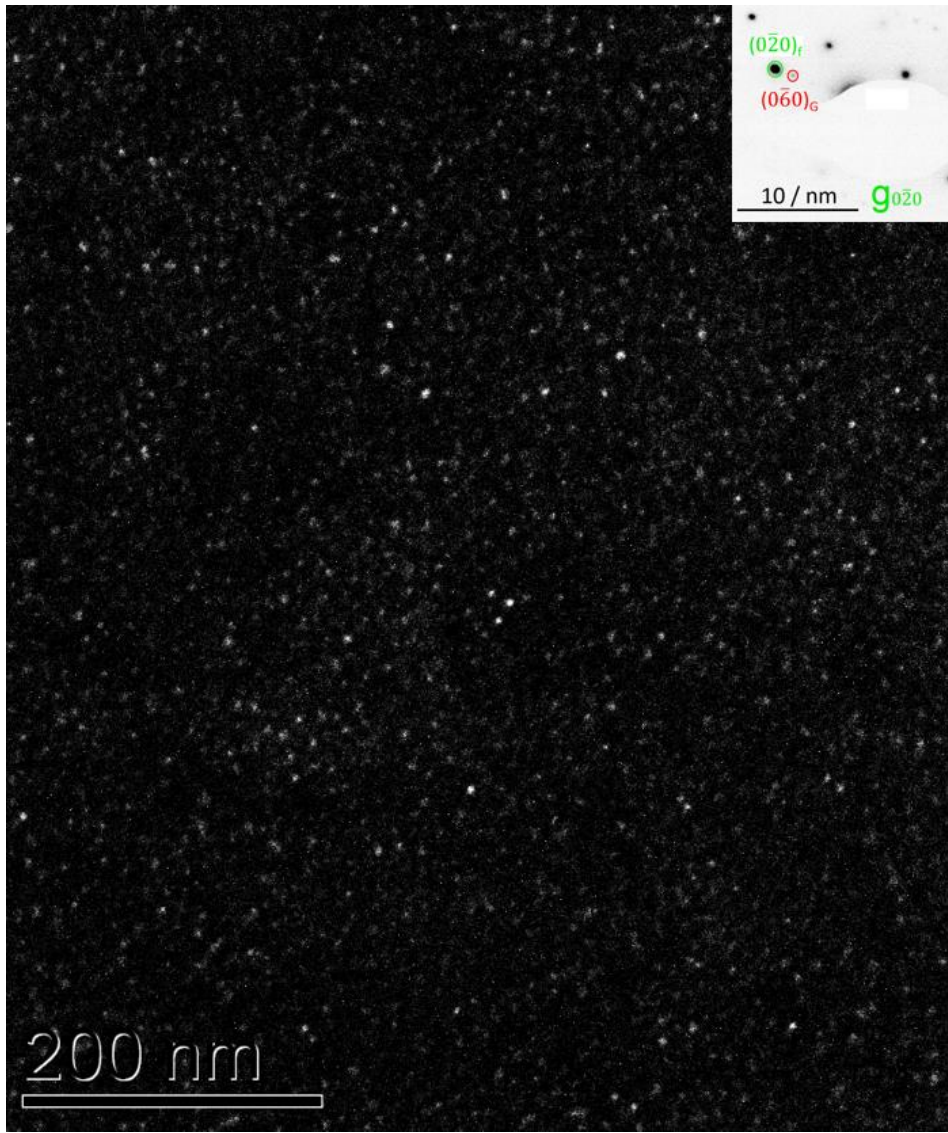


Figure 3-14. TEM image of G phase precipitate in ferrite of CF-3 irradiated at 20 dpa.

### 3.3 Mechanical Testing Results

#### 3.3.1 Nano-indentation Results on Welds

On average, the hardness of austenite for as-welded and aged 308L is 3.49 GPa and 3.53 GPa, respectively, which represents an insignificant change in the hardness data shown in Figure 3-15. This result matches well with the reported data [80].

Austenite stays quite stable under the influence of thermal aging in an intermediate temperature range. As can be seen in Figure 2-12, the edge of the indent is very close

to the ferrite/austenite phase boundary. Thus, it is impossible to rule out the influence of the nearby austenite on the nano-hardness measurement. In this case, the results were interpreted as the nano-hardness of the ferrite+austenite phase. A significant increase in hardness was observed for the ferrite+austenite phase shown in Figure 3-15 (4.49 GPa for as-welded and 6.88 GPa for aged). As can be seen, the ferrite hardening is the major reason for the increase of the deformation resistance of the ferrite+austenite phase.

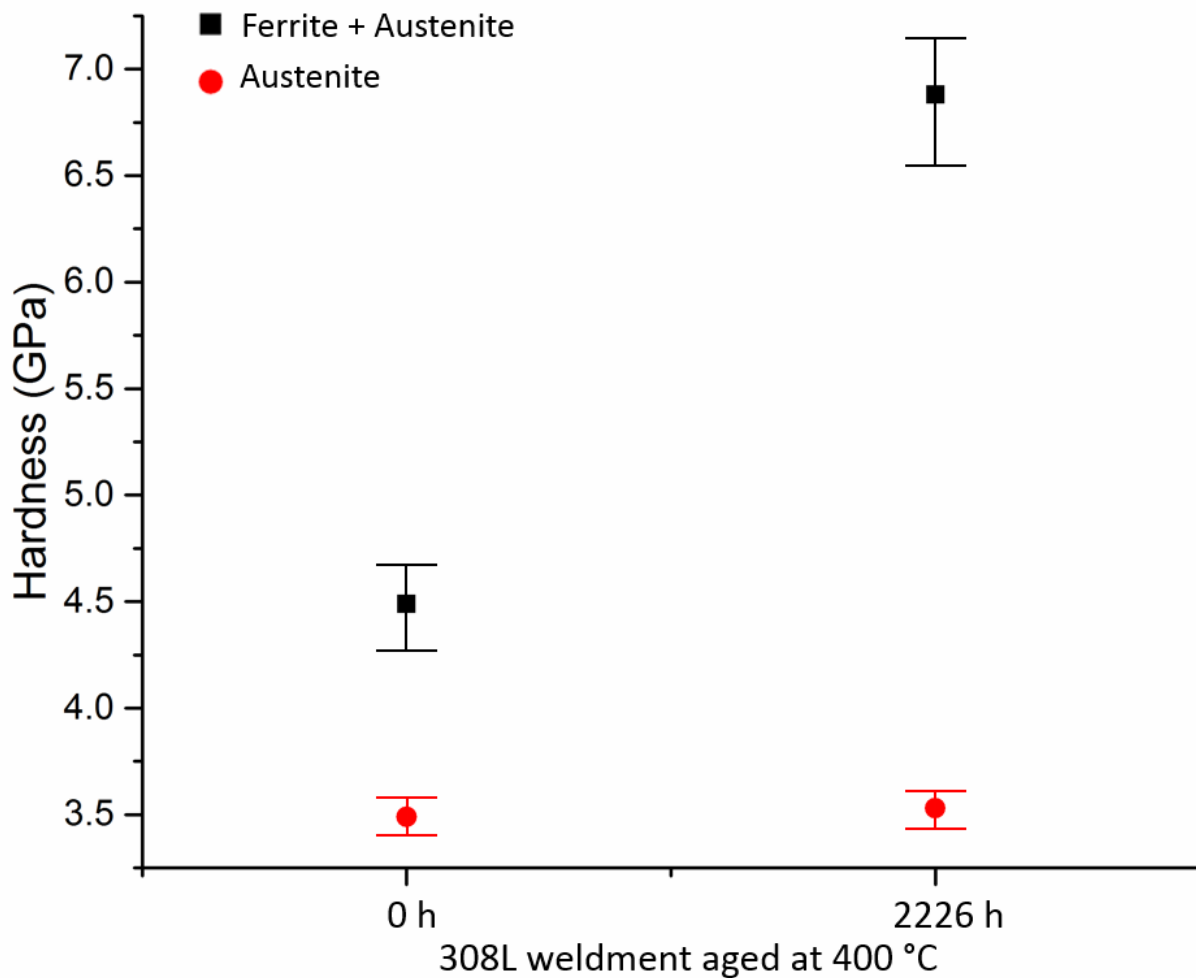


Figure 3-15. Nano-hardness of the austenite and ferrite + austenite phase of 308L weld aged at 0 h and 2226 h.

### 3.3.2 Tensile Test on CF-3

The tensile test results of as cast and aged CF-3 are presented in the inset table of Figure 3-16. The effect of thermal aging increased yield strength (YS) by 39 MPa and ultimate tensile strength (UTS) by 128 MPa approximately for CF-3 steel. Shown in Figure 3-16, a 20% increase in YS is present in the strain range from 0 to 0.02. This phenomenon may be due to the age induced dislocation pinning in both ferrite and austenite [81]. Right after the elastic deformation, strain hardening was initiated for both conditions with strain at 0.02-0.05. A reduction in ductility, with 24% decrease in uniform elongation (UE), is another indicator of the ferrite hardening effect. The austenite matrix is responsible for the major part of the plastic deformation. The SEM image of the tensile fracture surface is illustrated in Figure 3-17. SEM images were taken at 5 kV with absorbed current around 9 pA. The working distance was at 30 mm with only the secondary electron detector used for imaging. The size of the probe was 15 nm. Ductile dimple fracture was observed in both unaged and aged CF-3 specimens.

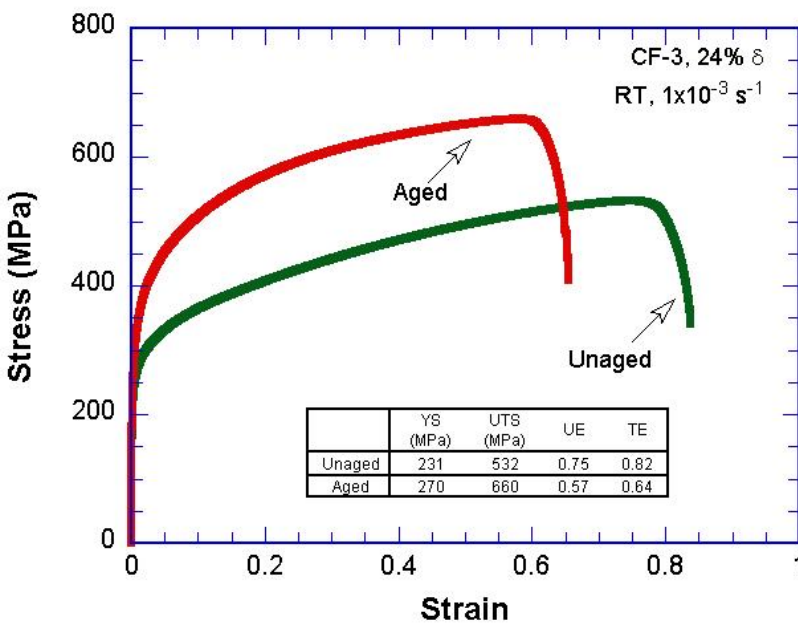


Figure 3-16. Stress strain curves of CF-3 with 24% ferrite tested at room temperature.

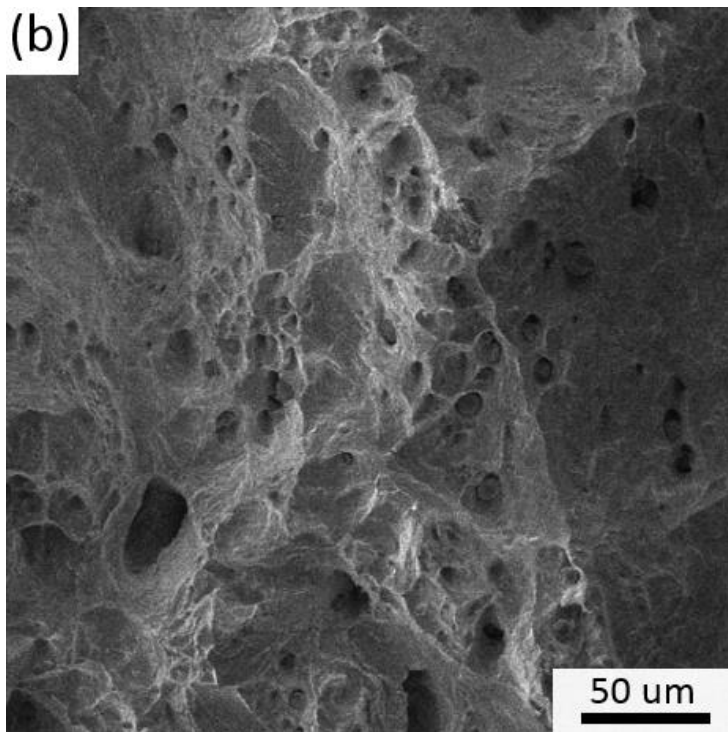
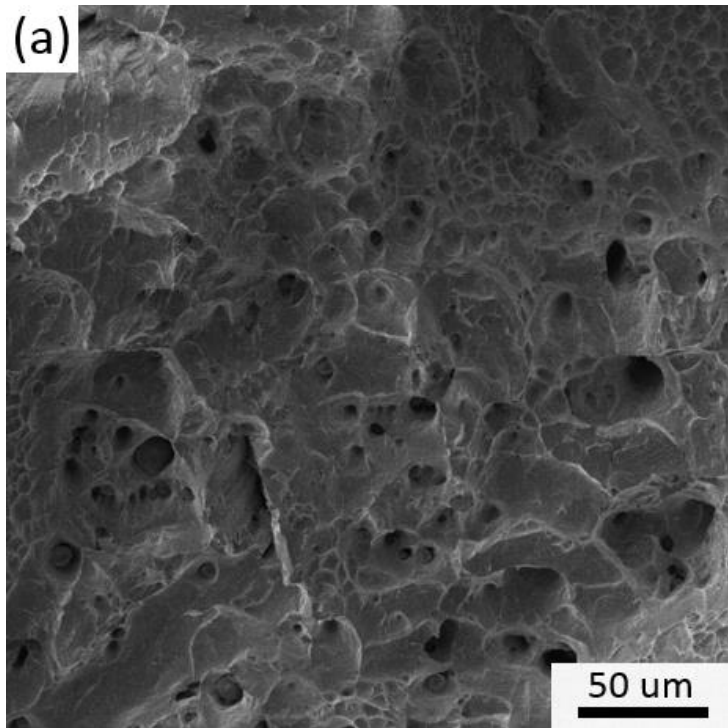


Figure 3-17. SEM fractography of CF-3 with 24% ferrite in a). unaged and b). aged condition.

### 3.3.3 Micro Scratch Test on Welds

Fracture toughness results for the 308L welds under various aging conditions measured using the micro scratch test are shown in Table 3-4. The as-welded condition has the highest value of  $22.65 \text{ MPa(m)}^{1/2}$  while the 6,000 h aging condition has the lowest fracture toughness at  $17.71 \text{ MPa(m)}^{1/2}$ . In comparison, the  $J_{IC}$  values tested by 0.4T-CT test on as-welded 308L cladding was estimated at  $200 \text{ kJ/m}^2$  at room temperature [82]. This value is quite typical for extremely tough material in steel welding. If the elastic modulus of 308L is assumed to be 150 GPa (estimated based on previous nano-indentation in this study) and Poisson's ratio at 0.3, the 308L weld plane strain fracture toughness could be as high as  $165 \text{ MPa(m)}^{1/2}$ . Obviously, the fracture toughness measurement via micro scratch test in this study is about an order of magnitude lower compared with literature reports.

Table 3-4. Fracture toughness of 308L weld measured from micro scratch test.

Condition	As-weld	Aged 2226 h	Aged 6000 h
$K_{IC} / \text{MPa(m)}^{1/2}$	22.65	20.99	17.71

The micro scratched surface was further examined using the previously mentioned SEM data for tensile fractography. Enlarged images were obtained to identify the surface relief pattern adjacent to the scratch. No crack was observed on either side of the rim for the as-welded condition shown in Figure 3-18 A) and B). In comparison, cracks started to emerge on the upper rim for the 2226 h aged weld shown in Figure 3-18 C) and D). Crack development was observed all over the upper rim for the 6000 h aged sample shown in Figure 3-18 E) and F). Furthermore, the strain of the scratch propagated towards the nearby substrate region (marked in the green circle) causing a corrugated pattern in Figure 3-18 B) right above the extruded rim. In comparison, the same region above the crack in Figure 3-18 D) induced only some quasi-periodic

surface relief patterns as a sign of local strain relief. No surface relief patterns were found where nearby cracking had initiated for the 6000 h aged 308L weld in Figure 3-18 F).

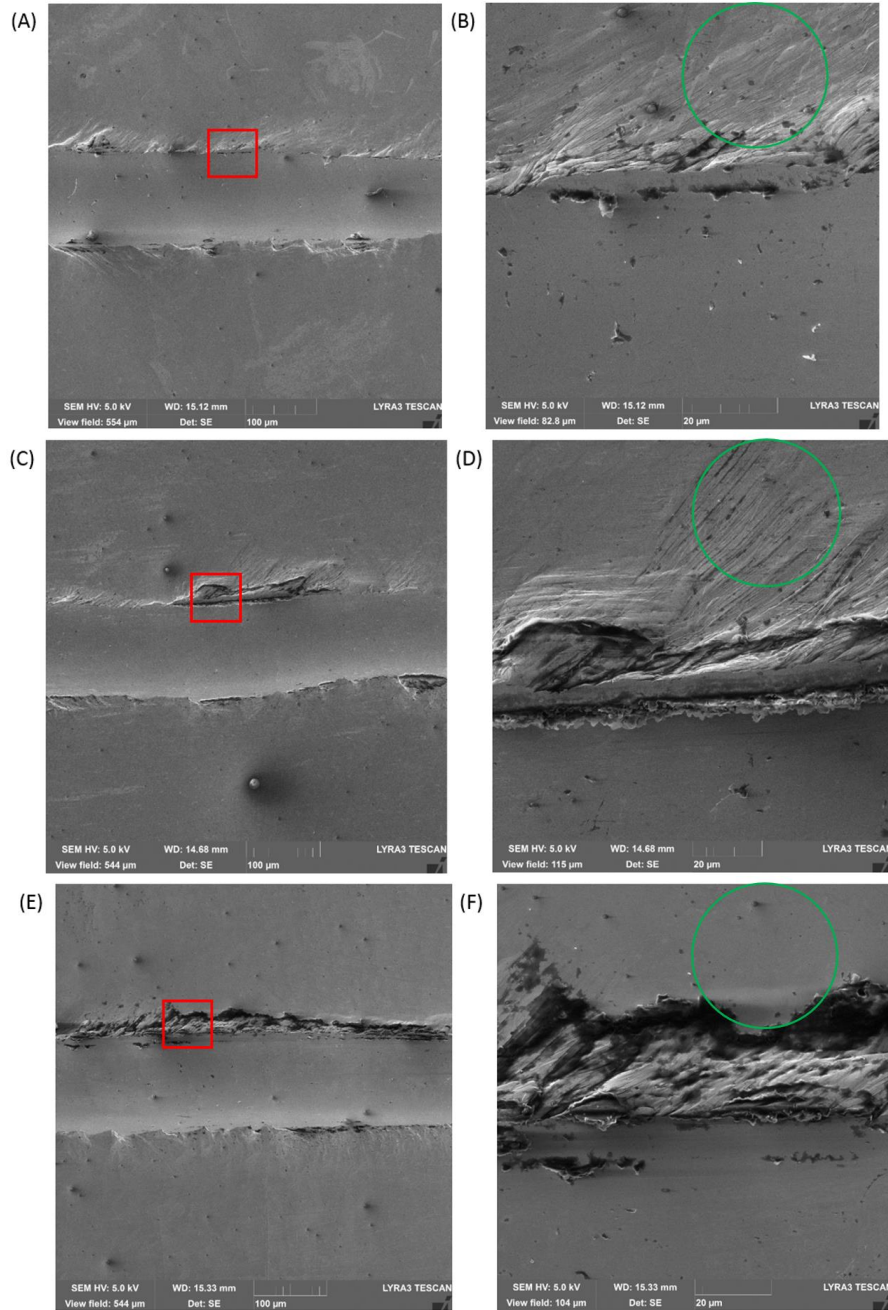


Figure 3-18. SEM images of the scratch of 308L weld for (A) and (B) as-welded, (C) and (D) aged for 2226 h, (E) and (F) aged for 6000 h, images on the right are the red box area in images on the left.

## CHAPTER 4 DISCUSSION

### 4.1 Macrostructure and Metallurgical Analysis

Due to the low grain boundary angle of the austenite, the current etching can clearly reveal only the austenite/ferrite phase boundary for CF-3 by optical microscopy. The ferrite phase was easily etched, while austenite remained quite unaffected. The estimated grain size is on the scale of a few mm based on visual inspection. Electron back-scattering diffraction (EBSD) is known to recognize grains with different orientations. However, most commercial EBSD equipment is incapable of working on grain sizes this large. Samples would have to be tilted with the working distance as small as possible. Thus, this method was not considered.

#### 4.1.1 CF-3

The CF-3 in both unaged and aged samples exhibits a duplex structure of ferrite and austenite phases shown in the optical images in Figure 3-1. No obvious macro defects such as bubbles or large inclusions were observed. The average size of the ferrite phase is around a few  $\mu\text{m}$ . Based on the chemical composition provided in Table 2-1, the equivalent Cr and Ni content for CF-3 was calculated to be 20.5 wt.% and 9.4 wt.% following Eq. 4-1 and 4-2 [77,83].

$$Cr_{eq} = Cr + Mo + 1.5Si \quad (4-1)$$

$$Ni_{eq} = Ni + 30C + 0.5Mn \quad (4-2)$$

According to the pseudo binary phase diagram of Fe-Cr-Ni with Fe balanced at 70 wt.%, the phase transformation sequence of the CF-3 cast will be  $L \rightarrow L + \delta \rightarrow L + \delta + \gamma \rightarrow \delta + \gamma$ . As can be seen, ferrite is the primary phase of the cast. Most of the ferrite would then transform into austenite similar to the diagram shown in Figure 1-4.

However, depending on the actual cooling rate of the casting, not all ferrite phase may have sufficient time to be transformed into austenite. In this case, for CF-3, around 24% ferrite is retained in the dendrite core.

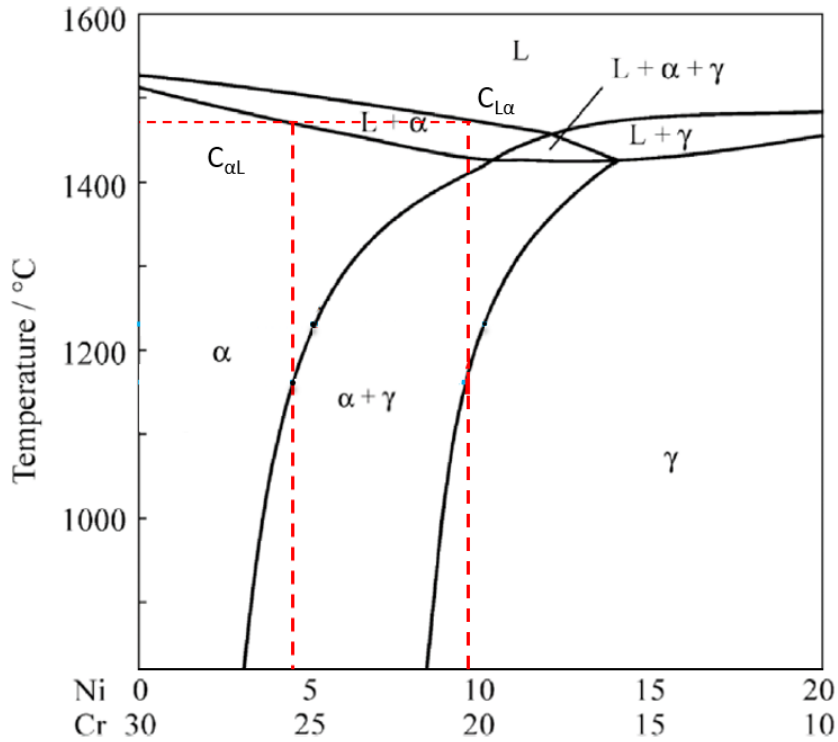


Figure 4-1. 70 wt.% Fe-Cr-Ni pseudo binary phase diagram. (Source: Ref. [11])

No obvious macro-segregation was observed in the SEM images shown in Figure 3-3. The actual chemical composition variation for elements such as Fe, Cr and Ni in ferrite phases is quite small based on APT analysis. One reason for this can be that all those CF-3 samples were from the exact same interior region of cast slab. Thus, it is quite possible for the sample to have very close microstructure and chemical composition. As explained by Louthan [84], the dendritic structure tends to have a certain degree of constitutional variation, especially between the dendritic arms and interdendritic domains. This can be reflected in the chemical compositions of austenite and ferrite having distinctive Cr and Ni content. Such a difference could also be traced

back to the phase diagram and the solidification process. As shown in Figure 1-2, the binary phase diagram of Fe-Cr has a very flat solidus line when the Cr content is less than 35%. This means that concentration variation will have a very small impact on the solidus temperature upon solidification. The addition of Ni element would expand the  $\gamma$  loop area and create the region of L +  $\alpha$  +  $\gamma$  when Ni content exceeds 11 wt.%, as calculated by Li [11] and shown in Figure 4-2. Because Li's sample had very close chemical composition to that in this study for CF-3 shown in Table 2-1, Li's result is used to simulate the solidification process for CF-3 in this study. The cooling rate was estimated to be less than 10 °C/s for static casting. Non-equilibrium solidification and unstable dendrite growth were assumed.

As the initial ferrite solidifies from the liquid, the chemical composition of the ferrite would be  $C_{\alpha L}$  owing to solute partitioning based on the phase diagram in Figure 4-1 [85]. The corresponding Ni and Cr concentrations agree quite well with those measured in this study. Due to the enrichment in Cr with less Ni, the initially formed ferrite would be the last to transform into austenite phase, as the transformation temperature is much lower compared with ferrite with composition of  $C_{L\alpha}$ . Thus, the retained ferrites residing in the dendrites tend to have chemical compositions similar to that of  $C_{\alpha L}$ . In comparison, the austenite phase tends to have more Ni and less Cr.

Fu [85] investigated the phase transformation by directional solidification on liquid stainless steel 304. He further concluded that, depending on the cooling rate, the duplex structure could be formed via two mechanisms. Under fast cooling,  $\delta$  ferrite could be retained owing to the incomplete ferrite-to-austenite transformation. If the cooling rate is sufficiently slow, ferrite will fully transform into austenite. Then a subsequent reverse

transformation of austenite into  $\alpha$  ferrite will occur for samples with greater Cr content. Furthermore, EDS across the ferrite/austenite phase boundary clearly indicated that ferrite has greater Cr and less Ni content compared with the adjacent austenite.

Mhuru [86] recently extracted APT results at the interface area of ferrite/austenite phases in unaged CF-3. A sharp transition of Cr and Ni across the phase boundary was observed with greater Cr and less Ni at the ferrite side. It has to be pointed out that the CF-3 steel in Mhuru's research was solution annealed at 1065 °C for 2h followed by water quench. Annealing at such temperature will provide a good homogenization of the chemical composition of each phases with little impact on the phase transformation.

Figure 4-1 only reveals the equilibrium constitution of the steel alloy above 800 °C. Based on previous metallurgical analysis, the austenite phase with chemical composition around  $C_{L\alpha}$  or more to the right of Figure 4-1, is in its equilibrium state at around 400 °C. Thus, long-term thermal exposure tends to have very limited effect on its phase stability at relatively low temperature. This conclusion has been frequently validated by various TEM images, diffraction patterns and APT results [87,88]. Ai [89] performed XRD, EDS, SEM and TEM on thermally aged DSS 7MoPlus steel on both the ferrite and austenite phases. The only phase transformation observed was the mottled phase by spinodal decomposition in ferrite.

#### **4.1.2 308L Weld**

The metallurgical phase solidification of 308L weld is very similar to that of CF-3. The weldment fusion zone has a much faster cooling rate compared with the casting. Because of the cooling rate difference, the varied extent of constitutional supercooling allowed for the transformation planar->cellular->columnar dendrite->equiaxed dendrite illustrated in Figure 4-2 [76,77,90]. Similar to that of CF-3, a duplex structure of ferrite

and austenite was formed but with much smaller dimension [91]. In this study, only the equiaxed region is shown in Figure 3-3 and Figure 3-4. Other regions of the as-weld 308L are included in the Appendix D.

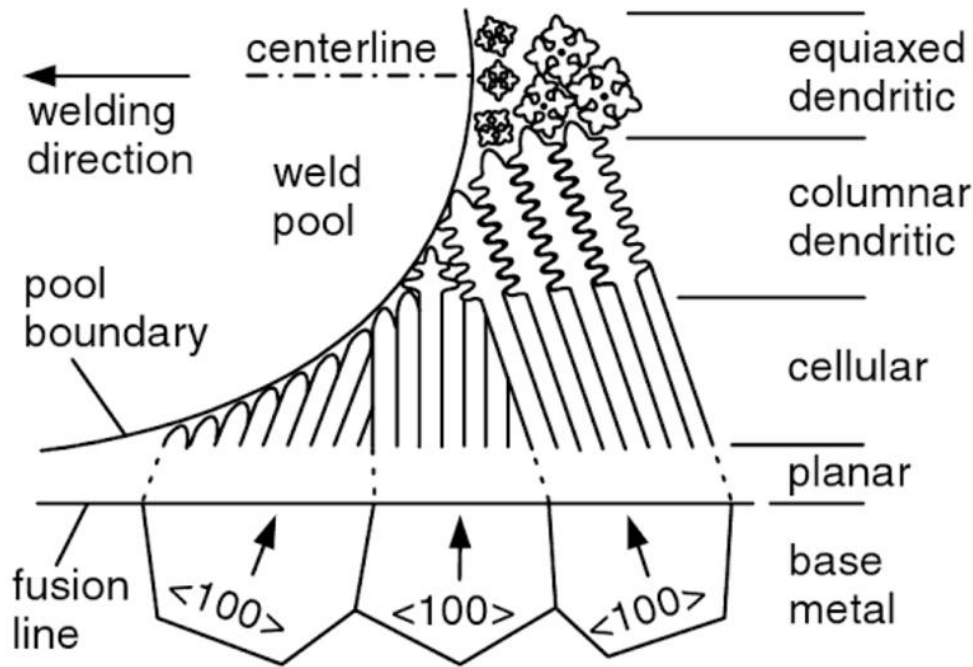


Figure 4-2. Variation in solidification mode in weld. (Source: Ref. [76])

## 4.2 Microstructure Evolution in Ferrite-Spinodal Decomposition

### 4.2.1 Synergistic Effect of Spinodal Decomposition

The long-term thermal exposure of CF-3 at 400 °C for 10 kh was studied to simulate the in-reactor service degradation process. The atom probe results of ferrite in Figure 3-1 successfully reveal the Cr clustering behavior during thermal exposure. Such a result is in close correspondence with literature reports. The combined effect of thermal aging and neutron irradiation on the ferrite phase degradation is demonstrated on spinodal decomposition shown in Figure 3-1. As reviewed by Wilkes [92], it was experimentally and theoretically shown that irradiation-induced disordering competes with the process of thermal ordering. The resulting phase structure is strongly

dependent on the defect production rate and the irradiation temperature, which determine the concentration of defects and their mobility. Either the radiation accelerates the approach to thermal equilibrium, or radiation-induced non-equilibrium phase precipitation occurs. The mechanism of microstructural evolution can be further complicated by Mn, Mo, Si and other minor alloying elements. One recent study shows that 6.4 MeV Fe<sup>3+</sup> ion irradiation at 300°C can suppress spinodal decomposition by decreasing the fluctuation of Cr concentration in the Cr-rich  $\alpha'$  phase [93]. However, Miller [36] studied the effect of neutron irradiation on spinodal decomposition of a Fe-Cr model alloy, and it was found that the spinodal decomposition in a Fe-32% Cr alloy was significantly enhanced by neutron irradiation after 0.03 dpa at 290°C. This controversy regarding irradiation effect on the spinodal decomposition of aged ferrite can be attributed to the difference in incident particles, dose rate, temperature and the material itself. The dose rate in this study ( $10^{-9}$  dpa/s) is of the same order of that used in Miller's study. Therefore, it is not surprising that both studies show an enhancement of spinodal decomposition from neutron irradiation.

#### **4.2.2 Irradiation Enhancement Estimation**

After 10,000 hours aging at 400°C, a Cr-Fe concentration profile nearly identical to that of 0.08 dpa-neutron irradiation at 315°C was indicated by the frequency distribution in Figure 3-2. The Cr and Fe peaks both become broader after thermal aging or neutron irradiation. The Cr peak broadening to a lower concentration (<25.24 at.%) corresponds to the increased volume of the Cr depleted zone, and broadening to a higher concentration (>25.24%) indicates the increased volume of Cr-enriched zones. This study demonstrates that low dose neutron irradiation could induce a spinodal decomposition of delta ferrite in a similar fashion to that induced by thermal aging. With

the assumption that the individual aging and irradiation experiments induced equivalent extents of Fe-Cr demixing, it is possible to estimate the irradiation enhancement rate of the system.

By applying the Arrhenius equation in Eq. 1-1, with the activation energy of 164 kJ/mol, aging at 400 °C for 10,000 h is equivalent to aging at 315 °C for 692,000 h. During neutron irradiation at 0.08 dpa at 315 °C with a dose rate of  $2.8 \times 10^{-9}$  dpa/s, the total time consumed was 7,936 h. Thus, for an estimated aging at 315 °C for nearly 79 years of thermal diffusion, with the help of neutron irradiation at the same temperature less than a year is needed to reach the same extent of ferrite decomposition. This comparison suggests that neutron irradiation-assisted diffusion kinetics in Fe-Cr system is approximately 80 times faster on average. Such a simulated result is quite similar to what Miller [36] discovered in 1996. In fact, based on neutron irradiation physics, point defects introduced by irradiation normally have a greater density compared with the thermally-activated vacancy density. In addition, the demixing behavior of Cr-Fe is a diffusion-dependent process especially via vacancy. It is obvious that neutron irradiation can have a direct positive impact on the Cr-Fe demixing process.

Similar irradiation enhancement estimations on the Fe-Cr system were performed by Li [94].  $Kr^+$  with 1 meV energy was used to irradiate the CF-8 alloy at 400 °C with fluence of  $1.88 \times 10^{19}$  ions/s. Subsequent APT investigation was carried out on the ferrite phase. The steady-state model was adopted to calculate the characteristic diffusion distance. A diffusion coefficient in ion-irradiated ferrite was calculated to be  $3 \times 10^{-16} \text{cm}^2/\text{s}$ . With a referenced thermal diffusivity of  $3 \times 10^{-19} \text{cm}^2/\text{s}$  for the Fe-Cr system [95], an enhancement of 3 orders of magnitude by ion irradiation was concluded.

However, the temperatures for both the calculated and referenced diffusivity were not clearly mentioned. The element for the diffusivity was not clearly stated either. In addition, the article later concluded that ion irradiation would suppress the reaction of spinodal decomposition which contradicts the results of enhanced diffusion kinetics of the Fe-Cr system. Because of these reasons, the enhancement calculation from this article was not considered.

#### **4.2.3 Spinodal Decomposition at High Dose Irradiation**

Neutron irradiation was observed to synergistically enhance the ferrite decomposition process [96]. The introduction of large quantities of point defects such as interstitials and vacancies could significantly affect the microchemistry of the ferrite phase. The correlation of the wavelength vs irradiation dose in Figure 3-4 shows a steady wavelength growth because of neutron irradiation. With the dramatic increase in vacancies, the diffusion kinetics of Cr atoms migrating through the ferrite matrix was significantly enhanced. Based on this plot, the wavelength growth rate gradually decreases. A possible wavelength saturation value at 20.03 nm is illustrated in Figure 3-8. In general, the wavelengths extracted for high-dose irradiated CF-3 are much greater than those reported for CF-3 under elevated aging conditions. One possible reason could be that the wavelength is dependent on the diffusivity of Cr atoms. Neutron irradiation induces faster Cr diffusion and yields a greater wavelength. However, the low-dose neutron irradiation induced an identical wavelength compared with aging at 400 °C at around 6.8 nm. This indicates that high dose irradiation modified more than just the diffusion kinetics of the Fe-Cr system, and modified the microchemistry of the Cr migration as well.

Based on the classical spinodal decomposition theory established by Cahn [34], once the wavelength of the decomposition is observed, it should stay at a critical value from then on. However, in this study, an obvious wavelength evolution progression was observed. To properly explain the wavelength saturation behavior, Cahn's theory was modified to include three-stage spinodal decomposition from the homogeneous state toward thermal equilibrium as shown in Figure 4-3. The measured average Cr concentration is around 25% for ferrite and this value was used for the homogeneous state. For those Fe-rich and Cr-rich domains, the actual total concentration of Fe and Cr was measured to be greater than 97%. To simplify the model, the influence of other alloy elements, such as Ni and Si, was not considered for equilibrium estimation.

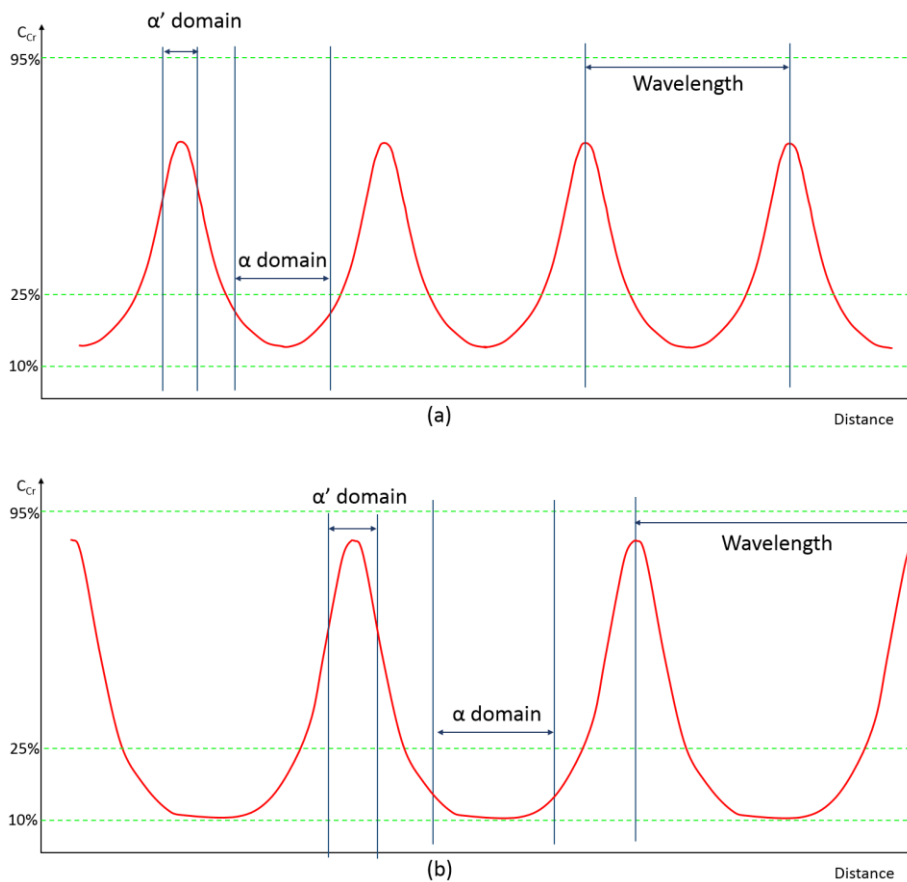


Figure 4-3. Schematics of (a) early-stage, (b) intermediate-stage and (c) late-stage of spinodal decomposition.

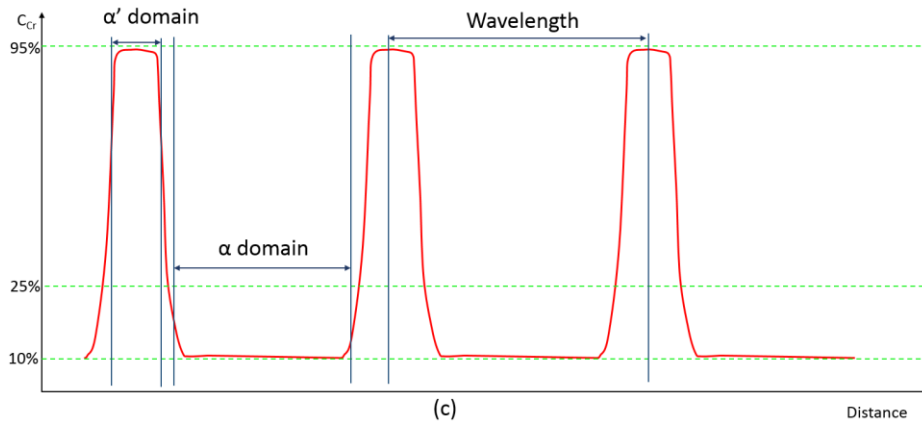


Figure 4-3. Continued.

To consolidate the thermal equilibrium chemical composition of each child phase, long-term aging at low temperature on the Fe-Cr system is needed. However, no related data has been published yet. There have been several efforts for modeling and computation of this equilibrium concentration of Fe-Cr by William, Chandra, Xiong and Zhou [29,35,97,98]. For the equilibrium concentration of  $\alpha$ , 10 at.%Cr was selected. And for the equilibrium concentration of  $\alpha'$  phase, the prediction seems quite inconclusive, as the data is much harder to obtain and validate. It is commonly accepted that the chemical concentration of Cr should be greater than 95 at.%. Thus, a value 95 at.% was selected for a conservative calculation. The equilibrium volume fraction of the Cr rich domain at 95% was calculated to roughly 17% based on the lever law

As can be seen in the three different stages for Fe-Cr with 25 at.%,  $\alpha$  phase reached its equilibrium concentration much earlier compared to the  $\alpha'$  phase, while the wavelength increased rapidly during the early stage. As more and more  $\alpha$  phase arrived at its equilibrium status, the contribution to wavelength was limited to the shrinkage of the interface. Both processes eventually slowed wavelength growth and arrived at late stage wavelength saturation.

Krishan and Abromeit [99–101] proposed a model of spinodal decomposition under neutron irradiation of AB alloys. Because the neutron irradiation-induced defect supersaturation, an amplification factor on both spinodal decomposition wavelength and amplitude was developed based on Cahn’s theory. The critical wavelength was shifted to a larger value. An equation based on the model of wavelength is expressed in Eq. 4-3.

$$\lambda \approx 2\pi \left( \frac{1}{Kn_v|F|} \right)^{1/2} \quad (4-3)$$

where  $K = 4\pi r_r/\Omega$ ,  $r$  is the recombination radius,  $n_v$  is the averaged vacancy concentration,  $F$  is the parameter based on the defect formation rate. The detailed interpretation and clarification of these parameters is quite complicated and not in the realm of material science.

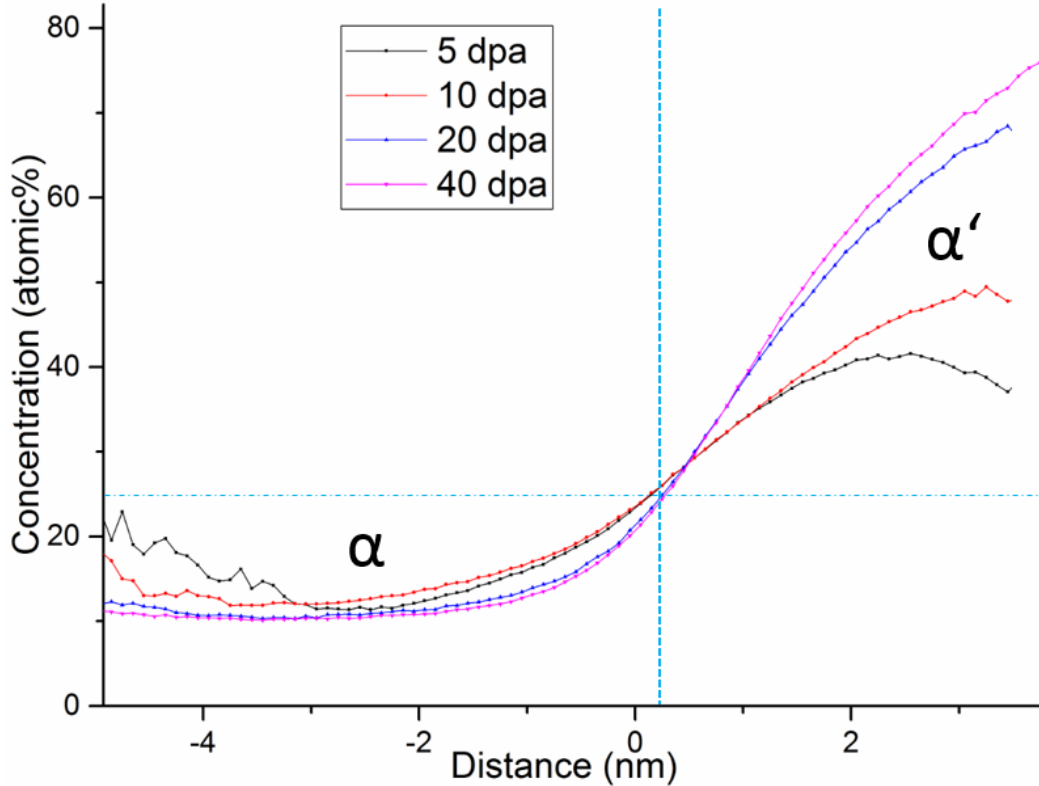


Figure 4-4. Cr proxigrams in ferrite of irradiated CF-3.

To better visualize the shift of short/long range diffusion of spinodal decomposition from early to intermediate stage, the Cr proxigram was plotted in Figure 4-4. The light blue vertical broken line indicates the medium position of the diffusing interface. The demixing of Fe and Cr through uphill diffusion corresponds with this phenomenon. No sign of nucleation and growth was present, because a sharp interface was not observed. A smooth concentration transition from the  $\alpha/\alpha'$  was observed for 5 dpa and 10 dpa doses, where diffusion of Cr and Fe element be quite local. In comparison, for 20 dpa and 40 dpa doses, a lower plateau was formed, where  $\alpha$  resides with Cr concentration close to 10%. On the one hand, this plateau is actually the sign of  $\alpha$  phase at thermodynamic equilibrium status. No extra Cr could be depleted by minimum Gibbs free energy status. On the other hand, the growth of the  $\alpha'$  phase requires the diffusion of Cr via a much longer distance from nearby a Cr rich region, such as  $\alpha'$  phase with smaller Cr concentration. Combined with the frequency distribution of Cr in Figure 3-3, a peak shifting saturation was observed near 10% for ferrite irradiated at 40 dpa. Such a phenomenon suggests that a lower bound of Cr concentration was reached at 40 dpa.

The above results and modeling agrees quite well with the data published by Hamaoka and Pareige [44,64]. Hamaoka carried out aging experiments on CF-3M with subsequent APT investigations of the ferrite phase. The Cr-Fe demixing sequence of aging at 400 °C for 100 h to 5000 h was compared via frequency distribution. Both peak shift and peak broadening were captured similarly. This implies that the effect of neutron irradiation on Fe-Cr demixing is similar to that of thermal aging. Due to the lack of wavelength information, the trend of wavelength changes were not revealed in

Hamaoka's discussion. Thus, it was not taken into account. In comparison, Pareige's experiment was performed by aging CF8M at 350 °C and ATP was later carried out on the ferrite phase. A method of frequency distribution of distances developed by Novy [102] was used to extract the wavelength information of Cr modulation. Overall, there was a logarithmic relationship of increasing wavelength with increased aging time. An equivalent time exponent was estimated to be 0.16. To explain the wavelength increase, it was concluded the Fe-Cr system was in its early stage even after 20 years of thermal aging at 350 °C.

In order to generate a more direct comparison of the wavelength of Cr modulation in the ferrite of the neutron irradiated CF-3, the author attempted to apply the frequency distribution of distances, but no valid wavelength was successfully extracted. One possible reason could be that the randomization of the region of interest was not well formulated. Another reason could be that the wavelength yielded in this study is too large, making this extraction method invalid.

Novy [103] carried out aging experiments on Fe-20 at.% Cr model alloys at 500 °C. A non-steady coarsening behavior of the Cr rich  $\alpha'$  phase was observed. A lower solubility limit at 500 °C was found at 14 at.%, which makes sense compared with 10 at.% used in this study at 315 °C. The actual trend of the spinodal curve for Fe-Cr phase diagram shown in Figure 1-2 implies that the lower the aging temperature, the lower the content of Cr in the Cr-depleted  $\alpha$  phase at equilibrium. This evidence indicates that even under high-dose neutron irradiation, the phase diagram of Cr-Fe system was not significantly modified.

#### 4.2.4 Spinodal Decomposition under TEM

Currently, it is commonly accepted that a mottled phase should be visualized more obviously with the bright field image captured along the [001] zone axis compared to other alignment directions [81,104]. The details of the spinodal decomposition of 308L weld are shown in Figure 3-3. The incident electron beam was aligned along [001] zone axis of the ferrite phase. The modulated contrast resembling the surface of an orange peel was visualized in TEM micrographs in both aged and irradiated 308L welds. Such an appearance corresponds to the finding by Nichol et al [105]. However, the fundamental mechanism of such a mottled contrast is still unknown. Recently, Westraadt [106] explained that this modulated contrast could be due to a small coherency strain which is more evident along the [001] direction. However, he also stated that other factors, such as sample thickness fluctuation and ion milling defects, could also induce a similar modulated contrast.

The TEM image is a perfect mapping tool for APT data reconstruction. As shown in Figure 3-9 a) and b), the reconstructed small micrograph corresponds to the clustering of Cr element by APT. Only Cr ions were included as the dark region. Both the aged and irradiated APT reconstruction highly mimics that of TEM results. Such a correspondence not only helps validate the APT reconstruction results, but also helps to possibly explain that the contrast in the TEM micrograph could be due to the  $\alpha/\alpha'$  phase chemical composition difference. The wavelengths of the Cr modulation calculated by RDF for aged and irradiated 308L welds show very close values at 6.4 nm and 6.8 nm for aged and irradiated samples, respectively. Such a similarity in wavelength of Cr modulation was also indicated in the TEM micrographs.

The imaging of spinodal decomposition via TEM has been difficult. Weng [81] performed thermal aging experiments on DSS 2205 at 475 °C. Further TEM imaging with a FEG/TEM Tecnai F30 on the ferrite phase was performed. The modulated contrast was obvious when the electron beam was in alignment with the  $\langle 001 \rangle$  direction of ferrite. The reason for this was not clearly discussed in his report. He also mentioned that the mottled phase contrast could be the result of differential oxidation of the  $\alpha/\alpha'$  phase. This might not necessarily be true in this study. As can be clearly seen in the Cr only APT reconstruction, no oxidation occurred. A similar mottled contrast by the APT reconstruction revealed that it could be due to the Z contrast or the composition difference of the  $\alpha$  and  $\alpha'$  phases. Recently, Westraadt [106] developed a STEM imaging method based on a similar mechanism. TEM experiments were performed on aged Fe-36 wt.%Cr model alloys. The material was solution treated followed with aging at 500 °C. A JEOL ARM 200F TEM was used for the imaging with operation voltage at 200 kV. The TEM foil was jet polished similar to the aged specimens in this research. The nano-scale mottle contrast via STEM of the model alloy highly resembled the APT reconstruction in this study. Subsequent compositional analysis proved that the mottled signal intensity corresponded to the STEM image which is known to be sensitive to the Z contrast. The modulated contrast caused by chemical composition difference clearly indicated the modulated morphology of spinodal decomposition in the ferrite phase. It is estimated that the TEM sample used in his study could be as thin as 10 nm. Otherwise, the 3D superimposition of the modulated structure would definitely dissipate the 2D projection. Up until now, there is no other TEM investigation on spinodal decomposition

of ferrite under neutron irradiation. Thus, little comparison could be made as to the irradiation-induced spinodal decomposition.

### **4.3 Microstructure Evolution in Ferrite-G Phase**

#### **4.3.1 G Phase Formation under Irradiation and Aging in CF-3/308L weld**

As shown in Figure 3-4, a direct comparison between the aged CF-3 at 10,000 h with the aged and irradiation sample indicated that the combined effect could dramatically enhance the G phase in both size, density and volume fraction. The spinodal decomposition-assisted flux could play a partial role in this result. More importantly, the irradiation-induced defects provided a high-energy status for G phase to nucleate inside the ferrite matrix, where both interfacial and strain energy could counteract. With the irradiation-enhanced diffusion on those solute elements, such as Ni, Si and Mn, the G phase growth was also favored. Such an increase in both size and density directly led to the increase of its volume fraction. The 400 °C thermal aging induced more solute cluster nuclei while the low dose irradiation promoted coarsening.

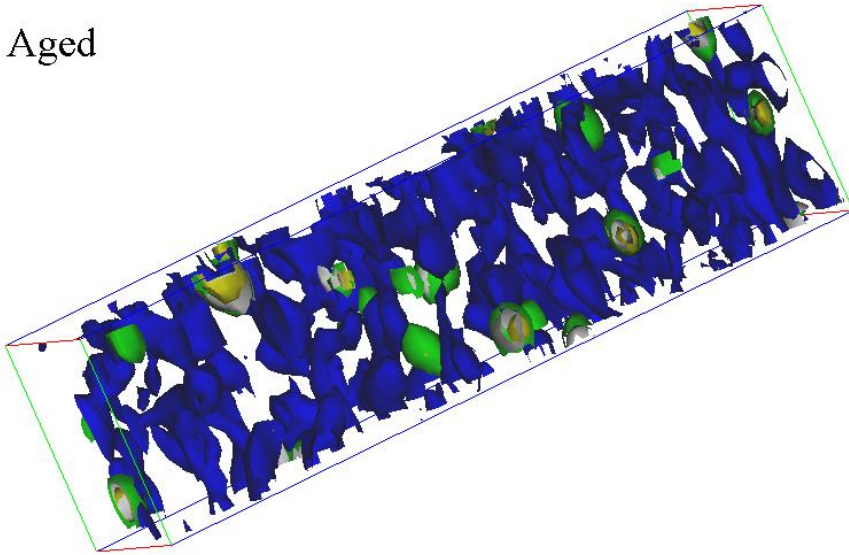
The synergistic effect of neutron irradiation and thermal aging on G phase precipitation has rarely been studied and reported. However, Li [94] performed similar experiments with heavy ion irradiation on aged CF-8 with subsequent APT cluster analysis. The thermally aged CF-8 at 400 °C for 10,000 h yielded G phase precipitates with sizes of 4.8 nm and density of  $9.7 \times 10^{22}/\text{m}^3$ . Such results are quite comparable to those for CF-3 under same aging conditions. However, the low dose heavy ion irradiation suppressed the size of the G phase, with insignificant impact on the number density. These contrary results could be due partially to the time spent to reach the accumulated irradiation dose level. Neutron irradiation performed in this study occurs at a much smaller dose rate than that observed for heavy-ion irradiation. The extended

irradiation in this study would allow the irradiation induced-defects to interact with the nearby atoms to enhance the diffusion kinetics.

The densities of the G phase observed in the 308L weld summarized in Table 3-3 are about an order of magnitude greater than that of CF-3 ferrite. This is probably because a large number of favorable sites at the interface of  $\alpha/\alpha'$  were not involved with G phase nucleation in CF-3 ferrite. It was also found that irradiation weldment promotes a greater number of clusters as compared with irradiated CF-3, probably because, the ferrite in 308L weld typically contains more Mn and less Si than that of CF-3.

Concurrent evolution between solute clustering and spinodal decomposition was proposed by Mateo and studied by Danoix [39,107]. It was claimed that the G-phase particles were located at  $\alpha-\alpha'$  phase interfaces and no particles were observed within the  $\alpha$  or  $\alpha'$  domains. Our study shows that the solute clusters are all located in the Cr-depleted zone, as shown in Figure 4-5. As spinodal decomposition progresses, domains enriched in iron and domains enriched in chromium form over the parent solid solution. It seems that Ni and Mn are rejected from the Cr-enriched domains as the  $\alpha'$  phase develops to its equilibrium composition. The solute clusters should nucleate at the  $\alpha-\alpha'$  interfaces and unsymmetrically grow into Fe-rich  $\alpha$  phases. It was reported that Si was rejected from either domain as Fe started to enrich in the  $\alpha$  phase. However, due to its relatively low concentration in the solute clusters and the ferrite matrix, it is difficult to determine the domain from which Si was rejected. Overall, a strong interaction between the spinodal decomposition and solute cluster nucleation and growth was well confirmed in the irradiated and aged 308L weldment ferrite.

Aged



Irradiated

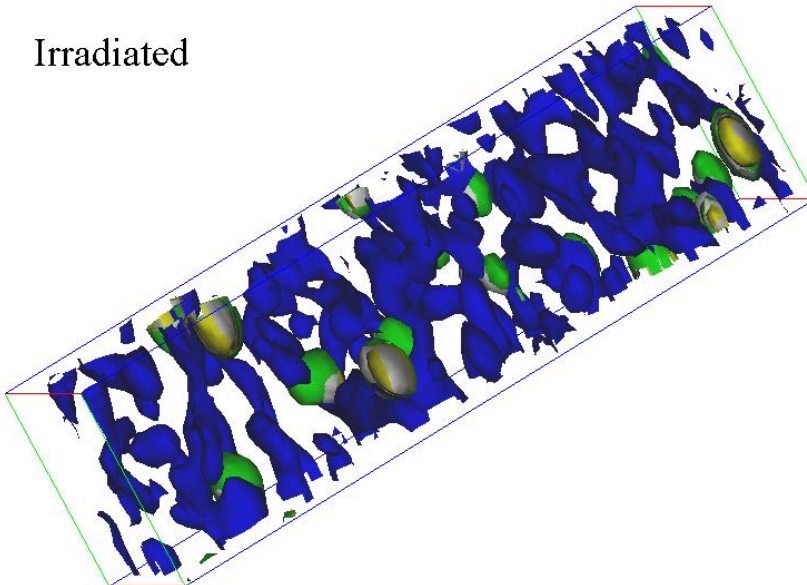


Figure 4-5. Iso-surfaces of Mn (Gold)-Ni (Green)-Si (Gray) clusters and interfaces of Cr (Blue) enriched  $\alpha'$  phases: Aged (33.58%Cr-7.47%Mn-13.39%Ni-5.6%Si) and Irradiated (33.57%Cr-6.72%Mn-14.31%Ni-5.74%Si).

Takeuchi [43,54] performed two separate neutron irradiation experiments on stainless steel electroslag weld overlay claddings with irradiation fluence at  $7.2 \times 10^{19} \text{ n cm}^{-2}$  and  $7.2 \times 10^{23} \text{ n cm}^{-2}$ . The corresponding irradiation temperatures were 280 °C and 290 °C, respectively. His comparison of aging and neutron irradiation on ferrite decomposition in weld indicated that irradiation tends to increase the activity of Si, while

aging yields greater Ni clustering. Both are solute elements of the G phase cluster. Such a phenomenon was not identified in this study because the fact that G phase clustering in aged and irradiated welds behaved quite similarly. In addition, the frequency distribution results of Ni, Si and Mn used in Takeuchi's report could probably be over interpreted. An obvious issue is the binomial distribution which was not in agreement with the average element content. Thus, Takeuchi's discovery was not considered in this study.

#### **4.3.2 G Phase Coarsening under High Dose Irradiation in CF-3**

As shown in Figure 3-5, the number density of the G phase clusters decreased with high irradiation doses. This could be largely due to the fact that the interface area of  $\alpha/\alpha'$  phase kept shrinking, limiting the nucleation action of those Ni and Si clusters. The chemical composition ratio of the high dose irradiated ferrite has not been reported previously in CF-3. The average size of the G phase clusters identified after 20 dpa was much greater than that observed in CF-3 under accelerated aging conditions using an atom probe by other researchers [107]. Such evidence indicates that the G phase coarsening in ferrite was significantly enhanced under high dose neutron irradiation due to the  $\alpha/\alpha'$  interface shrinkage. With the gradual concentration increase of Ni, Si and Mn, no saturation or thermodynamic equilibrium trend was observed based on APT data. This phenomenon is quite different from a conventional precipitation scenario where an equilibrium chemical composition was observed.

Similar high dose irradiation results on CASS have not been reported. Intermediate dose ion irradiation was performed on aged CF-8 by Li [94] at 400 °C with corresponding irradiation dose up to 3.82 dpa. In the irradiation dose range of roughly 1 dpa – 3.82 dpa, Li observed that the G phase precipitate exhibited a number density

increase and mean size decrease. Such a trend is contrary to the result found in this study. Li did not explain the mechanism for such a phenomenon. The author believes that the impact of high-energy ion irradiation in Li's experiment significantly interfered with the precipitation ordering behavior due to irradiation damage. This could help explain the G phase mean size decrease. The number density increase is likely due to the competition of thermal nucleation and irradiation damage, where thermal diffusion was more important than the irradiation disordering. Thus, the results from Li's article were not considered in this study.

Pareige's [44] long term (0 year – 20 years) thermal aging experiment on CF8M can help compare the effect of thermal aging and high dose neutron irradiation on G phase precipitation. A steady evolution of G phase in mean size was observed in CF8M aged at 350 °C. Such a characteristic trend of precipitation behavior corresponds to the coarsening behavior of neutron irradiation observed in this study. As for the number density, a trend of initially increase followed by decrease was observed by Pareige with peak at 30,000 h aged condition. In comparison, the number density of G phase found in this study kept decreasing. However, the irradiation dose range did not strictly follow the low-intermediate-high dose trend similar to that of the thermal aging experiment in Pareige's report. A dose range of 5 dpa – 40 dpa could be interpreted as corresponding to aging time greater than 30,000 h. such a correlation indicates that high dose neutron irradiation could easily accelerate the thermal aging phase decomposition process in respect of G phase precipitation. The number density of G phase found in CF-8M tends to be an order magnitude higher than that of CF-3. Part of the reason could be due to the higher Mo content in CF-8M that could facilitate G phase clustering behavior as a

solute element. The mean size increase rate in CF-8M was not as great as that of CF-3 under high dose irradiation (0.8 nm to 1.8 nm with corresponding aging time from 2000 h to 20,000 h). Such a slow size increase trend is in good agreement with Hamaoka's [64] report. This could be explained by the enhanced neutron irradiation diffusion of solute atoms, which facilitates the coarsening behavior. The average solute concentration of Ni, Si and Mn in Pareige's report shows an increasing trend with the increase of thermal aging time, which is similar to the trend observed in this study. In comparison, Hamaoka's report indicates that the average solute element composition in G phase stay relatively the same. Both Pareige and Hamaoka used a filter as a concentration threshold to categorize the G phase clusters. The filter concentration for Ni, Mn and Si used in Pareige's report was much smaller than that in Hamaoka's report.

#### **4.3.3 TEM investigation and APT validation**

To compare the ATP reconstruction results for the G phase precipitation with the TEM micrographs, a specific APT reconstruction of the 20 dpa irradiated CF-3 ferrite was performed. In Figure 4-6, the object in white denotes the G phase precipitate created from the Ni iso-surface with ionic concentration at 20 at.%. The background blue spheres indicate the Fe and Cr atoms as representative of the ferrite matrix. Overall, the number density of G phase reconstructed in IVAS corresponds to that of TEM results. However, the size of the G phase constructed from iso-surface is much larger than that measured from TEM. This can be explained by the G phase in ferrite, in which only the core area contributes to the diffraction with the F.C.C. structure. Meanwhile, that enrichment in the exterior region of G phase is still coherent with the ferrite matrix. Thus, its existence is not revealed under TEM diffraction contrast. This means that the iso-surface of Ni used to bind the G phase is relies highly on the

clustering behavior of Ni. Thus, it is impossible to tell where the phase boundary is based on its concentration in IVAS reconstruction. In this case, the sizes of Ni, Si and Mn clusters are much larger than the G phase precipitate size.

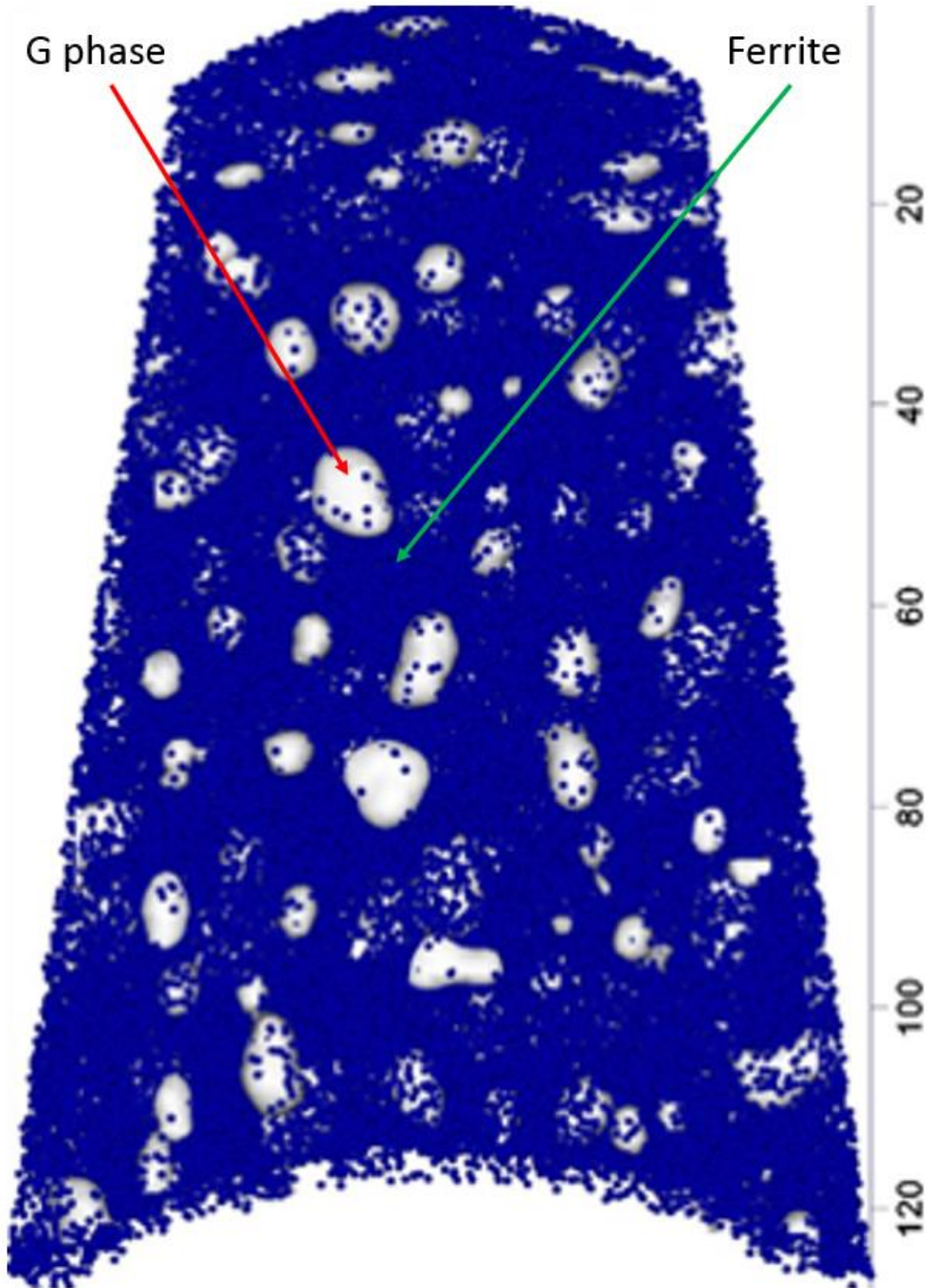


Figure 4-6. G phase precipitate in ferrite of CF-3 irradiated at 20 dpa reconstructed in IVAS.

To elucidate this interpretation discrepancy in IVAS reconstruction, a more detailed 1-D concentration profile was represented as a cylinder with diameter of 2 nm passing through a quasi-spherical Ni, Si and Mn cluster center region shown in Figure 4-7. To best reveal the element concentration profile, the length along the z axis of the cylinder was set at 20 nm. In addition, the step size for the profile was set at 0.6 nm. The calculated concentration profile along the z axis is summarized in Figure 4-8. The line of iso-surface concentration of Ni is presented to mark the corresponding cluster size measurement and a reading of 7.1 nm can be obtained. Such a number is slightly smaller than the size identified by the MSM technique shown in Figure 4-8. In MSM calculation, the size of the clusters are based on the phase boundary which in Figure 5-12 for example, occurs at Ni with concentration around 5 at.%. In comparison, the estimated size and position of the actual G phase is marked along a relative plateau of Si element. Inside this area, the Ni element does not seem to reach a steady level, possibly because the Ni composition is more sensitive to the calculation step size at 0.6 nm.

To summarize, the interface region detection is the major challenge causing the difference in TEM and APT measurements of G phase size. In this study, cluster identification via the MSM technique is clarified to be effectively extracting the cluster size and composition, rather than the G phase. Meanwhile, the TEM technique has successfully identified the crystallography of the G phase and its orientation relationship with the ferrite matrix. Both methods show good agreement for the number density of the nano-sized particles.

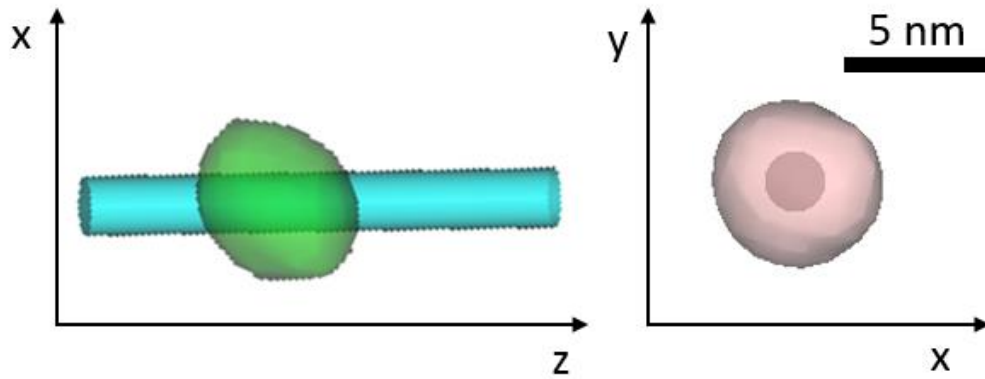


Figure 4-7. Relative position of the G phase cluster from Ni iso-surface and the cylinder.

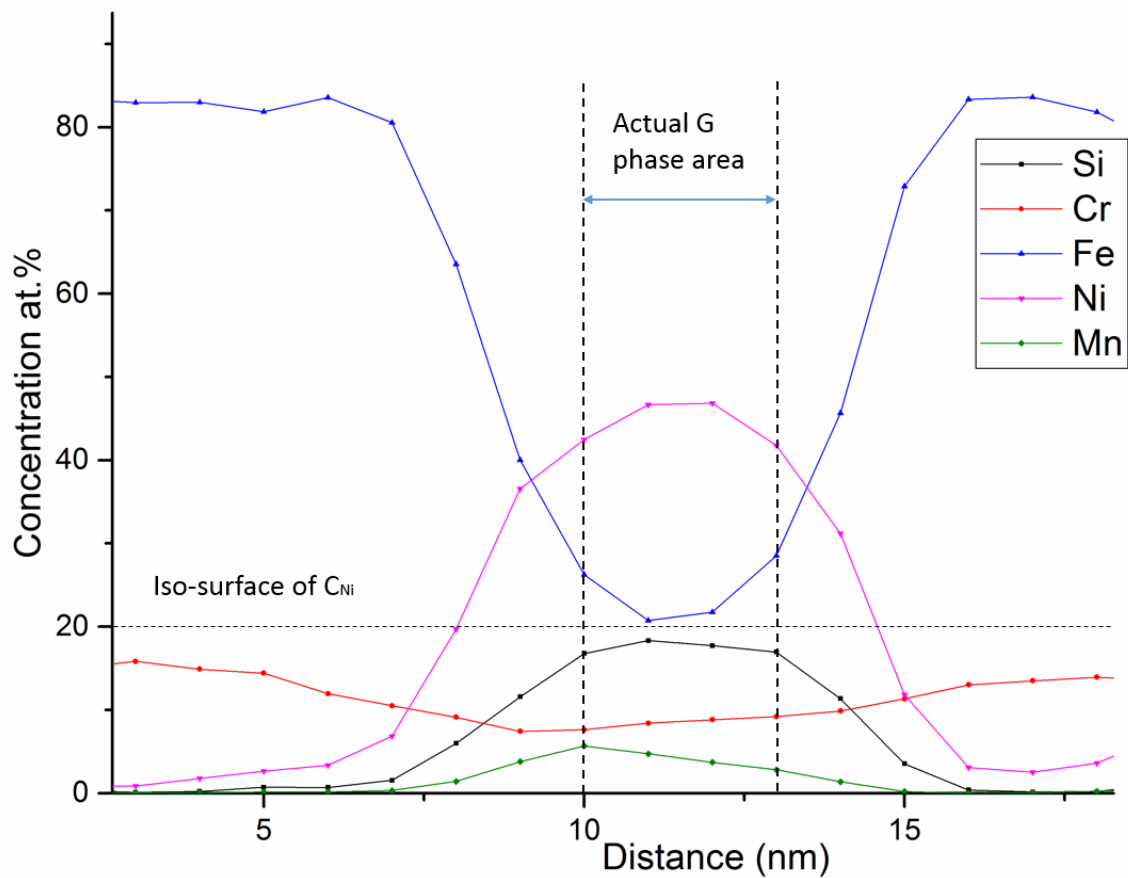


Figure 4-8. G phase precipitate in ferrite of CF-3 irradiated at 20 dpa reconstructed in IVAS.

#### 4.4 Effect of Thermal Aging and Neutron Irradiation Validation

Because of the limited irradiation sample volume and access, no metallography of the irradiated CF-3 or 308L weld is available to reflect the impact of irradiation on

macrostructure. Thus, it is impractical to describe the macro-scale impact of irradiation damage on the CASS/weld. In the meantime, based on the metallography shown in Chapter 3, long term thermal exposure has shown negligible impact on the macrostructure of CF-3 and 308L weld, such as ferrite content and morphology. No dramatic phase transformation of ferrite to austenite was observed. As no metallography is available for the neutron-irradiated samples, it is hard to tell if any macro-scale defects were induced. Future work is needed to clarify the existence of irradiation-induced segregation, void and bubble.

Irradiation is known to significantly affect the microphysics and microchemistry of the materials owing to irradiation-induced defects. The impact on density-related properties, such as free energy and diffusivity, in the long term, will be reflected in the microstructure evolution. Shown in section 4.2.2, neutron irradiation can dramatically enhance spinodal diffusion and increase the rate of the ongoing spinodal decomposition toward thermal equilibrium. Similar evidence has been reported by Miller [36], as neutron irradiation enhanced the reaction rate compared with that of thermal aging.

Such an irradiation enhanced diffusion can also be explained by Gladyshev and Kiriwara's [99] theory. Kiriwara performed experimental analysis on neutron irradiation enhanced self-diffusion in gold. His theory indicated that neutron irradiation-induced defects are not only associated with the free energy, but also with the changes in the entropy and enthalpy of the system. In the present study, it is quite obvious that the enthalpy of vacancy formation was dramatically decreased as a result neutron irradiation.

## 4.5 Mechanical Testing Analysis

### 4.5.1 Nano-indentation

The dislocation mobility in ferrite phase under low strain rates can be inferred from the nano-indentation results. Both spinodal decomposition and G phase precipitate can interact with the dislocation movement in the ferrite phase. Spinodal decomposition results in nanoscale Fe-rich  $\alpha$  phase and Cr-rich  $\alpha'$  domains. Because of the atomic size difference of Fe and Cr, a local strain field can be induced owing to the lattice misfit. Such fine-scale coherent domains interconnect with each other within the ferrite phase and are known to increase the lattice friction stress for the dislocation movement [30]. G phase precipitate can bring about precipitation hardening which plays a minor role in the ferrite phase strengthening.

Takeuchi [54] performed similar nano-indentation tests on as-received and aged weld. An ENT-1100a nano-indentation tester was used for the experiment with the maximum loading force set at 2 mN. The hardness measured by Takeuchi for as-received and aged ferrite was 4.7 GPa and 5.2 GPa, respectively. The hardness of as-received ferrite is in good agreement with the result of this study shown in Figure 3-12 at around 4.5 GPa. However, the aged ferrite in this study had a much greater hardness measurement. It turned out that the weldment in Takeuchi's experiment was thermally aged at 300 °C for 2000 h. The 308L weld tested in this study was aged at 400 °C for 2226 h. Thus, it makes sense that the higher aging temperature enabled greater extent of phase decomposition in ferrite. This, in turn can lead to greater hardening effect.

Fujii [93] also performed nano-indentation experiments on as-received and thermally aged CF8M at 400 °C for 10,000 h and 40,000 h. Both austenite and ferrite phases were examined, using an ENT 1100a The indentation with a Berkovich diamond

tip. The maximum indentation depth was kept at 300 nm. The austenite hardness measured in CF-8M for as-received and two aged conditions stayed at about 3.0 GPa. Considering the testing error, these results are in good agreement with the finding in this study of 3.5 GPa. The ferrite hardness of as-received CF-8M was at around 4.8 GPa. The hardness of aged 10,000 h and 40,000 h CF-8M ferrite were around 9.5 GPa and 10.5 GPa, respectively. The hardness measurement of ferrite/austenite in 2226 h aged 308L weld is reflective of a typical ferrite phase aged under these conditions.

Recently, Schwarm performed nano-indentation on CF-3 in as-received condition [27]. The cast block was solution treated at 1065 °C before testing. The indentation was performed using a Hysitron 900 Triboindenter with a diamond Berkovich tip with the maximum loading at 4 mN. The measured hardness for austenite and ferrite were quite close at around 5 GPa. As his report did not include the post-indentation SEM image of the tested sample, it is difficult to rationalize why the ferrite phase and the austenite phase have such close nano-hardness values. The present author suspects that, all of Schwarm's indents may have been within the austenite phase, as the Hysitron 900 tester has a low accuracy in adjusting the indentation position. Under such assumption, the indentation results in Schwarm's report were not considered in this study.

#### **4.5.2 Tensile Test**

Recently, Mburu and Schwarm [26,27,86,87] carried out similar miniature tensile tests on aged CF-3 steel to investigate the ferrite hardening phenomenon under thermal aging. The results indicated that aging had little effect on the YS of CF-3 steel but increased the UTS by close to 100 MPa. Obviously, the impact of aging on UTS of CF-3 in their study agrees quite well with that in this study. After performing APT analysis on both austenite and ferrite phases, Mburu and Schwarm found that austenite phase

stayed quite homogeneous after long-term aging, and they concluded that ferrite hardening is the primary reason for the increase in the UTS of the CF-3 miniature test. In order to fully understand the tensile test behavior of CF-3 steels, schematics of the composite for the dual phase of ferrite/austenite are illustrated in Figure 4-9.

To simplify the tensile behavior of this duplex structure, a fiber reinforced composite schematics were used. The 24% ferrite in CF-3 can be treated as reinforcement for austenite with discontinuous (chopped) distribution in random short mode. This indicates that ferrite can reinforce the austenite matrix without severely affecting the matrix deformation. Thus, the deformation process can be decomposed into the individual behavior of ferrite and austenite. The phase boundary was assumed to be negligible. To achieve this, an exaggerated stress strain curve is illustrated in Figure 4-9 to allow for a direct decoupling of the dual phase structure based on the composite model. As can be seen, austenite is more strain sensitive than ferrite. Under tensile testing at low loading rate, austenite can deform more freely and favorably than ferrites with the responsive strain distributed homogeneously within the austenite phases. For the as-cast CF-3 steel, austenite shoulders most of the deformation. In the meantime, ferrite can help increase the tensile strength with less plastic deformation. This assertion perfectly explains the dimple microvoid coalescence failure of the fracture surface for as-cast DSS [11,108]. Crack formation and growth were restrained within the austenite phase. The ferrite phase is well isolated from plastic deformation indicated by the blue dashed line in Figure 4-9.

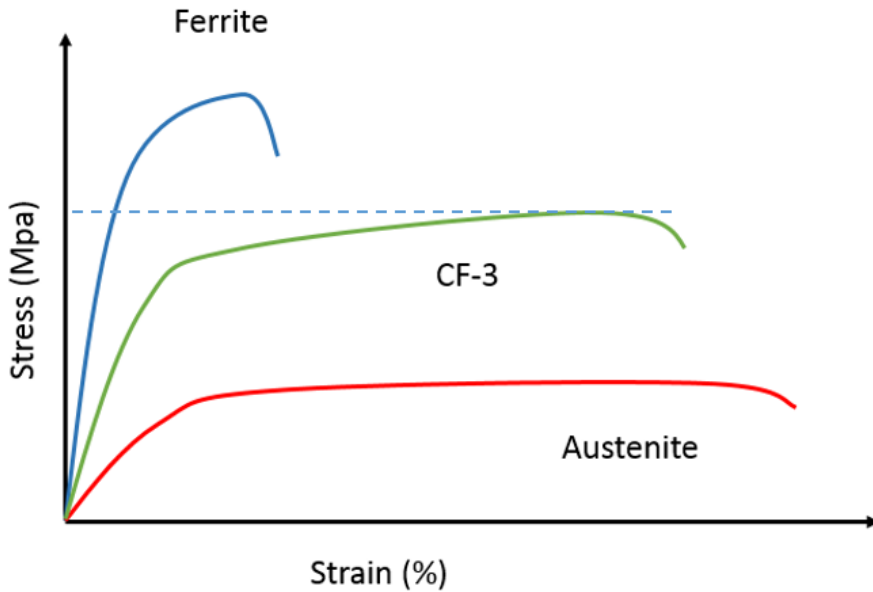


Figure 4-9. Decoupled stress strain curve of ferrite, austenite and CF-3 in exaggerated illustration. (Phase boundary not considered)

It is well known that aging at 400 °C can directly harden the ferrite phase with little impact on the austenite phase. If the phase boundary still plays the same role in the strain transfer between the austenite and ferrite, the increases in YS and UTS can be readily explained. For the increased initial stage strain hardening due to thermal aging, one possible explanation is that the phase boundary becomes less ductile after aging. This leads to more strain transferred from austenite to ferrite. Such increased strain in ferrite causes it to deform plastically and the strain hardens, resulting in rapid initial stage strain hardening.

Wang [28] recently performed similar miniature tensile tests on a DSS with ferrite content of 15 wt.% under unaged and aged conditions. The effects of thermal aging and strength enhancement trend measured in his study were quite comparable to those in this study. His result indicated that plastic deformation occurs initially in the austenite phase, regardless of the treatment condition. This conclusion is in good agreement with the illustration shown in Figure 3-12, where austenite exhibits plastic deformation earlier

than ferrite. Further deformation and fracture were correlated with the ferrite/austenite phase boundary in Wang's report. This included the stress transfer and strain redistribution between the two phases. Schwarm [26] performed FEM modeling on the elastic deformation stage of the austenite and ferrite phases in as-received CF-3 steel under applied stress. He further concluded that austenite is more prone to elastic deformation than ferrite. This makes sense, because the ferrite phase tends to be stiffer than austenite. His modeling also indicated that the strain was unevenly distributed across the bulk material during elastic deformation, especially at the austenite/ferrite phase boundaries. He further performed an EBSD examination on the surface of the tensile testing sample prior to fracture (strain = 45%). The result suggested that the ferrite and austenite phases share similar extent of plastic deformation at low strain rate for tensile testing, indicating that the phase boundary exhibits an excellent capability in coordinating the stress-strain distribution between the two phases in CF-3 during the late stage of the tensile test.

The fracture surface micrographs of the unaged and aged CF-3 in Figure 3-17 both show a predominant micro void coalescence dimple fracture, and a very small portion of river pattern can be observed in the aged tensile fracture surface. Formation of the river pattern is probably due to the involvement of the hardened ferrite phase. Chen [55] performed compact tension tests on the unaged and aged CF-3 steels. Similar dimple fracture was observed for both the unaged and aged CF-3 compact tension test fracture surfaces with no clear evidence of embrittlement.

#### **4.5.3 Micro Scratch Test**

Compared with the  $J_{IC}$  values from literature measured via J-integral and compact tension test on 308 weld by Mills and Alexander [109,110], the fracture

toughness results measured in this study are several times smaller. Initially, this was considered to be because the fracture failure mode is a combination of mode I crack opening and mode II crack sliding [71]. As for the scratch test utilized in this study, the failure mode resulted primarily from Type II sliding fracture toughness. However, after examining the morphology of all scratches, it was observed that cracks were not created in the sample surface during the tests. As shown in Figure 3-18, the bottom region of the scratch lane has no sign of any cracks with only smooth surface. This indicates that the measured tangential force is no longer a reflection of the crack formation and stable propagation. It is rather a combination of the tip/surface friction force and the forward indentation resistance. According to Akono's report [71,72], a valid fracture evolution is critical to extract the fracture toughness. Only in this case, the tangential force is a reflection of the actual crack propagation. The present author further collaborated with Anton Parr Inc. to perform scratch tests on CF-3 aged for an extremely long time. Much greater indentation pressures were applied. However, no obvious cracking at the scratch bottom was initiated. This indicates that under horizontal scratch loading, the preferential response of 308L welds is plastic deformation rather than cracking. In this case, this test method seems to be ineffective for the high fracture toughness metal in this study.

## **4.6 Structure-Property Relationship Validation on CASS/weld**

### **4.6.1 Spinodal Decomposition Strengthening**

The results of nano-indentation, tensile test and micro scratch test all indicate that long-term aging exposure would harden the ferrite phase and decrease the overall ductility of the material. The austenite phase is relatively stable under low temperature thermal aging impact based on the phase diagram. Thus, it has limited impact on the

mechanical property degradation of CASS/weld. Such correlation has been conclusively validated. The relationship between ferrite embrittlement and its phase decomposition has been reported, but quite inconclusive, especially the underneath strengthening mechanism.

Weng [81] reported to have discovered twinning in the ferrite phase of DSS near the fracture surface due to thermal aging under external impact loading. Twinning in B.C.C. typically occurs via  $\{112\}$  planes and occurs at low temperature and high strain rate [111]. No twinning was observed in the present study by TEM or stress-strain curve. However, Weng's report agrees quite well with the observation of Cortie and Marcinkowski's [30,112] on hardness indentation impressions of Fe-Cr binary alloys, where the ferrite grain size was quite large at 50-100  $\mu\text{m}$ . The observed twinning deformations all occurred under high strain. In comparison, the loading rate in this study was quite small. Even though the underneath mechanism is still unknown, it is suspected that aging-induced spinodal decomposition has a greater impact on lattice friction energy as a result of chemical strengthening. Such strengthening has much higher impact on resolved shear stress for dislocation slip than twinning. Thus, for fully aged ferrite, a shift in plastic deformation mechanism from slip to twinning can be observed. Meyers [113] performed constitutive analysis over the onset of twinning in B.C.C. metals, especially in Fe, and found that the grain size played a major role in the twinning initiation in Fe grains. Such a description corresponds perfectly with findings in this study. The average phase sizes of ferrite in CF-3 steels and 308L welds were less than 10  $\mu\text{m}$  and 1  $\mu\text{m}$ , respectively. It is quite impractical for dislocation pile-up induced

stress concentration to accumulate sufficiently to exceed the critical twinning stress. Thus, it makes sense that no twinning was observed in this study.

Hsieh's [114] group performed in-situ TEM investigation on aged DSS ferrite. He further concluded that the dislocation mobility was hindered because of thermal aging-related spinodal decomposition. As Cahn and Kato [115,116] reported, the amplitude and wavelength of Cr composition modulation can induce periodic variation of the elastic modulus in Fe-Cr binary alloys. Kato further calculated the amount of lattice misfit hardening and modulus hardening. The calculated results agreed quite well with experimental measurement.

Little is known concerning the scale of the spinodal coherency strain field, even though it has been widely mentioned. Some researchers [81] propose isotropic distribution between the Cr-rich zone and Cr-depleted matrix. However, Nichol [105] concluded that the modulated structure yielded better contrast along the  $\langle 001 \rangle$  direction. One major reason is the small atomic size difference between Fe and Cr [7]. Thus, Weng [81] argued that the elastic coherence strain at the indiscernible interfaces is negligible. However, the measurement of the spinodal strain by Li [11] showed clear existence of an interconnected strain field in his geometric phase analysis on aged ferrite. Even though a strain field at a single  $\alpha/\alpha'$  domain pair can be small, such strain field distribution is not uniform within the ferrite phase. It is suspected that the accumulated effect on the strain field can be quite large, exceeding 30% in both tensile and compressive strain. The distance of such high strain regions is about 20 nm. Although further validation of such strain field measurement is needed, Li's results still help to explain how the accumulated strain field plays an important role in the

strengthening of the ferrite phase. The interaction between the dislocation strain field and the spinodal strain field can make it much more difficult for dislocation to move, thus enhancing the hardness and strength of the ferrite phase. The reason for such non-uniformity is still unknown. Upon spinodal decomposition, Ni is known to partition to  $\alpha$  phase due to its low solubility in  $\alpha'$  phase [117,118], while Si is known to partition preferentially to  $\alpha'$  phase. Such behavior can be a potential reason for the strain distribution non-uniformity.

#### **4.6.2 Particle Strengthening by G Phase**

G phase is also known to play a minor role in ferrite strengthening. Mburu [86] performed mechanical property testing on aged CF-3 with G phase present and on CF-8 with no G phase precipitation observed. The changes in mechanical property were very similar. However, a number of other factors can affect both the microstructure and mechanical properties including chemical composition and the scale of spinodal decomposition in ferrite. Thus, it is actually quite difficult to tell if G phase played a role or not, as it normally emerges synergistically with spinodal decomposition in ferrite of duplex structured stainless steel alloys. Moreover, it is quite difficult to decouple the impact of both phases. Yamada [119] performed aging experiments at 400 °C to introduce spinodal decomposition and G phase in ferrite. Aged samples were then reheated at 550 °C to eliminate the spinodal decomposition but not the G phase. The change in hardness showed that G phase was responsible for the second stage ferrite hardening behavior. Yamada's result helps to confirm that G phase does contribute to the ferrite phase hardening. Theoretically, it is possible to determine the impact of G phase based on its volume fraction, average radius and strengthening mechanism. For the aged CF-3 measured via APT G phase reconstruction, the volume fraction of G

phase is less than 1%. In comparison, the spinodal decomposition morphology occurs throughout the ferrite phase. In this manner, it is safe to conclude that G phase played an insignificant role in the ferrite strengthening.

#### **4.6.3 Other Strengthening Mechanism**

This author recently reviewed the YS and hardness of Fe-Cr binary tested at room temperature by Maykuth and Jaffee [120] shown in Figure 4-10. The plot indicates that a very small portion of Fe in the Cr matrix can have a significant impact on its strength, with peak Fe content at 25 at.%. If this strengthening phenomenon were true when the Cr-rich zone size was a few nanometers, the spinodal decomposition could be explained accordingly. For CF-3 with 25 at.% of Cr in the ferrite phase, as ferrite decomposes spinodally, the summation of the nominal hardness of the Cr rich zone and matrix with less Cr will always have greater strength value than the homogeneous state, because the strength vs composition curve near 25 at.% faces downward. Unfortunately, the reason for this phenomenon of Fe strengthening on the Cr matrix is still unknown. It is suspected that a greater lattice friction force is needed for dislocation to move through the Cr-rich zone regardless of its size.

To further quantify the possible strengthening magnitude, the following assumptions and discussions were made. Overall, previous efforts trying to correlate hardness or YS with wavelength or amplitude seem to be quite inconclusive and lacking a detailed strengthening mechanism. Thus, it is quite reasonable to assume that, after long-term thermal exposure, ferrite decomposes into the Cr-depleted matrix and the Cr-rich zone dispersions distanced by wavelength  $\lambda$ . Such a simplification makes it possible to apply particle strengthening mechanisms to the system.

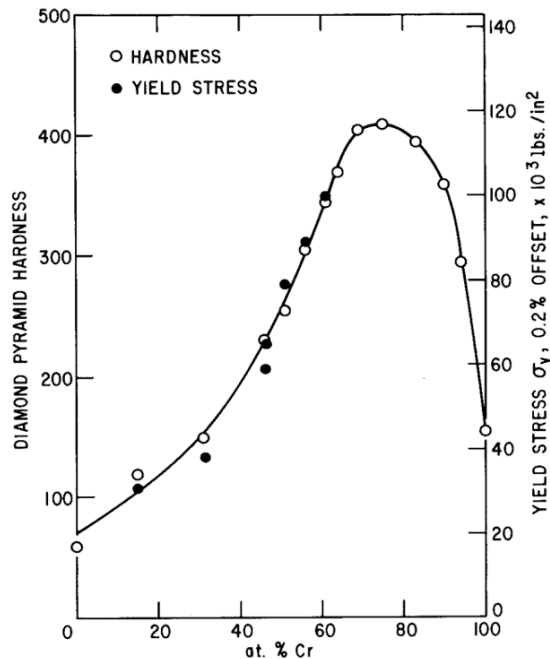


Figure 4-10. Strength and hardness of unaged Fe-Cr alloys. (Source: Ref. [112])

To correlate the result of tensile tests on CF-3 steels and their microstructure evolution, properly only the resolved shear stress quantification for pure slip should be considered and compare it with the 0.2% YS of the ferrite phase based on the tensile test. For the unaged condition, the value from Figure 4-10 with Cr content of 25% are employed with value of 35,000 psi = 241 MPa. Strengthening mechanisms such as solid solution, Hall-Petch effect and G phase clustering, were not considered for simplification. Under the composite model of CF-3, with ferrite content of 24%, the YS for austenite is 228 MPa. Considering that austenite hardness stays relatively constant, its YS can be set as constant too. The corresponding strengthening in ferrite can be calculated accordingly to be 403 MPa = 58,000 psi based on the value measured in section 3.3.2.

Before proceeding to calculate the resolved shear stress for pure slip mode in aged ferrite of CF-3, it is helpful to consider the Orowan bending theory. Although it is

highly impossible for such occurrence to be true, it helps to clarify if the Cr-rich zone is deformable or not. The stress needed for dislocation to loop around the 3 nm Cr-rich zone to critical radius can be expressed in Eq. 4-4.

$$\tau = \frac{2\alpha Gb}{\lambda - d} \quad (4-4)$$

where  $\alpha$  is a structure coefficient at 0.5 for B.C.C.,  $G$  is the shear modulus of the material at 77 GPa and  $b$  is the burger's vector at 0.248 nm. With the value of wavelength  $\lambda$  and zone size  $d$  in this study, the estimated resolved shear stress  $\tau = 4$  GPa. Such a value is impractically larger than the observed value of 403 MPa. Thus, there is no doubt that dislocation can be better estimated to cut through the Cr rich zone.

Based on Marcinkowski's [112] evaluation of aged Fe-Cr binary alloys, the mechanism of friction stress augmentation due to the generation of the Cr-rich zone was applied. He proposed that the higher Cr-rich zone yields greater lattice friction force maximized at 75 at.% Cr, thus inhibiting the dislocation slip movement. The resolved shear stress for slip based on this mechanism accounted for around 50% of the observed YS in his report. Similarly, owing to thermal aging, the ferrite phase was simplified to decompose into the 12 at.% Cr matrix and the Cr-rich zone dispersions of 45 at.% Cr based on Figure 3-6. The volume fraction of the Cr-rich zone was estimated from the lever law to be 39.4%. The total frictional force  $F_T$  acting on a unit length of a perfectly rigid dislocation is given by Eq. 4-5.

$$F_T = \tau_M b_M (1 - f_{Cr}) + \tau_{Cr} b_{Cr} f_{Cr} = \tau_T b \quad (4-5)$$

where  $\tau_{Cr}$  and  $\tau_M$  refer to the corresponding shear stresses acting on the dislocation of the Cr-rich zone and matrix, respectively and  $f_{Cr}$  denotes the volume fraction of the Cr

rich zone. Assuming that  $b_{Cr} = b_M = b$ , the total shearing stress of slip can be expressed by Eq. 4-6.

$$\tau_T = \tau_M + (\tau_{Cr} - \tau_M)f_{Cr} \quad (4-6)$$

Estimation based on Figure 4-10 gives  $\tau_M$  at 20,000 psi and  $\tau_{Cr}$  at 62,000 psi. The calculated total shearing stress is  $\tau_T = 36,500$  psi = 252 MPa, which is approximately 63% of the measured value. Compared with the original unaged ferrite YS value, this is only a slight increase.

Other strengthening mechanisms, such as modulus strengthening, chemical strengthening and Williams' [121] modified Mott and Nabarro theory on coherency strain hardening, can all contribute to the ferrite hardening. Under the Cr-rich zone dispersion assumption, the estimated modulus strengthening and chemical strengthening have quite limited impact on strengthening magnitude. Williams [121] considered the interaction between the hydrostatic stress field of edge dislocation and precipitate. The estimated critical shear stress was found to be the same order magnitude as  $\tau_T$ . However, Williams' theory is more applicable to precipitates with very small volume fraction.

In the meantime, Kato [118] extended the study of lattice misfit hardening and modulus strengthening based on the modulated structure of Cr concentration fluctuation rather than Cr-rich zone. The incremental critical resolved shear stress  $\Delta\sigma_y$  due to the spinodal decomposition in B.C.C. Fe-Cr alloys is expressed as Eq. 4-7.

$$\Delta\sigma_y = 0.5A\eta Y + 0.65\Delta Gb/\lambda \quad (4-7)$$

$$Y = E/(1 - \nu) \quad (4-8)$$

where the former term denotes the magnitude of misfit hardening and the latter term indicates the modulus strengthening extents,  $A$  is an amplitude factor,  $\eta$  is the dimensionless variation of the lattice constant  $a$  with respect to the concentration of Cr, and  $Y$  is expressed by the elastic moduli. For isotropic elasticity,  $Y$  is given by Eq. 4-8, where  $E$  is the elastic modulus and  $\nu$  is the Poisson's ratio (0.3 for steel),  $\Delta G$  represents the shear modulus difference of the Fe-rich and Cr-rich zones,  $b$  is the burger's vector of 0.248 nm, and  $\lambda$  is the wavelength of the spinodal modulated structure. In this study, the  $\lambda$  value obtained from RDF is used. Substituting all values leads to an incremental  $\Delta\sigma_y$  of almost 360 MPa. This is not considering the Taylor's factor of two for B.C.C. alloys [114]. As can be seen, the YS value based on Kato's model is at least 120% overestimated. The main reason for it that, modulus strengthening is proportional to  $1/\lambda$  in Kato's theory, which is way too linear, thus causing unexpected overestimation when  $\lambda$  is only a few nanometers. More future work is needed in this area, to possibly combine the theories of Marcinkowski and Kato to obtain a more accurate strengthening mechanism.

#### **4.6.4 Compact Tension Test and Impact Test of CF-3**

Because of the limitation of the micro scratch test on the 308L weldment, no successful extraction of the fracture toughness was achieved in this study. However, the  $\frac{1}{4}$  T compact tension test was performed on the CF-3 by Chen at ANL using specimens from the same cast slab as those used in this study. The details of these tests can be found in the referenced conference paper [88]. Compared with unaged CF-3, aging at 400 °C for 10,000 h dramatically reduced the  $J_Q$  value from 320 kJ/m<sup>2</sup> to 170 kJ/m<sup>2</sup>. Subsequent fractography investigation was also performed [55]. As the microstructure of austenite was reported to show little change under thermal aging, the fracture

toughness decrease due to thermal aging can be purely attributed to the spinodal decomposition of ferrite phase. The synergistic effect of thermal aging and neutron irradiation on the fracture toughness decrease was also confirmed. The extra amount of G phase precipitation in ferrite can be one reason for the decrease. Another reason can be the irradiation-hardened austenite reported by Takeuchi [43,54]. The amount of decrease in fracture toughness due to the low dose neutron irradiation is much larger compared to that measured on stainless steel weld by Tobita [82]. As no detailed microstructure graphs were presented in his report, the reason for this discrepancy is still unknown.

The full-size Charpy V-notch impact energy changes of CF-3 due to thermal aging was studied by Chopra [17]. Specimens tested were the same as the CF-3 steels used in this study with heat number 69. The impact test used a much greater strain rate compared with that in the compact tension and tensile test. The effect of ferrite embrittlement on the fractography of CF-3 aged at 400 °C for 10,000 h clearly revealed the trend of brittle cleavage failure throughout the fracture surface. Crack initiation in ferrite was assumed to be caused by either dislocation pile-ups or twinning intersections. The twinning mechanism could be supported by Weng's [81] report. Meanwhile, the dislocation pile-up owing to spinodal decomposition constraints can be reinforced by Li and Hsieh's [11,114] findings. This author tends to agree with the dislocation pile-up mechanism.

## CHAPTER 5 CONCLUSIONS

In this study, CASS/welds were investigated under varied aging and irradiation treatment. Systematic metallurgical, metallographic, crystallographic and microstructural characterization and analysis were carried out by optical microscopy, SEM, TEM and APT examination. The chemical composition was examined by APT. The corresponding mechanical properties were evaluated by tensile test, nano-hardness test and micro scratch test.

The macrostructural transformation texture of dendritic austenite and duplexed with ferrite subgrains was successfully identified. It was assumed that the austenite/ferrite duplex played the major role in determining the mechanical properties of the steel, rather than the dendrite grains. A structure-property relationship on CASS/welds was explored. The ferrite phase microstructure evolution under aging and irradiation was characterized using APT. Part of the APT reconstruction results were further validated using TEM characterization with respect of spinodal decomposition and G phase precipitation. The tensile strength of CF-3 and hardness of weldment under varied aging conditions were successfully characterized by sub-sized tensile testing and nano-indentation.

Based on the characterization and subsequent analysis, the following contributions have been achieved:

A synergistic effect of neutron irradiation with thermal aging on the ferrite in CF-3 has been confirmed. The enhancement in both spinodal decomposition and G phase precipitation was quantified for the first time. The neutron irradiation-induced G phase precipitation is more active than spinodal decomposition.

Response of ferrite to high dose neutron irradiation was investigated for the first time. Irradiation dose ranges, including threshold and the saturation dose levels for spinodal decomposition, were established.

Wavelength growth of spinodal decomposition vs neutron irradiation in ferrite of CF-3 was observed. The difference from the conventional wavelength migration under thermal aging was explained by three-stages evolution of Cr clustering.

The results obtained from this research can further help push forward the CASS/weld degradation under LWR working environment. The high dose neutron irradiation results helped provide valuable data points for the establishment of full range neutron irradiation response of ferrite decomposition. The micro scratch test itself set a good example of fracture toughness extraction and interpretation. The volume fraction variation of G phase under neutron irradiation was proposed and can act as one of the key parameters for aging degradation assessment.

The new methods and theories developed this thesis include:

- First, the methodology of proxigram for Cr concentration profile extraction was developed and interpreted by the author. The method was capable of determining the wavelength and amplitude of spinodal decomposition, in good agreement with frequency distribution and RDF results.
- Second, improvement on the RDF calculation was successfully achieved by extending its range from 10 nm to 25 nm with additional Matlab code. This modification perfectly solved the limitation of the IVAS built-in algorithm.
- Third, the extent of spinodal decomposition in ferrite of CASS/weld was quantified based on frequency distribution. By judging from the peak shift saturation, the equilibrium concentration of the Cr-depleted  $\alpha$  phase was accurately predicted.
- Fourth, specific milling steps were developed for the atom probe tip preparation on the irradiated cast and weld samples. The irradiated samples tend to be very fragile. The designed milling steps can help make high quality APT tips with large data set extraction. For features such as G phase clustering, a larger data set can allow for more accurate size and density quantification.

- Fifth, a simple method for estimating irradiation enhanced diffusion was achieved based on the aged and irradiated CF-3 individually. This estimation is within the acceptance of the enhancement rate. The result can act as a benchmark for future estimation and validation.
- Sixth, nano-scale features, such as Cr spinodal decomposition and G phase clusters, identified from APT reconstruction were successfully correlated with the results from TEM. The good agreement of APT and TEM data indicates that data extracted from APT are quite accurate in spinodal decomposition wavelength and G phase precipitation number density prediction.

Takeuchi [54,122] performed APT examination on the 308L weldment under neutron irradiation conditions and observed Si rich clusters in austenite phase. Similar characterizations are needed as future work on the irradiated austenite phase in both CF-3 and 308L to clarify this phenomenon.

## APPENDIX A ATOM PROBE BASICS AND TIP FABRICATION

There are two data acquisition modes in LEAP, the voltage mode and laser mode. Conductive materials such as stainless steels can be analyzed well in the voltage mode. The alignment of needle specimen to the electrode is achieved visually after sample loading. Laser mode is applicable to any materials, such as semiconductors and ceramics. The alignment of specimen apex to the laser takes more steps including pre-alignment, manual alignment and fine alignment of laser position and focus. For CASS/weld tip, both modes work fine. To maximize the data collection on those irradiated specimens that are prone to fracture, laser mode is preferred with detection rate kept between 0.1% - 0.5%. Sometimes the voltage mode is used as well. The samples are placed in a high-vacuum chamber with a cooling system in order to meet the strict working environment in LEAP. The pressure is usually kept extremely low at  $10^{-11}$  torr. The temperature is dependent on the analyzed materials. In the case of stainless steel alloys, the temperature is set between 20 K and 80 K to achieve similar evaporation rates for both Fe and Cr atoms. In the present work, the temperature was set to be 55 K. Data collection will stop once the sample tip fractures or the voltage reached the limit of 9 kV. Most of the time the tip fractures owing to the stress on the tip caused by the local electric field. Any small defects in the tip can cause a fracture event. In case of a good run when tip did not fracture, the applied voltage will keep ramping up. When the voltage becomes too high, the local electrode starts to evaporate and contaminates. What's more, high voltage can lead to catastrophic tip fractures, which could damage the local electrode. Thus, data collection automatically stopped when voltage reached a set value.

A good quality tip is key to the success of the atom probe experiment. Typically large data is not required for spinodal decomposition analysis. On average, 10 millions of ions is sufficient to reveal the features such as the frequency distribution and RDF computation. However, for cluster analysis, the accuracy in size and density calculation decreases significantly when sample data size is too small. Thus, for those atom probe experiments on CF-3 and 308 weld, large data set with approximately 20 million ions is highly needed.

Tips that run good in LEAP with more than 20 million ions collection rely on several different factors including the tip geometry, material, treatment condition and the LEAP running environment. For stainless steel, the average data set obtained is around 10 million. Depending on the treatment condition, as cast homogeneous CF-3 tips can reach 20 million before fracture. In comparison, the neutron irradiated CF-3 tips tend to fracture more easily under high voltage due to the irradiation induced defects. In general, a clean tip pillar with sharp tip top and smooth tapering transition, followed with near straight body is the ideal tip geometry. The detailed steps of the tip annular milling are summarized in Table A-1. The low kV step at 5 kV is the critical step. The key this step is to watch the tip shrinking and sharpening. The major purpose is to fully sputtering out the Pt layer without causing too much tip thinning. A sequence of FIB-SEM images demonstrating the basic procedures are illustrated in Figure A-1.

Starting from Figure A-1 a), ferrite with length greater than 15  $\mu\text{m}$  is ideal for Pt deposition. For a maximum of 6 APT tips, a cantilever with 15  $\mu\text{m}$  is typically needed. After two steps of trench milling and a cantilever lift-out using the FIB micromanipulator, the triangle coupon of ferrite was further transferred onto the Si tip holder. Shown in

Figure A-1 b) and c), the part of the ferrite coupon was welded onto the Si tip holder imaged using I beam (Figure A-1 b)) and E beam (Figure A-1 c)) mode with stage tilt at 0 degree. The dark box indicates the ion-milling region to separate the tip with the ferrite coupon. Figure A-1 d) illustrates the annular milling using high energy Ga<sup>+</sup> ion to obtain the ideal cylinder shape of the tip finished with outer diameter of 350 nm. Figure A-1 e) shows a good tip finished with outer diameter at 150 nm by the 5 kV Ga<sup>+</sup> ion. To reduce the Ga<sup>+</sup> ion sputtering damage of the tip surface, a cleaning step at 2 kV is needed as the final step.

Table A-1. LEAP Tip Annular Milling Steps

Current (30 kV)	OD(um)	ID(um)	Z
3 nA	6.0	4.00	0.3 μm
1 nA	4.5	2.00	0.3 μm
0.3 nA	4.0	1.5	0.2 μm
0.3 nA	3.5	1.0	0.2 μm
0.1 nA	3.0	0.75	0.2 μm (measure)
0.1 nA	2.5	0.50	0.2 μm(measure)
30 pA	2.0	0.30	0.2 μm(measure)
30 pA	1.5	0.25	0.2 μm(measure)
5 kV-48 pA	-	0	Watch the tips change shape
2 kV-27 pA	-	0	1 min would work the best

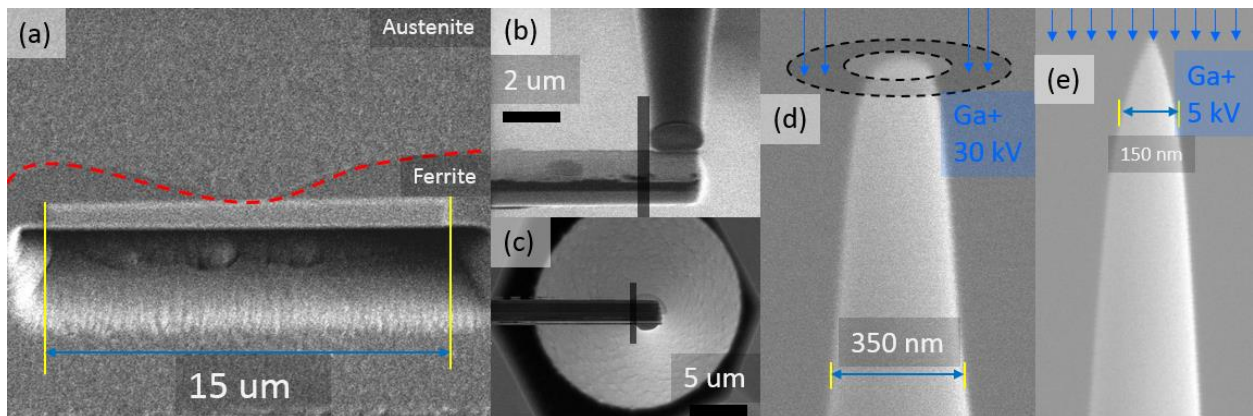


Figure A-1. LEAP Tip fabrication steps in FIB-SEM procedure.

## APPENDIX B MICRO SCRATCH FRACTURE TOUGHNESS

The stress intensity factor defines the status of fracture when a crack is initiated. With the help of stress concentration factor, the stress intensity factor is defined as follows by Irwin-Griffith equation:

$$K_c = Y\sigma_f\sqrt{\pi a} \quad (\text{B-1})$$

where  $Y$  is the geometry factor,  $\sigma_f$  denotes the applied stress.  $a$  is the crack length.  $K$  increases with the increase of crack length grows. When the crack gets great enough after initiation with the increase of external load, its rapid propagation becomes inevitable. This value of stress intensity factor where crack starts to be unstable and propagate rapidly is typically termed as fracture toughness,  $K_c$ .

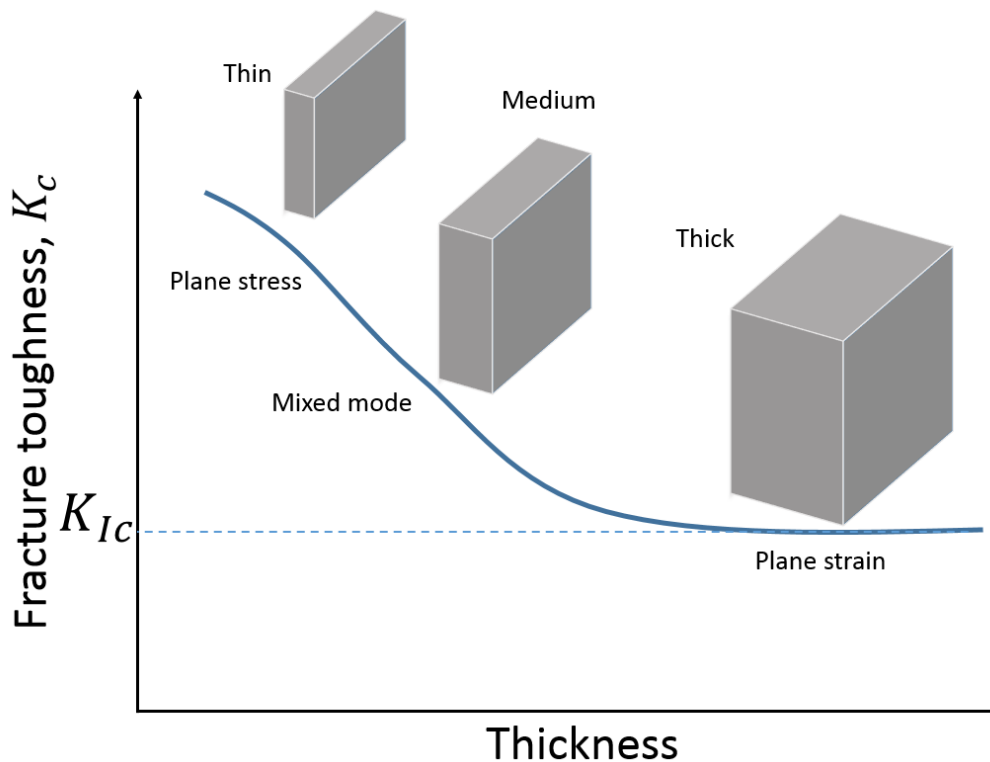


Figure B-1. Relationship of fracture toughness and sample thickness.

$K_c$  is dependent on the material geometry. Shown in Figure B-1, with the increase of the sample thickness, the  $K_c$ , or the critical stress intensity factor will initially increase linearly with increase of sample thickness then decrease. Further increase of the thickness will lead to the  $K_c$  reaching a lower saturation level. This value of  $K_c$  is determined as the property of the material, regardless of the testing sample dimension, geometry, testing method, as mode I plane strain fracture toughness  $K_{Ic}$ .

Recently, researchers from Massachusetts Institute of Technology developed a new testing method of measuring the fracture toughness via micro scratch test. During the test, a scratch is produced in the sample using a typical indenter tip with vertical load and a constant speed. The tangential force, penetration depth, and vertical load are measured. With the vertical load increases, both tangential force and penetration depth increase gradually.

$$K_c = \frac{F_T}{\sqrt{(2pA)}} \quad (\text{B-2})$$

For linear elastic fracture mechanics model, a relationship between the tangential force and the penetration depth is analyzed shown in Eq. B-2 where both the perimeter,  $p$  and contact area  $A$  are a function of penetration depth  $d$ . To further quantify the relationship between the tangential force  $F_T$  and penetration depth  $d$ , the value of  $F_T$  vs  $d^{3/2}$  is plotted [72]. It turned out that a linear relationship between the two can be revealed when the penetration distance is greater than half of its max. After further mathematical formulation, the slope of the  $F_T$  vs  $d^{3/2}$  is correlated with the fracture toughness of the material. Both shared the same unit of  $\text{Pa(m)}^{1/2}$ . Further research conducted by the same group proposed the perimeter  $p$ , and the indenter projection area alongside the sliding direction  $A$ , to describe the impact of the indenter tip

geometry. The product of the two parameters with a factor of 2, denoted as  $2pA$  is the probe shape function  $f$ . Further derivation proved that the probe shape function is proportional to the value of  $d^3$ . By plotting the tangential force,  $F_T$  vs the square root of the probe shape function  $f$ , a linear relationship can be observed. In addition, the slope of the plot was further proved to be the fracture toughness  $K_{IC}$  of the material.

## APPENDIX C THE PHYSICS OF NEUTRON IRRADIATION DAMAGE

The fundamental physics of a single neutron irradiation with the cascading defects generation is illustrated in Figure C-1. The incident neutron collides with the lattice atom, as the primary knock-on atoms (PKAs) followed with kinetic energy transfer. Those PKAs then collide with more nucleus that are in the passage of the PKA. This process generates more point defects. The whole process happened within extremely short amount of time in about  $10^{-11}$  s [52]. As the energy of the incident neutron varies, the density of the induced point defects also changes. Some of irradiation induced Frenkel pairs will recombine through defects reaction due to thermal healing. The process of radiation damage event can be summarized as the formation point defects and defect clusters. The irradiation damage rate is typically estimated from SRIM calculation based on the K-P model. For steel material, pure iron with density of  $7.8 \text{ g/cm}^3$  is used for the SRIM calculation alongside with the neutron irradiation energy profile. Theoretically, the neutron irradiation damage is given by the displacement rate shown in Eq. C-1 [52].

$$R = \int N\phi(E_i)\sigma_D(E_i)dE_i \quad (\text{C-1})$$

where the displacement rate  $R$  has the unit of number of displacements per unit volume per unit time,  $N$  is the number density of the material,  $\phi$  denotes the neutron flux and  $\sigma_D$  is the displacement cross section. By utilizing the K-P model and several other neutron irradiation physics assumptions,  $R$  can be estimated through Eq. C-2.[52]

$$R = N\sigma_s(\gamma\bar{E}_i/4E_d)\Phi \quad (\text{C-2})$$

where  $\sigma_s$  is the scattering cross section,  $\bar{E}_i$  is the average neutron irradiation energy and  $\Phi$  denotes the total neutron flux above  $E_d/\lambda$ .

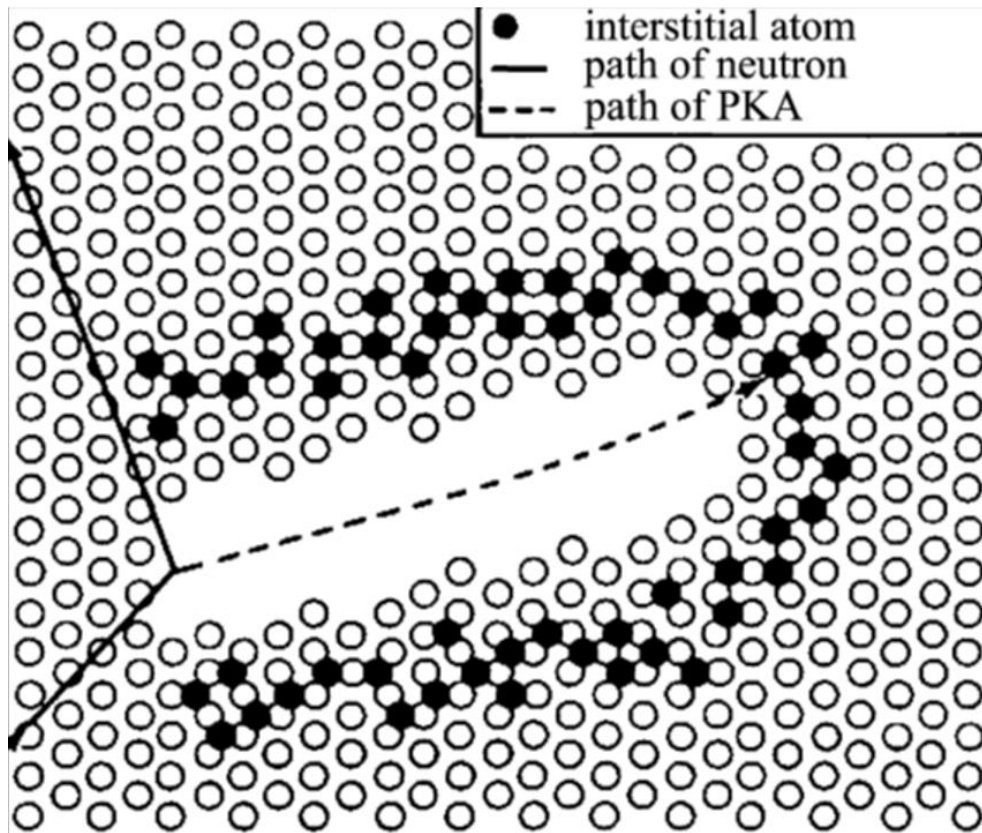


Figure C-1. Schematic of neutron irradiation damage in solid. (Source: Ref. [123])

The schematic shown in Figure C-1 is a B.C.C. ferrite crystal with  $\{111\}$  orientation. The high-energy incident neutron strikes the Fe atom via an inelastic scattering process, transferring a portion of its energy to the Fe atom, or primary knockon atom (PKA). The dash arrow indicates the PKA's trajectory. As the PKA moves through the lattice, Fe atoms in its path are displaced to nearby interstitial sites. Such an effect leaves a long vacancy pathway surrounded by the displaced interstitials, known as a cascading effect. Researcher [52] has estimated the amount of Fe atoms being displaced in a single PKA cascading event. For a neutron energy of 0.5 MeV, approximately 350 Fe atoms were displaced per neutron. For a neutron irradiation

damage rate of  $10^{-6}$  dpa/s, its equivalent effect is that each Fe atom will be displaced from its lattice position once every 12 days ( $10^6$  seconds).

APPENDIX D  
SUPPLEMENT RESULTS

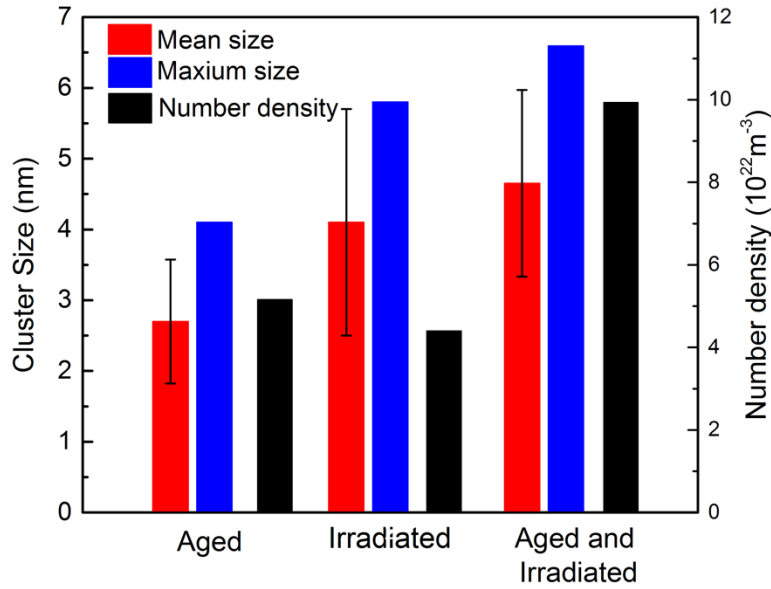


Figure D-1. Maximum size, mean size and volumetric number density of G-phase precipitates of CF-3.

The data of G phase identified in CF-3 in APT reconstruction has already been summarized in the table 3-3. The mean size of the G phase clusters with error bar is shown in Figure D-1.



Figure D-2. As-weld 308L OM image of the base metal and fusion zone.

As revealed in Figure 4-2, the columnar dendrite, heat affected zone and base metal are illustrated in Figure D-2. Some of the welding defects are labelled as those black irregular void areas.

## LIST OF REFERENCES

- [1] P. Marshall, Austenitic stainless steels: microstructure and mechanical properties, Springer Science & Business Media, 1984.
- [2] J.L. Dossett, H.E. Boyer, Practical heat treating, Asm International, 2006.
- [3] W.D. Callister, D.G. Rethwisch, Materials science and engineering, John Wiley & Sons NY, 2011.
- [4] B.L. Bramfitt, Structure Property relationships in irons and steels., Mater. Park OH ASM Int. 1998. (1998) 153–173.
- [5] H. Okamoto, L. Kacprzak, P.R. Subramanian, Binary alloy phase diagrams, ASM international, 1996.
- [6] M. Maalekian, The effects of alloying elements on steels (I), Christ. Doppler Lab. Early Stages Precip. 23 (2007) 221–230.
- [7] F. Danoix, P. Auger, D. Blavette, Hardening of aged duplex stainless steels by spinodal decomposition, Microsc. Microanal. 10 (2004) 349–354.
- [8] I.V. Vernyhora, V.A. Tatarenko, S.M. Bokoch, Thermodynamics of fcc-Ni–Fe Alloys in a Static Applied Magnetic Field, ISRN Thermodyn. 2012 (2012).
- [9] P.J. Grobner, W.C. Hagel, The effect of molybdenum on high-temperature properties of 9 pct Cr steels, Metall. Trans. A. 11 (1980) 633–642.
- [10] F.C. Campbell, Structural composite materials, ASM international, 2010.
- [11] S. Li, Y. Wang, X. Wang, Effects of ferrite content on the mechanical properties of thermal aged duplex stainless steels, Mater. Sci. Eng. A. 625 (2015) 186–193.
- [12] J.M. Vitek, S.A. David, Solidification and aging behavior of Types 308 and 308CRE stainless steel welds, Oak Ridge National Lab., TN, 1984.
- [13] S. Bonnet, J. Bourgoïn, J. Champredonde, D. Guttman, M. Guttman, Relationship between evolution of mechanical properties of various cast duplex stainless steels and metallurgical and aging parameters: outline of current EDF programmes, Mater. Sci. Technol. 6 (1990) 221–229.
- [14] O. Kamiya, K. Kumagai, T. Futami, Effect of ferrite morphology on fracture mode of stainless steel weld metal, Weld. Int. 8 (1994) 798–803.
- [15] L. Karlsson, H. akan Arcini, E.-L. Bergquist, J. Weidow, J. Börjesson, Effects of alloying concepts on ferrite morphology and toughness of lean duplex stainless steel weld metals, Weld. World. 54 (2010) R350–R359.

- [16] O.K. Chopra, H.M. Chung, Aging of cast duplex stainless steels in LWR systems, *Nucl. Eng. Des.* 89 (1985) 305–318.
- [17] O.K. Chopra, A. Sather, Initial assessment of the mechanisms and significance of low-temperature embrittlement of cast stainless steels in LWR systems, Nuclear Regulatory Commission, Washington, DC (USA). Div. of Engineering; Argonne National Lab., IL (USA), 1990.
- [18] O.K. Chopra, W.J. Shack, others, Mechanical Properties of thermally aged cast stainless steels from shippingport reactor components, Citeseer, 1995.
- [19] H.M. Chung, T.R. Leax, Embrittlement of laboratory and reactor aged CF3, CF8, and CF8M duplex stainless steels, *Mater. Sci. Technol.* 6 (1990) 249–262.
- [20] S.J. Zinkle, J.T. Busby, Structural materials for fission & fusion energy, *Mater. Today.* 12 (2009) 12–19.
- [21] S.J. Zinkle, G.S. Was, Materials challenges in nuclear energy, *Acta Mater.* 61 (2013) 735–758.
- [22] D. Testa, A. Kunkle, The Westinghouse pressurized water reactor nuclear power plant, Westinghouse Electr. Corp. Water React. Div. (1984).
- [23] O.K. Chopra, G. Ayrault, Aging degradation of cast stainless steel: status and program, *Nucl. Eng. Des.* 86 (1985) 69–77.
- [24] M.K. Miller, J. Bentley, S.S. Brenner, J.A. Spitznagel, Long term thermal aging of type CF 8 stainless steel, *J. Phys. Colloq.* 45 (1984) C9–385.
- [25] P.H. Pumphrey, K.N. Akhurst, Aging kinetics of CF3 cast stainless steel in temperature range 300–400 C, *Mater. Sci. Technol.* 6 (1990) 211–220.
- [26] S.C. Schwarm, S. Mburu, R.P. Kolli, D.E. Perea, J. Liu, S. Ankem, Mechanical and Microstructural Effects of Thermal Aging on Cast Duplex Stainless Steels by Experiment and Finite Element Method, in: *Mech. Creep Behav. Adv. Mater.*, Springer, 2017: pp. 253–262.
- [27] S.C. Schwarm, R.P. Kolli, E. Aydogan, S. Mburu, S. Ankem, Characterization of phase properties and deformation in ferritic-austenitic duplex stainless steels by nanoindentation and finite element method, *Mater. Sci. Eng. A.* 680 (2017) 359–367.
- [28] Y. Wang, Y.H. Yao, Z.P. Wang, Y.H. Jin, X.L. Zhang, J.N. Liu, Thermal ageing on the deformation and fracture mechanisms of a duplex stainless steel by quasi in-situ tensile test under OM and SEM, *Mater. Sci. Eng. A.* 666 (2016) 184–190.
- [29] D. Chandra, L.H. Schwartz, Mössbauer effect study of the 475 C decomposition of Fe-Cr, *Metall. Trans.* 2 (1971) 511–519.

- [30] M.B. Cortie, H. Pollak, Embrittlement and aging at 475 C in an experimental ferritic stainless steel containing 38 wt.% chromium, *Mater. Sci. Eng. A*. 199 (1995) 153–163.
- [31] B. Trindade, R. Vilar, Influence of nickel on 475° C embrittlement of Fe- Cr- Ni alloys: Mössbauer effect study, *Hyperfine Interact.* 66 (1991) 351–358.
- [32] H. Kuwano, Y. Ishikawa, T. Yoshimura, Y. Hamaguchi, Characterization of the spinodal decomposition of Fe- Cr alloys by Mössbauer spectroscopy, *Hyperfine Interact.* 69 (1992) 501–504.
- [33] H. Yamamoto, A study on the nature of aging of Fe-Cr alloys by means of the Mössbauer effect, *Jpn. J. Appl. Phys.* 3 (1964) 745.
- [34] J.W. Cahn, On spinodal decomposition, *Acta Metall.* 9 (1961) 795–801.
- [35] J. Zhou, An Atom-Probe Tomography Study of Phase Separation in Fe-Cr Based Steels, KTH Royal Institute of Technology, 2014.
- [36] M.K. Miller, R.E. Stoller, K.F. Russell, Effect of neutron-irradiation on the spinodal decomposition of Fe-32% Cr model alloy, *J. Nucl. Mater.* 230 (1996) 219–225.
- [37] R.A. Van Santen, The Ostwald step rule, *J. Phys. Chem.* 88 (1984) 5768–5769.
- [38] C.M. Wayman, Solid-state phase transformations, *Annu. Rev. Mater. Sci.* 1 (1971) 185–218.
- [39] A. Mateo, L. Llanes, M. Anglada, A. Redjaimia, G. Metauer, Characterization of the intermetallic G-phase in an AISI 329 duplex stainless steel, *J. Mater. Sci.* 32 (1997) 4533–4540.
- [40] H.J. Beattie, F.L. VerSnyder, A new complex phase in a high-temperature alloy, *Nature.* 178 (1956) 208–209.
- [41] J.M. Vitek, S.A. David, D.J. Alexander, J.R. Keiser, R.K. Nanstad, Low temperature aging behavior of type 308 stainless steel weld metal, *Acta Metall. Mater.* 39 (1991) 503–516.
- [42] Y. Matsukawa, T. Takeuchi, Y. Kakubo, T. Suzudo, H. Watanabe, H. Abe, T. Toyama, Y. Nagai, The two-step nucleation of G-phase in ferrite, *Acta Mater.* 116 (2016) 104–113.
- [43] T. Takeuchi, Y. Kakubo, Y. Matsukawa, Y. Nozawa, T. Toyama, Y. Nagai, Y. Nishiyama, J. Katsuyama, Y. Yamaguchi, K. Onizawa, Effects of neutron irradiation on microstructures and hardness of stainless steel weld-overlay cladding of nuclear reactor pressure vessels, *J. Nucl. Mater.* 449 (2014) 273–276.

- [44] C. Pareige, S. Novy, S. SAILLET, P. Pareige, Study of phase transformation and mechanical properties evolution of duplex stainless steels after long term thermal ageing (> 20years), *J. Nucl. Mater.* 411 (2011) 90–96.
- [45] P.J. Grobner, The 885 F (475 C) embrittlement of ferritic stainless steels, *Metall. Trans.* 4 (1973) 251–260.
- [46] A. Trautwein, W. Gysel, Influence of long-time aging of CF8 and CF8M cast steel at temperatures between 300 and 500 C on impact toughness and structural properties, in: *Stainl. Steel Cast.*, ASTM International, 1982.
- [47] A.A. Tavassoli, A. Bisson, P. Soulat, Ferrite decomposition in austenitic stainless steel weld metals, *Met. Sci.* 18 (1984) 345–350.
- [48] O.K. Chopra, Degradation of LWR core internal materials due to neutron irradiation, US Nuclear Regulatory Commission, Office of Nuclear Regulatory Research, 2010.
- [49] F.M. Haggag, W.R. Corwin, R.K. Nanstad, Effects of irradiation on the fracture properties of stainless steel weld overlay cladding, *Nucl. Eng. Des.* 124 (1990) 129–141.
- [50] F. Haggag, W. Corwin, D. Alexander, R. Nanstad, Tensile and Charpy Impact Behavior of an Irradiated Three-Wire Series-Arc Stainless Steel Cladding, in: *Eff. Radiat. Mater.* 14th Int. Symp. Vol. II, ASTM International, 1990.
- [51] J.S. Lee, I.S. Kim, R. Kasada, A. Kimura, Microstructural characteristics and embrittlement phenomena in neutron irradiated 309L stainless steel RPV clad, *J. Nucl. Mater.* 326 (2004) 38–46.
- [52] G.S. Was, *Fundamentals of radiation materials science: metals and alloys*, Springer, 2016.
- [53] S.J. Rothman, Effects of irradiation on diffusion in metals and alloys, in: *Phase Transform. Irradiat.*, 1983.
- [54] T. Takeuchi, J. Kameda, Y. Nagai, T. Toyama, Y. Matsukawa, Y. Nishiyama, K. Onizawa, Microstructural changes of a thermally aged stainless steel submerged arc weld overlay cladding of nuclear reactor pressure vessels, *J. Nucl. Mater.* 425 (2012) 60–64.
- [55] Y. Chen, B. Alexandreanu, K. Natesan, Crack Growth Rate and Fracture Toughness Tests on Irradiated Cast Stainless Steels, Argonne National Laboratory (ANL), 2013.
- [56] J.P. Massoud, P. Dubuisson, P. Scott, V.K. Chamardine, CIR II program: description of the Boris 6 and 7 experiments in the BOR-60 fast breeder reactor, EPRI Rep. 1011787 (2005).

- [57] G.W. Fynn, W.J.A. Powell, The cutting and polishing of electro-optic materials, (1979).
- [58] D.C. Zipperian, Metallographic specimen preparation basics, Pace Technol.
- [59] D.C. Zipperian, Metallographic handbook, Chief Tech. Off. PACE Technol. Tucson AR. (2011).
- [60] B. Katharine, Small, Guide to Etching Speciality Alloys, Adv. Mater. Process. (2008).
- [61] G.F. Vander Voort, E.P. Manilova, Imaging phases in steels, Adv. Mater. Process. 163 (2005) 32–37.
- [62] M.K. Miller, E.A. Kenik, Atom probe tomography: A technique for nanoscale characterization, Microsc. Microanal. 10 (2004) 336–341.
- [63] M.K. Miller, R.G. Forbes, Tutorial review: atom probe tomography, Mater Charact. 60 (2009) 461–469.
- [64] T. Hamaoka, A. Nomoto, K. Nishida, K. Dohi, N. Soneda, Effects of aging temperature on G-phase precipitation and ferrite-phase decomposition in duplex stainless steel, Philos. Mag. 92 (2012) 4354–4375.
- [65] W. Guo, D.A. Garfinkel, J.D. Tucker, D. Haley, G.A. Young, J.D. Poplawsky, An atom probe perspective on phase separation and precipitation in duplex stainless steels.
- [66] Y. Chen, P.H. Chou, E.A. Marquis, Quantitative atom probe tomography characterization of microstructures in a proton irradiated 304 stainless steel, J. Nucl. Mater. 451 (2014) 130–136.
- [67] K. Kumar, A. Pooleery, K. Madhusoodanan, R.N. Singh, J.K. Chakravartty, B.K. Dutta, R.K. Sinha, Use of miniature tensile specimen for measurement of mechanical properties, Procedia Eng. 86 (2014) 899–909.
- [68] W.R. Corwin, S.T. Rosinski, E. Walle, others, Small specimen test techniques, in: ASTM, 1998.
- [69] Y. Chen, C. Bunget, L. Mears, T.R. Kurfess, Investigations in subsurface damage when machining  $\gamma'$ -strengthened nickel-based superalloy, Proc. Inst. Mech. Eng. Part B J. Eng. Manuf. 230 (2016) 1221–1233.
- [70] A. Johnson, D. Fisher, G. Vander Voort, Precision Cutting-The Science of the Cut, Tech-Notes Using Microstruct. Anal. Solve Pract. Probl. 3 (2003).
- [71] A.-T. Akono, F.-J. Ulm, An improved technique for characterizing the fracture toughness via scratch test experiments, Wear. 313 (2014) 117–124.

- [72] A.T. Akono, P.M. Reis, F.J. Ulm, Scratching as a fracture process: From butter to steel, *Phys. Rev. Lett.* 106 (2011) 204302.
- [73] C.O. Ruud, A.A. Diaz, M.T. Anderson, Grain Structure Identification and Casting Parameters of Austenitic Stainless Steel (CASS) Piping, PNNL-19002 Richland Wash. Pac. Northwest Natl. Lab. (2009).
- [74] P. Ramuhalli, R.M. Meyer, A.D. Cinson, T.L. Moran, M. Prowant, B. Watson, M.T. Anderson, In-situ Characterization of Cast Stainless Steel Microstructures, in: *Proc. Eighth Int. Conf. NDE Relat. Struct. Integr. Nucl. Press. Components Berlin Ger.* 2012, 2012.
- [75] C.C. Silva, J.T. de Assis, S. Philippov, J.P. Farias, Residual Stress, Microstructure and Hardness of Thin-Walled Low-Carbon Steel Pipes Welded Manually, *Mater. Res.* 19 (2016) 1215–1225.
- [76] S. Kou, *Welding metallurgy*, John Wiley & Sons, 2003.
- [77] K. Li, D. Li, D. Liu, G. Pei, L. Sun, Microstructure evolution and mechanical properties of multiple-layer laser cladding coating of 308L stainless steel, *Appl. Surf. Sci.* 340 (2015) 143–150.
- [78] S.A. David, Ferrite morphology and variations in ferrite content in austenitic stainless steel welds, Oak Ridge National Lab., TN, 1981.
- [79] K.B. Alexander, M.K. Miller, D.J. Alexander, R.K. Nanstad, Microscopical evaluation of low temperature aging of type 308 stainless steel weldments, *Mater. Sci. Technol.* 6 (1990) 314–320.
- [80] L.J. Ayers, *The hardening of Type 316L stainless steel welds with thermal aging*, Massachusetts Institute of Technology, 2012.
- [81] K.L. Weng, H.R. Chen, J.R. Yang, The low-temperature aging embrittlement in a 2205 duplex stainless steel, *Mater. Sci. Eng. A.* 379 (2004) 119–132.
- [82] T. Tobita, M. Udagawa, Y. Chimi, Y. Nishiyama, K. Onizawa, Effect of neutron irradiation on the mechanical properties of weld overlay cladding for reactor pressure vessel, *J. Nucl. Mater.* 452 (2014) 61–68.
- [83] R.L. Plaut, C. Herrera, D.M. Escriba, P.R. Rios, A.F. Padilha, A short review on wrought austenitic stainless steels at high temperatures: processing, microstructure, properties and performance, *Mater. Res.* 10 (2007) 453–460.
- [84] M.R. Louthan Jr, *Optical metallography*, *ASM Handb.* 10 (1986) 299–308.
- [85] J.W. Fu, Y.S. Yang, J.J. Guo, Formation of a blocky ferrite in Fe–Cr–Ni alloy during directional solidification, *J. Cryst. Growth.* 311 (2009) 3661–3666.

- [86] S. Mburu, R.P. Kolli, D.E. Perea, S.C. Schwarm, A. Eaton, J. Liu, S. Patel, J. Bartrand, S. Ankem, Effect of aging temperature on phase decomposition and mechanical properties in cast duplex stainless steels, *Mater. Sci. Eng. A*. 690 (2017) 365–377.
- [87] S. Mburu, R.P. Kolli, D.E. Perea, S.C. Schwarm, A. Eaton, J. Liu, S. Patel, J. Bartrand, S. Ankem, Atom Probe Tomography Analysis of the Local Chemical Environment at the Austenite/Ferrite Inter-faces of Cast Duplex Stainless Steels, in: *Proc. 14th LACCEI Int. Multi-Conf. Eng. Educ.*
- [88] Y. Chen, W.Y. Chen, A.S. Rao, Z. Li, Y. Yang, B. Alexandreanu, K. Natesan, Fracture Resistance of Cast Austenitic Stainless Steels, in: *2016 24th Int. Conf. Nucl. Eng., American Society of Mechanical Engineers*, 2016.
- [89] W.J. Ai, H.C. Kuan, J.J. Dong, C.T. Kwok, K.H. Lo, Short-term spinodal decomposition—its effects on corrosion behaviour of a duplex stainless steel and feasibility as a strengthening treatment, *Mater. Corros.* 68 (2017) 395–404.
- [90] S. Lampman, *Weld integrity and performance*, ASM Int. (1997).
- [91] S.A. David, J.M. Vitek, D.J. Alexander, Embrittlement of austenitic stainless steel welds, *J. Nondestruct. Eval.* 15 (1996) 129–136.
- [92] P. Wilkes, Phase stability under irradiation—a review of theory and experiment, *J. Nucl. Mater.* 83 (1979) 166–175.
- [93] K. Fujii, K. Fukuya, Effects of radiation on spinodal decomposition of ferrite in duplex stainless steel, *J. Nucl. Mater.* 440 (2013) 612–616.
- [94] M. Li, M.K. Miller, W.-Y. Chen, Phase stability in thermally-aged CASS CF8 under heavy ion irradiation, *J. Nucl. Mater.* 462 (2015) 214–220.
- [95] B. Jönsson, Assessment of the mobilities of Cr, Fe and Ni in bcc Cr-Fe-Ni alloys, *ISIJ Int.* 35 (1995) 1415–1421.
- [96] Z. Li, W.-Y. Lo, Y. Chen, J. Pakarinen, Y. Wu, T. Allen, Y. Yang, Irradiation response of delta ferrite in as-cast and thermally aged cast stainless steel, *J. Nucl. Mater.* 466 (2015) 201–207.
- [97] R.O. Williams, H.W. Paxton, The nature of aging of binary iron-chromium alloys around 500 C, *J Iron Steel Inst.* 185 (1957) 358–374.
- [98] W. Xiong, P. Hedström, M. Selleby, J. Odqvist, M. Thuvander, Q. Chen, An improved thermodynamic modeling of the Fe–Cr system down to zero Kelvin coupled with key experiments, *Calphad.* 35 (2011) 355–366.
- [99] G. Gladyshev, *Radiation Processes in Crystal Solid Solutions*, Bentham Science Publishers, 2012.

- [100] K. Krishan, C. Abromeit, Calculation of radiation-induced instability in concentrated alloys, *J. Phys. F Met. Phys.* 14 (1984) 1103.
- [101] C. Abromeit, K. Krishan, Influence of irradiation on the spinodal decomposition of a concentrated alloy, *Acta Metall.* 34 (1986) 1515–1524.
- [102] S. Novy, Mécanisme de vieillissement à très longue échéance des aciers inoxydables austénoferritiques, Université de Rouen, 2009.
- [103] S. Novy, P. Pareige, C. Pareige, Atomic scale analysis and phase separation understanding in a thermally aged Fe–20at.% Cr alloy, *J. Nucl. Mater.* 384 (2009) 96–102.
- [104] J.K. Sahu, U. Krupp, R.N. Ghosh, H.-J. Christ, Effect of 475 C embrittlement on the mechanical properties of duplex stainless steel, *Mater. Sci. Eng. A.* 508 (2009) 1–14.
- [105] T.J. Nichol, A. Datta, G. Aggen, Embrittlement of ferritic stainless steels, *Metall. Mater. Trans. A.* 11 (1980) 573–585.
- [106] J.E. Westraadt, E.J. Olivier, J.H. Neethling, P. Hedström, J. Odqvist, X. Xu, A. Steuwer, A high-resolution analytical scanning transmission electron microscopy study of the early stages of spinodal decomposition in binary Fe–Cr, *Mater. Charact.* 109 (2015) 216–221.
- [107] F. Danoix, P. Auger, S. Chambrelaud, D. Blavette, A 3D study of G-phase precipitation in spinodally decomposed  $\alpha$ -ferrite by tomographic atom-probe analysis, *Microsc. Microanal. Microstruct.* 5 (1994) 121–132.
- [108] J.-Y. Jeon, Y.-J. Kim, J.-W. Kim, S.-Y. Lee, Effect of thermal ageing of CF8M on multi-axial ductility and application to fracture toughness prediction, *Fatigue Fract. Eng. Mater. Struct.* 38 (2015) 1466–1477.
- [109] D.J. Alexander, J.M. Vitek, S.A. David, Long-term aging of type 308 stainless steel welds: Effects on properties and microstructure, Oak Ridge National Lab., TN (United States), 1994.
- [110] W.J. Mills, Fracture toughness of stainless steel welds, in: *Fract. Mech. Ninet. Symp.*, ASTM International, 1988.
- [111] C.R. Weinberger, B.L. Boyce, C.C. Battaile, Slip planes in bcc transition metals, *Int. Mater. Rev.* 58 (2013) 296–314.
- [112] M.J. Marcinkowski, A. Szirmai, R. Fisher, Effect of 500degreesc aging on deformation behavior of iron-chromium alloy, *Trans. Metall. Soc. AIME.* 230 (1964) 676.

- [113] M.A. Meyers, O. Vöhringer, V.A. Lubarda, The onset of twinning in metals: a constitutive description, *Acta Mater.* 49 (2001) 4025–4039.
- [114] Y.-C. Hsieh, L. Zhang, T.-F. Chung, Y.-T. Tsai, J.-R. Yang, T. Ohmura, T. Suzuki, In-situ transmission electron microscopy investigation of the deformation behavior of spinodal nanostructured  $\delta$ -ferrite in a duplex stainless steel, *Scr. Mater.* 125 (2016) 44–48.
- [115] J.W. Cahn, HARDENING BY SPINODAL DECONPOSITION, in: *Symp. ROLE Substruct. Mech. Behav. Met.*, 1963: p. 375.
- [116] M. Kato, Hardening by spinodally modulated structure in bcc alloys, *Acta Metall.* 29 (1981) 79–87.
- [117] M.K. Miller, I.M. Anderson, J. Bentley, K.F. Russell, Phase separation in the Fe–Cr–Ni system, *Appl. Surf. Sci.* 94 (1996) 391–397.
- [118] Y.-Y. Chuang, Y.A. Chang, A thermodynamic analysis and calculation of the Fe–Ni–Cr phase diagram, *Metall. Trans. A.* 18 (1987) 733–745.
- [119] T. Yamada, S. Okano, H. Kuwano, Mechanical property and microstructural change by thermal aging of SCS14A cast duplex stainless steel, *J. Nucl. Mater.* 350 (2006) 47–55.
- [120] D.J. Maykuth, R.I. Jaffee, Influence of Chromium Metal Purity on the Properties of Chromium Alloys, *Ductile Chromium Its Alloys ASM.* (1957) 229–246.
- [121] R.O. Williams, Theory of precipitation hardening: Isotropically-strained system, *Acta Metall.* 5 (1957) 385–392.
- [122] T. Takeuchi, Y. Kakubo, Y. Matsukawa, Y. Nozawa, Y. Nagai, Y. Nishiyama, J. Katsuyama, K. Onizawa, M. Suzuki, Effect of neutron irradiation on the microstructure of the stainless steel electroslag weld overlay cladding of nuclear reactor pressure vessels, *J. Nucl. Mater.* 443 (2013) 266–273.
- [123] J.A. Brinkman, Production of atomic displacements by high-energy particles, *Am. J. Phys.* 24 (1956) 246–267.

## BIOGRAPHICAL SKETCH

Zhangbo Li was born in Guangshui, Hubei province, People's Republic of China. He received a B.S. degree in Materials Science and Engineering from Huazhong University of Science and Technology in 2012.

In August 2012, Zhangbo started a Master of Engineering program in Materials Science and Engineering at University of Florida. One year later, he joined Professor Yong Yang's research group and transferred to the Ph.D program at University of Florida. After completing his Ph.D, he plans to work in academia or industry.